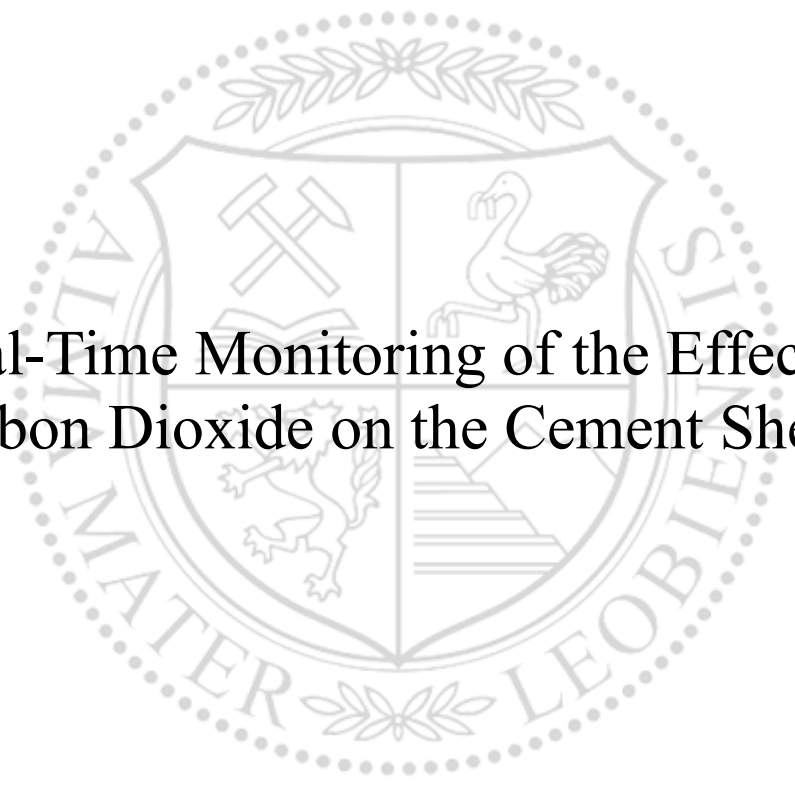




Chair of Drilling and Completion Engineering

Master's Thesis



Real-Time Monitoring of the Effect of
Carbon Dioxide on the Cement Sheath

Paul Wagner, BSc

July 2020

Scientia ac labore.

EIDESSTATTLICHE ERKLÄRUNG

Ich erkläre an Eides statt, dass ich diese Arbeit selbständig verfasst, andere als die angegebenen Quellen und Hilfsmittel nicht benutzt, und mich auch sonst keiner unerlaubten Hilfsmittel bedient habe.

Ich erkläre, dass ich die Richtlinien des Senats der Montanuniversität Leoben zu "Gute wissenschaftliche Praxis" gelesen, verstanden und befolgt habe.

Weiters erkläre ich, dass die elektronische und gedruckte Version der eingereichten wissenschaftlichen Abschlussarbeit formal und inhaltlich identisch sind.

Datum 01.07.2020



Unterschrift Verfasser/in
Paul, Wagner

Abstract

Global warming is one of the most significant issues the world is facing. Capturing carbon dioxide from the atmosphere or industrial processes and storing it in geological formations can help counteract climate change. Nevertheless, the interaction between well barrier elements such as cement, casing, tubulars, packers, and valves can lead to possible leakages. To accomplish successful carbon dioxide sequestration, injecting the carbon dioxide in its supercritical state is necessary. The supercritical carbon dioxide can corrode steel and elastomers and react with the calcium compounds in the cement, dissolving them and forming calcium carbonate and bicarbonate in the process. This carbonation can lead to channels forming on the cement-to-rock interface or cracking due to the carbonate precipitation, resulting in a loss of well integrity.

This study focusses on finding ways that enable the continuous monitoring of well integrity under in-situ conditions. The construction of an autoclave, capable of withstanding supercritical conditions of carbon dioxide, facilitates the in-situ monitoring. This autoclave also makes CT-scans of the pressurized sample possible, as well as acoustic measurements, using state-of-the-art piezo elements. The first tests will establish a baseline using neat Class G Portland cement to verify the design and sensors. The set up consists of a rock core in the middle of the autoclave cell surrounded by a cement sheath. Drilling a channel in the middle of the core expedites the distribution of the carbon dioxide. Once the ability of the sensors to monitor the integrity is verified, different cement compositions and their interaction with supercritical carbon dioxide can be studied.

The experimental setup and the procedure discussed here closely simulate the downhole condition. Hence, the results obtained using this setup and procedure is representative of what could be observed downhole. The direction is not to remove the sample from the cell and analyze it under in-situ conditions. Digitalization is powering the in-situ analysis in this experiment. After the carbonation, samples from the autoclave undergo a thorough chemical and physical analysis. The correlation of the data from the sensors and chemical analysis aids in further developing real-time monitoring.

The results from this study can lead to the prevention of leakage of carbon dioxide to the environment and other formations, which defeats the purpose of carbon dioxide sequestration. These results should improve the economics of these wells as well as the health, safety, and environmental aspects.

Zusammenfassung

Die globale Erwärmung ist eines der erheblichsten Probleme, die die moderne Gesellschaft lösen muss. Eine Möglichkeit, die globale Erwärmung zu stoppen oder zu reduzieren, ist die Abscheidung von Kohlendioxid aus der Atmosphäre oder industriellen Abgasen und dieses in geologischen Formationen zu lagern. Ein Problem dabei ist die Reaktion zwischen Kohlendioxid und Bohrlöchern, als Kombination von Zement, Rohren, Dichtungen und Ventilen, die zu möglichen Leckagen führen. Um eine Lagerung von Kohlendioxid zu ermöglichen muss es in seinem superkritischen Zustand injiziert werden. Superkritisches Kohlendioxid kann Stahl und Elastomere korrodieren und reagiert mit den Kalziumkomponenten in Zement. Diese werden zersetzt und es kommt zur Bildung von Karbonaten und Bikarbonaten. Diese Karbonatisierung führt zu einem Verlust der Integrität eines Bohrloches.

Diese Arbeit fokussiert sich auf die Entwicklung von Methoden, die die kontinuierliche Überwachung der Bohrlochintegrität unter realen Bedingungen ermöglichen. Diese Überwachung wird durch die Konstruktion einer Autoklave ermöglicht, deren Auslegung die superkritischen Bedingungen des Kohlendioxids berücksichtigt. Diese Autoklave ermöglicht auch CT Scans unter praxisnahen Bedingungen (Druck, Temperatur). Auch akustische Messungen mit Piezoelementen sind möglich. Erste Tests mit reinem Klasse G Portland Zement erstellen eine Referenz. Die Anordnung in der Autoklave besteht aus einem Gesteinskern, der mit Zement ummantelt ist. Eine Bohrung in der Mitte des Gesteinskerns ermöglicht eine schnelle und gleichmäßige Verteilung des Kohlendioxids. Bei einer Eignung der Sensoren zur Überwachung der Bohrlochintegrität können verschiedene Zemente und ihre Eignung zur Verwendung mit Kohlendioxid getestet werden.

Der Versuchsaufbau und -ablauf, die hier besprochen werden, gleicht den Zuständen in einer geologischen Formation, wodurch die Erkenntnisse repräsentativ sind für die realen Zustände. Während des ganzen Versuchs wird der Druck nie von den Proben genommen. Digitalisierung ermöglicht die in-situ Analyse. Nach Beendigung des Versuchs werden Proben des Zements eingehend chemisch und physikalisch untersucht. Die Daten dieser Analysen werden mit den Sensordaten verglichen, um die kontinuierliche Überwachung zu verbessern.

Die Ergebnisse dieser Arbeit können die Leckage von Kohlendioxid in die Umwelt oder andere Formationen verhindern. Eine solche Leckage führt zu einem Misslingen der Lagerung von Kohlendioxid. Die Ergebnisse sollten zu einer ökonomischen Verbesserung der Bohrungen sowie von Gesundheits-, Sicherheits- und Umweltaspekten führen.

Acknowledgements

I wish to show my gratitude to first, and foremost, Univ.-Prof. MBA, PhD Kris Ravi, and Ass.Prof. Dipl.-Ing. Dr.rer.nat. Michael Prohaska-Marchried. Thank you for your continuous support in realizing this project.

I would also like to pay special regards to the Chair of Reservoir Engineering, especially Univ.-Prof. Dipl.-Phys. Dr.rer.nat. Holger Ott, Dipl.-Ing. Pit Arnold and Ing. Michael Koopmans for helping me with the CT-scans in this thesis and supporting me in their evaluation.

I would like to thank my colleagues Karez Abdulhameed, Arash Nasiri, and Nikolaus Zimmermann, for always helping me in the laboratory when needed.

I would like to thank my parents for being with me through all of my studies and my life and supporting me throughout.

Finally, I wish to show my deepest gratitude to my loving wife, Dipl.-Ing. Bettina Strommer. She gave me strength in the direst moments of this project and always held my head up high and motivated me to push through.

Contents

Chapter 1 Introduction.....	1
Chapter 2 Geological Carbon Dioxide Deposition.....	3
2.1 Prerequisites for Both Approaches.....	3
2.1.1 Capturing Carbon Dioxide.....	3
2.1.2 Transporting Carbon Dioxide.....	5
2.2 Carbon Capture and Storage (CCS).....	5
2.2.1 The Potential of CCS.....	5
2.2.2 Injecting the Carbon Dioxide for CCS.....	6
2.2.3 Economics of CCS.....	7
2.3 Utilizing Carbon Dioxide in Enhanced Oil & Gas Recovery (EOR).....	8
2.3.1 Injecting Carbon Dioxide for EOR.....	9
2.3.2 Economics of Carbon Dioxide in EOR.....	9
Chapter 3 Carbonation of Cement.....	10
3.1 Portland Cement Composition.....	10
3.2 Portland Cement Hydration.....	11
3.2.1 Clinker Phase Hydration.....	11
3.2.2 Aluminate Phase Hydration.....	13
3.3 Portland Cement Carbonation.....	14
Chapter 4 Ultrasonic Detection of Cement Carbonation.....	16
4.1 Physical Principles of Ultrasonic Analysis.....	16
4.1.1 Piezoelectric Generation of Ultrasonic Waves.....	16
4.1.2 Ultrasonic Wave Propagation and Attenuation.....	18
4.2 The Set-up.....	20
4.3 Compressive Strength Baseline Testing.....	21
Chapter 5 Experiments.....	24
5.1 Previous Research on Oil Well Cement Carbonation.....	24
5.1.1 Jobard et al. – Effect of Water and Supercritical CO ₂ on Caprock/Cement Interface.....	24
5.1.2 Aiex et al. – Effect of Static CO ₂ on Cement under High-Pressure & High-Temperature Conditions.....	24
5.1.3 Lacerda et al. – Monitoring the Carbonation Front Progress.....	25
5.2 Construction of an Autoclave facilitating Real-time Carbonation Monitoring....	25
5.2.1 Designing the Autoclave.....	25
5.2.2 The construction of the Autoclave.....	27
5.2.3 Testing the Autoclave.....	27
5.3 Future Designs.....	28

5.4 Experiment Procedure.....	28
5.5 Risk Assessment of the Testing Procedure.....	34
5.5.1 Determining the Legal Basis of the Autoclave	34
5.5.2 Risk Identification and Evaluation.....	35
5.5.3 Risk Mitigation.....	36
5.6 Experiment I – Heavy Carbonation Baseline	37
5.6.1 The Slurry Composition and Analysis.....	37
5.6.2 Preparing and Pressurizing the Autoclave	38
5.6.3 Monitoring the Carbonation	41
5.6.4 Termination of the Experiment.....	48
5.6.5 Experiment I – Conclusion	49
5.7 Experiment II – Light Carbonation Baseline	51
5.7.1 The Slurry Composition and Analysis.....	51
5.7.2 Preparing and Pressurizing the Autoclave	52
5.7.3 Monitoring the Carbonation	54
5.7.4 Termination of the Experiment.....	60
5.7.5 Experiment II – Conclusion.....	61
5.8 Chemical and Mechanical Analysis.....	62
5.8.1 Mechanical Analysis.....	62
5.8.2 Chemical Analysis	62
Chapter 6 Comparison of the Experiments	64
6.1 Comparison of the Pressure and Temperature Data	64
6.2 Comparison of the CT-Scans	65
Chapter 7 Conclusion.....	68

Chapter 1 Introduction

The climate of the earth is a vastly complex system incorporating multiple components of the entire planet. This system is confusing to understand since a plethora of parameters influence it. Scientists have learned to understand this system, and the leading conclusion is that humans are causing a global warming effect, influencing the global climate terribly. The leading cause of this anthropogenic climate change is the generation of greenhouse gases. Greenhouse gases comprise carbon dioxide (CO₂), methane (CH₄), nitrous oxide (N₂O), ozone (O₃), and water vapor (H₂O). Carbon dioxide is, by the percentage, the most significant part of this mixture. The industry emits these gasses at the surface of the earth from where they will rise into the troposphere in 10- to 15-kilometer altitude. In these altitudes, the gasses form an insulating blanket, trapping radiation leaving the planet's system. This way, more radiation from the sun goes into the atmosphere than leaves it, ultimately heating the planet (Mathez and Smerdon 2018).

Since carbon dioxide is the most influential driver of global warming, it accounts for more than 50% of the total amount of greenhouse gasses, handling its emission will have the most positive impact on the hindrance of global warming. **Figure 1** shows the growth of greenhouse gas emissions over the last forty years and what role carbon dioxide plays in this. Lowering carbon dioxide emissions could cut total emissions by a significant portion (JRC / PBL).

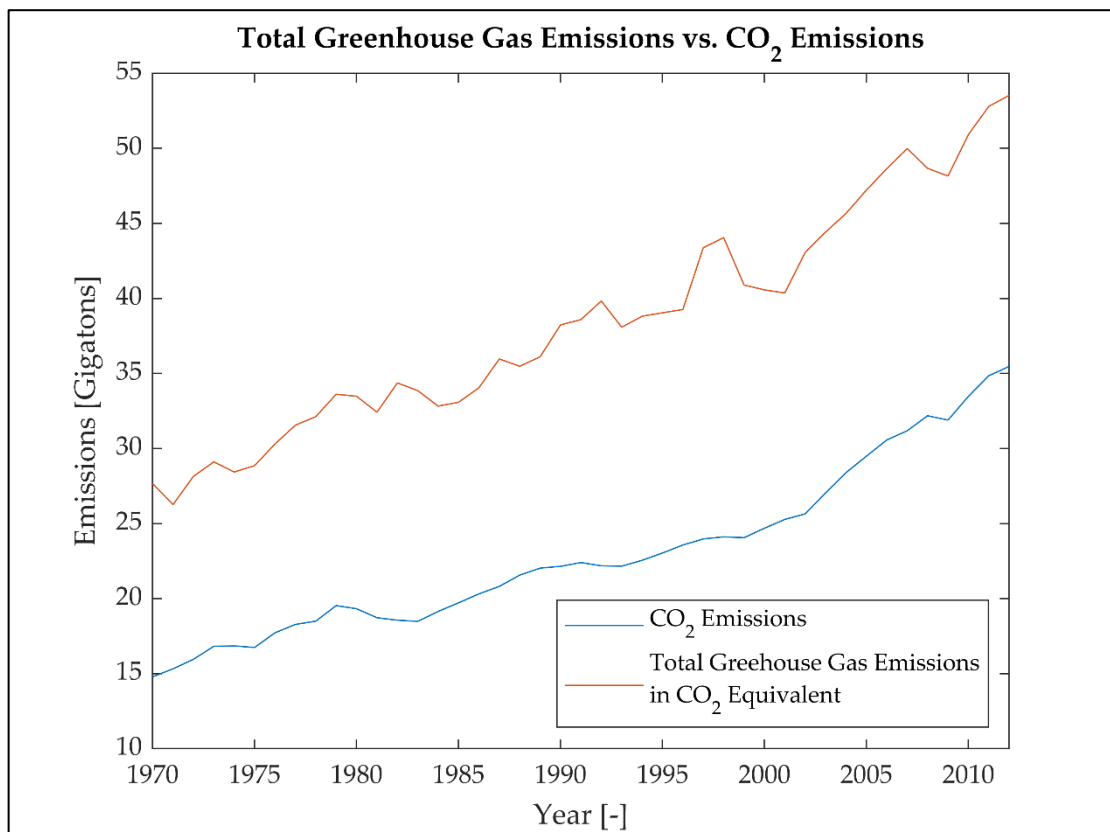


Figure 1: Comparing the amount of CO₂ emission to the total amount of greenhouse gas emission (JRC / PBL).

Introduction

One promising method to tackle the rising carbon dioxide emissions are the processes of carbon capture and storage and the utilization of carbon dioxide as an enhanced oil recovery method. For these processes, capture systems trap carbon dioxide, either from industrial plants or from the atmosphere. At the moment, capturing carbon dioxide typically takes place close to the storage reservoir, to avoid transport. Pipelines deliver the carbon dioxide to the well site. Potential reservoirs for carbon dioxide storage include depleted oil and gas fields as well as saline formations. For enhanced oil recovery, the candidate selection is different. A requirement is the presence of an intact caprock, forming a trap and keeping the carbon dioxide in the reservoir. Depending on geological factors, carbon dioxide becomes supercritical at depths of 800 to 1000 meters. In this supercritical state, carbon dioxide uses the entire potential space of underground storages (Bert Metz 2005).

The main issue in using oil and gas wells for the storage of carbon dioxide is the cement used in constructing the wells. When exposing cement to carbon dioxide, Calcium bearing phases of the cement react with carbon dioxide forming carbonate and the more harmful bicarbonate. Typically, these reactions require a certain amount of water, e.g., in the form of humidity. The gaseous carbon dioxide then dissolves in the water and penetrates pores of the cement, where reactions will begin. In the underground storage of carbon dioxide, as mentioned before, the state is supercritical, and the carbon dioxide penetrates cement pores far quicker. The carbonation of oil and gas well cement can lead to disastrous consequences.

The cement in oil and gas wells is an essential part of guaranteeing the integrity of a well. After running the casing of an oil and gas well, pumping cement into the annular area between casing and formation ensures that the casing is fixed in place, and more importantly, that there are no fluid migrations paths behind the casing. If fluid can migrate behind the casing, the well's integrity is compromised, and interventions are in order.

To better understand the speed of carbonation and how it affects the cement's physical and chemical properties, this thesis outlines a method to analyze the carbonation in real-time and under near-reservoir conditions. Designing and constructing an autoclave, capable of carrying out such tests, is the purpose of this thesis. Creating a standardized procedure of cement testing using the autoclave ensures the high reproducibility of the analysis. Also, a stochastic model gives more profound insides of how and where the carbonation is most likely to take place.

Chapter 2 Geological Carbon Dioxide Deposition

When speaking of the geological deposition of carbon dioxide, there are two entirely different approaches. There is, on the one hand, the permanent storage of carbon dioxide in depleted oil and gas reservoirs, unminable coal beds, and deep salt formations and, on the other hand, the utilization of carbon dioxide as an enhanced oil/gas recovery method in active oil and gas fields. Economically, these approaches offer wholly different opportunities. This chapter will focus on both these approaches and outline their potentials and shortcomings. **Figure 2** shows a map of the world with indicators in locations of large scale carbon dioxide projects, either underway or proposed.

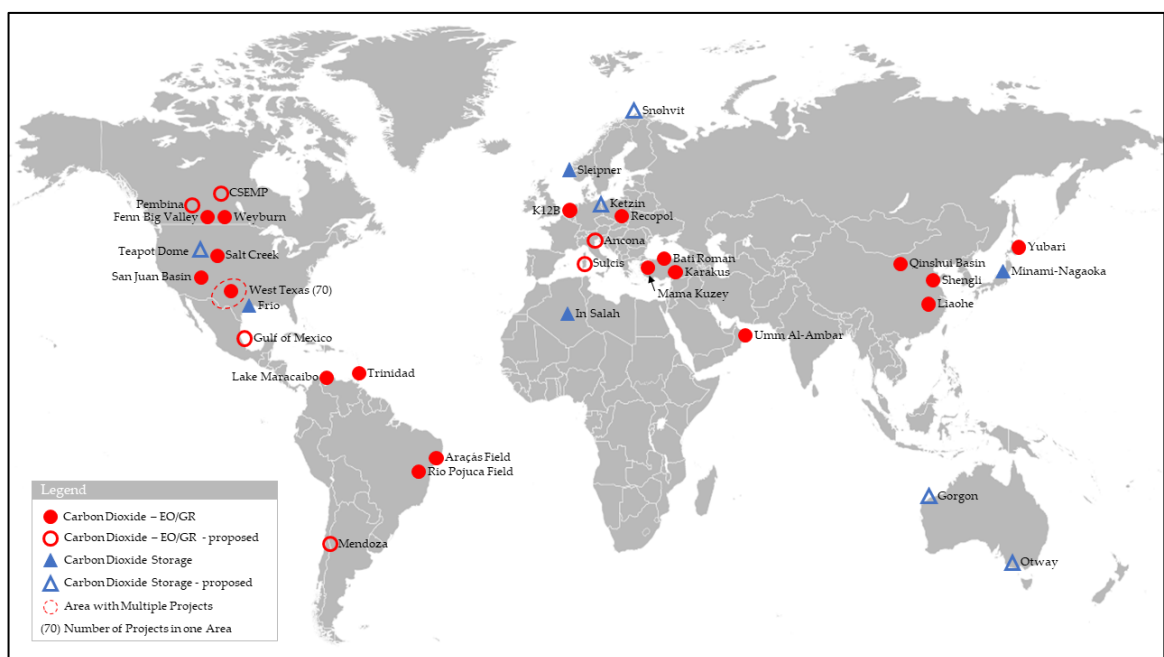


Figure 2: Worldwide locations of carbon dioxide storage activities (Bert Metz 2005).

2.1 Prerequisites for Both Approaches

To store carbon dioxide in a geological formation or utilize it in enhanced oil or gas recovery, capturing and transporting the carbon dioxide to the desired location needs to happen beforehand. The capture system

2.1.1 Capturing Carbon Dioxide

Typically, the capturing of carbon dioxide takes place at sizeable industrial plants, so-called point sources. Although capturing carbon dioxide out of the atmosphere is possible, it is not yet a viable option. Thus, this part will only discuss the capturing at point sources. When using fossil fuel or biomass, there are three essential systems to capture carbon dioxide: post-combustion, oxy-fuel combustion, and pre-combustion

capture. **Figure 3** illustrates the fundamental processes of these three systems. In some cases, carbon dioxide capturing carbon dioxide happens directly from the process streams, e.g., during natural gas purification, where carbon dioxide is a waste product. Other examples are the production of synthesis gas, cement, or steel (Bert Metz 2005).

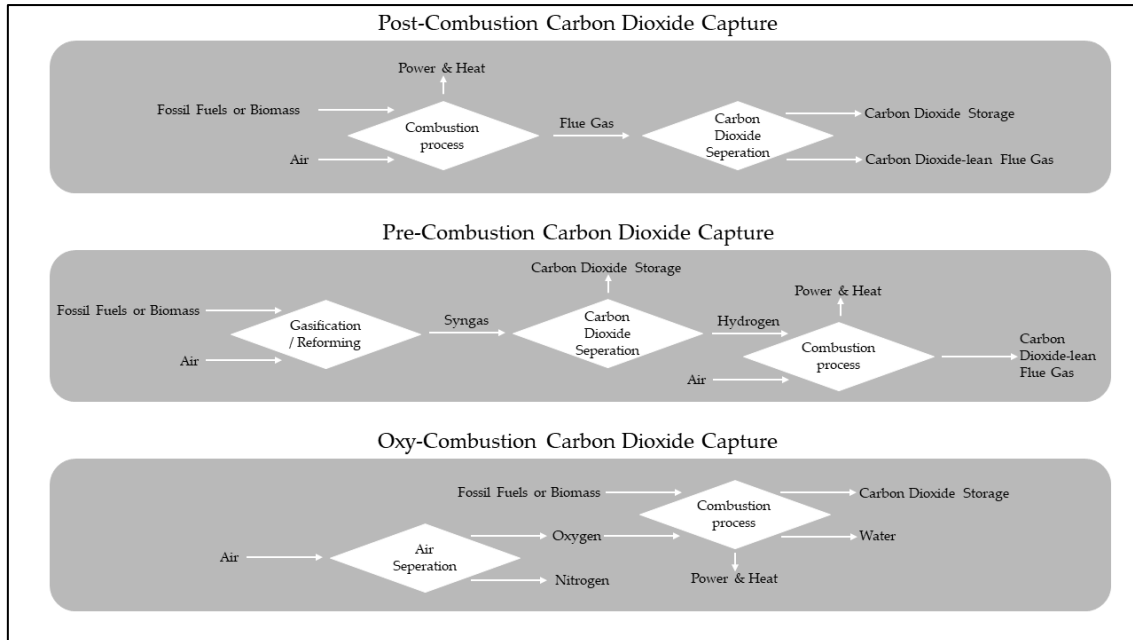


Figure 3: Three basic systems of carbon dioxide capture (IEA 2016).

The post-combustion system starts the process after conventional combustion that creates flue gas. This system focusses on the separation of the flue gas to isolate the carbon dioxide. In a pre-combustion system, the focus lies on gasifying the fuels beforehand through oxygen-deprived combustion. The syngas created in this combustion represents the basis for carbon dioxide separation. In the final system, oxy-combustion, firstly, the air is separated to enable a combustion process with pure oxygen. This combustion creates more energy in the form of heat and creates only carbon dioxide and water as waste products. The created waste products also function as a regulating agent for combustion to achieve the desired energy levels (Goel et al. 2018).

In order for any of these systems to achieve their purpose, a capturing mechanism needs to be in place. There are three essential mechanisms, usage of a sorbent/solvent, usage of a membrane, or cryogenic distillation. In the case of usage of a sorbent/solvent, the carbon dioxide passes through a solid or liquid absorbent capable of fixing it. The mixture then passes to another vessel, where the recovery of the absorbent and the separation of the carbon dioxide takes place. This process typically requires energy. This reaction consumes some absorbent, and the remaining portion flows back into the capturing vessel. This system does not require high pressures and works best with an increased flow time of the carbon dioxide through the absorbent. The mechanism of using a membrane requires higher pressures since a selectively permeable membrane traps the carbon dioxide molecules, and the remaining gas passes. There are different types of available membranes, depending on the gas composition. Even though membrane separation is in use in large scale industrial applications, there is no application in large scale CCS applications. The same applies to cryogenic distillation, a

system tried and tested in air separation. In this distillation, gas is liquified in a series of compression, cooling, and expansion steps. As with the membrane capture, cryogenic distillation also requires a massive flow of oxygen, which lowers the applicability in CCS. The most common method of capturing carbon dioxide for CCS is the usage of an absorbent. The usage of absorbent creates economic implications, explained in a later chapter (Bert Metz 2005; IEA 2016).

2.1.2 Transporting Carbon Dioxide

The most practical method of transport for carbon dioxide is by pipeline. When transporting carbon dioxide via pipeline, the phase of the carbon dioxide is essential. Since gas has a low density, the transport is inefficient. The most common state is a dense phase liquid. For this state, a pressure of min. 73.8 bar and a temperature of min. -56.6°C is necessary. When the pressure of carbon dioxide is above the critical pressure but the temperature below the critical temperature, the density increases with the decreasing temperature. This characteristic is why carbon dioxide pipeline transport happens in the dense phase liquid state. In this state, the density is similar to a liquid, whereas the viscosity and compressibility resemble a gas. This phase also applies to other modes of transport, e.g., in a container on a ship, truck, or train. Since a high density requires low temperatures, cryogenic transport is required, and the cryogenic conditions create a considerable energy demand. Another issue is the pipeline network since carbon dioxide transport requires a dedicated pipeline network. One such network exists in the United States, where carbon dioxide is in use as an enhanced oil/gas recovery method since the 1980s (Seevam et al. 2007).

2.2 Carbon Capture and Storage (CCS)

The process of carbon capture and storage offers serious potential in lowering carbon dioxide emissions in fossil-based industries and, ultimately, stop anthropogenic climate change. Even though the potential is there, there are controversies regarding CCS in different categories, the most important being economic feasibility and environmental considerations. This chapter focusses on the technology of capturing carbon dioxide and its geological sequestration, besides shedding light on the controversies surrounding CCS.

2.2.1 The Potential of CCS

Three distinct geological formations meet the essential prerequisites for carbon dioxide storage: depleted oil and gas reservoirs, unminable coal beds, and deep salt formations. In order for any of these to function as a carbon dioxide disposal site, a sealing cap rock needs to be in place. Unminable coal beds and deep salt formations require a minimal permeability to function as carbon dioxide disposal sites. Typically, depleted oil and gas reservoirs have sufficient permeability (Bert Metz 2005).

One significant advantage is that the technology required to inject carbon dioxide into deep geological formations is often the same as in oil and gas exploration. From the necessary well with their monitoring methods to computer-aided reservoir simulations, all of it is necessary for oil and gas exploration as well as carbon dioxide storage.

Reservoir Type	Lower Estimate [Gigatons]	Upper Estimate [Gigatons]
Oil and Gas Fields	675	900
Unminable Coal Beds	3	200
Deep Saline Formations	1,000	Up to 10,000

Table 1: Potential storage capacity of the eligible formations (Bert Metz 2005).

Table 1 shows the upper and lower estimates of potential storage space for carbon dioxide in the above mentioned geological formations. With emissions of roughly 36 gigatons of carbon dioxide in 2012, it is possible to store this fraction of the total amount of greenhouse gases. Unfortunately, the human race is far away from being able to dispose of the entire amount of generated carbon dioxide. One estimation by the International Energy Agency (IEA) expects CCS to account for a yearly emission reduction of 8.2 gigatons in 2050. With extrapolated data to 2050, this corresponds to roughly 19% of the total carbon dioxide emissions. In other words, CCS has the potential to lower global carbon dioxide emissions by one-fifth of the total emissions (IEA 2016).

2.2.2 Injecting the Carbon Dioxide for CCS

The fundamental prerequisite for a geological formation to function as a carbon dioxide storage is the existence of a low permeable seal above the formation. Such a low permeable seal is typical in oil and gas reservoirs since the seals trap the hydrocarbons and create accumulations. The seal is necessary since carbon dioxide is buoyant in almost all subsurface settings and will migrate to the uppermost point of the formation. The rate of injection largely depends on the porosity and permeability of the formation. For economic CCS operations, an injection rate of at least one-megatonne carbon dioxide per year is necessary. Proper CCS operations inject multiple thousand tonnes of carbon dioxide per day (Bert Metz 2005).

It requires a well to inject carbon dioxide into a geological formation, often thousands of meters below the surface. Injection wells are common in the oil and gas industry and enable enhanced oil recovery for many years. Instead of injecting formation water back into the formation or natural gas, a means of enhanced oil recovery, injecting carbon dioxide requires corrosion-resistant completions. State-of-the-art technologies facilitate much more sophisticated well trajectories for injection wells, realizing horizontal and extended reach wells. A horizontal or extended reach injection well can achieve the same results as multiple conventional injection wells (Bert Metz 2005).

The governing factor of the injection rate and displacement efficiency is the phase of carbon dioxide. In its supercritical state, carbon dioxide has a fraction of the viscosity of oil and water. At the triple point, supercritical carbon dioxide has a density of 468.19 kg/m³, whereas gaseous carbon dioxide has a density of 1.8075 kg/m³ at atmospheric pressure and 25 °C. The liquid density at the triple point is 1178.4 kg/m³. It becomes evident that the high-density liquid phase is the most practical for transport, but injection and displacement require different properties. Supercritical carbon dioxide is miscible in natural gas and forms a stable front expanding inside the reservoir. The

supercritical carbon dioxide is not miscible in formation water. If there is no miscibility, the displacement depends on the density difference of the formation fluids and the carbon dioxide. When injecting supercritical carbon dioxide into an oil reservoir, the displacement and miscibility are contingent on the composition of the oil, since carbon dioxide is miscible in specific compositions. The behavior of the fluid system is entirely different if the carbon dioxide is miscible. The buoyant forces are considerably lower if the fluids are miscible, and this will result in less vertical flow and more significant radial displacement. A buoyant plume will form nonetheless. When carbon dioxide migrates through a formation, a portion of the carbon dioxide will dissolve into formation water. The dissolved carbon dioxide is subject to water flow as a means of displacement. This water flow has minimal velocities, ranging from millimeters to centimeters per year. Since water with dissolved carbon dioxide is slightly more dense than the formation water, it will migrate downwards, resulting in formation water migrating towards the carbon dioxide plume and causing more carbon dioxide to dissolve. Simulations have shown that this mechanism replaces gas displacement after a few hundred years, and the liquid migration of formation water with dissolved carbon dioxide becomes the dominating displacement mechanism (Air Liquide; Bert Metz 2005).

2.2.3 Economics of CCS

The determining factors of CCS for most corporations are economics. As opposed to enhanced oil recovery, CCS does not create additional value at the moment. As legislations change, this might change as well. One accepted theory is that governments are introducing fines or taxes on emitted carbon dioxide. These taxes or fines can be off-put by storing the CCS and keeping it from discharging into the atmosphere.

This section will only focus on the storing costs of carbon dioxide in geological formations and neglect costs resulting from capture, compression, and transport. The assumption is the delivery of dense-liquid carbon dioxide to the well site or a surface station with a pipeline network in the case of multiple wells. The three main drivers of storage costs are well construction, infrastructure, and the necessary project administration and management. Constructing a well for the sole purpose of CCS enables additional considerations in the planning phase in terms of carbon dioxide resistance. The storage cost is going to be far higher as compared to the usage of an existing oil and gas well. In terms of safety, utilizing existing oil and gas wells is more complicated, since conventional Portland cement is not carbon dioxide resistant.

Option Type	On- or Offshore	Location	US\$/t Carbon Dioxide stored		
			Low	Mid	High
Saline Formation	Onshore	Australia	0.2	0.5	5.1
Saline Formation	Onshore	Europe	1.9	2.8	6.2
Saline Formation	Onshore	USA	0.4	0.5	4.5

Option Type	On- or Offshore	Location	US\$/t Carbon Dioxide stored		
			Low	Mid	High
Saline Formation	Offshore	Australia	0.5	3.4	30.2
Saline Formation	Offshore	North Sea	4.7	7.7	12.0
Depleted Oil Field	Onshore	USA	0.5	1.3	4.0
Depleted Gas Field	Onshore	USA	0.5	2.4	12.2
Disused Oil or Gas Field	Onshore	Europe	1.2	1.7	3.8
Disused Oil or Gas Field	Offshore	North Sea	3.8	6.0	8.1

Table 2: Reported carbon dioxide storage costs from different studies and reports (Allinson et al. 2003; Bock et al. 2003; Chris Hendricks, Wina Crijns-Graus, Frank Bergen 2004).

The most influential part of the storage cost is the well construction; prices for an injection well range from 200.000 US\$ for cheap onshore wells to 25 million US\$ for offshore wells. Re-completing existing wells can be a far cheaper option. Of course, depth is also an influence, since well construction costs and compression costs increase with depth. Permitting a certain impurity of carbon dioxide can lower costs. Higher impurities lower costs while capturing the carbon dioxide, but these impurities (NO_x , H_2S , SO_x) increase completion costs due to their corrosive properties. Finding a middle ground in these considerations decides over the feasibility of a CCS project (Bock et al. 2003; Chris Hendricks, Wina Crijns-Graus, Frank Bergen 2004).

2.3 Utilizing Carbon Dioxide in Enhanced Oil & Gas Recovery (EOR)

An oilfield undergoes various phases of production in its life cycle, and after the primary and secondary phases of production, there is still roughly 65% of the oil in place. So-called tertiary recovery methods enable the production of the oil that is still in the reservoir. Utilizing carbon dioxide as an enhanced oil recovery method is such a tertiary method and in use since the 1970s. The injected fluid has to be miscible with oil, changing the wettability properties, to achieve increased tertiary production. Supercritical carbon dioxide is entirely miscible in most oils. This type of tertiary production accounts for roughly 17% of the total production of a well. It is important to note that the storage of carbon dioxide in a geological formation is a beneficial side effect of EOR. Keeping that in mind, EOR injections and production wells may not enable the storage of carbon dioxide over a long duration. The utilization of carbon dioxide in EOR processes only

takes place as long as the enhanced production still economically outweighs the capture, transport, and injection of carbon dioxide (Institute for 21st Century Energy 2012).

2.3.1 Injecting Carbon Dioxide for EOR

The key to successful EOR using carbon dioxide is the miscibility of carbon dioxide with oil. The light components of the oil are entirely miscible, whereas heavy components are not. This lack of miscibility is a limitation since carbon dioxide cannot dissolve in heavy oil. Assuming a well is a candidate for EOR using carbon dioxide, two commonly used injection strategies exist. A requirement to choose the correct injections strategy is a thorough understanding of the reservoir pressure. If the reservoir pressure is at the desired level, a continuous carbon dioxide injection delivers the best results. In this strategy, zones form within the reservoir. Near the injecting well, a carbon dioxide zone will form followed by a miscible zone where carbon dioxide and oil form a single fluid, followed by a so-called oil slug, a zone of pure oil moving towards the producing well. Between these zones are of course transition zones ranging from either pure oil or carbon dioxide to the thoroughly mixed fluid. In terms of carbon dioxide storage efficiency, this is the better strategy, since a continuous flow into the reservoir takes place. The other strategy alternates between the injection of water and carbon dioxide, usually referred to as water alternating gas (WAG). During WAG, the injection consists of fixed cycles of a known volume of water and carbon dioxide. The cycle length ranges from a month up to a year, and the ratio of the volumes of water and dense liquid carbon dioxide is between 1:1 and 2:1. The injection of water reduces the mobility of the carbon dioxide in the formation preventing channeling. Although in terms of EOR, WAG is the better strategy, the storage efficiency of carbon dioxide is far lower. Besides the fact that there is no injection of carbon dioxide happening in the water cycles. This fact underlines that carbon dioxide in EOR applications only has the beneficial side effect of storing carbon dioxide, but the essence is an increased production of oil (Saini 2017).

2.3.2 Economics of Carbon Dioxide in EOR

The custom in utilizing carbon dioxide for EOR operations is for the operating companies to buy carbon dioxide in large amounts. There are projects where significant point sources supply carbon dioxide. However, the everyday commercial basis is procuring carbon dioxide from manufacturers. The economics of the operation depends on the oil price and the carbon dioxide price. The carbon dioxide price ties to the oil price. In the United States, a WTI price of 25 US\$ per barrel represents a carbon dioxide price of 16.3 US\$ per tonne. The revenues from the oil production need to compensate for the increased expenditure due to carbon dioxide purchasing. This expenditure is quite significant in EOR projects since, on average, it accounts for 68% of the totals costs. Calculations have shown that each additionally recovered barrel of oil requires between 0.15 to 0.4 tonnes of carbon dioxide. Since EOR is not an optimized storage operation, a fraction of the carbon dioxide comes back to the surface together with the produced oil. Surface separators split the oil from the carbon dioxide, followed by the reinjection of the carbon dioxide (Bock et al. 2003; Bert Metz 2005).

Chapter 3 Carbonation of Cement

As explained in the chapter before, when storing carbon dioxide in a geological formation or utilizing it in EOR, the carbon dioxide is typically injected in its supercritical state. With carbon dioxide having a triple point of 31.1 °C and 73.8 bar, almost all potential storage reservoirs exceed these values causing the presence of carbon dioxide in its supercritical state. The most crucial issue with this is that the calcium bearing phases within Portland cement react with carbon dioxide causing carbonation. This carbonation, more precisely, an exact real-time measurement of it under in-situ conditions, is the main topic of this thesis. It is of utmost significance to monitor and understand the carbonation and its progression since it can have detrimental effects on the cement and, ultimately, the well's integrity.

3.1 Portland Cement Composition

The most common cement used in oil and gas cementing operations is Portland cement. Portland cement is also the most prevalent example of hydraulic cement. Hydraulic cement is the cement which develops compressive strength due to hydration. This hydration involves reactions between water and cement components. A thorough explanation of such hydration follows in a later section.

Portland cement is categorized into different classes and grades by the American Petroleum Institute (API). These classes and grades give regulations on the chemical composition of the cement. One of the most popular classes, and also used for the baseline experiments in this thesis, is API Class G cement. The API defines class G cement as follows:

"The product obtained by grinding Portland cement clinker, consisting essentially of hydraulic calcium silicates, usually containing one or more forms of calcium sulfate as an interground additive. No additives other than calcium sulfate or water, or both, shall be interground or blended with the clinker during manufacture of Class G well cement.

This product is intended for use as a basic well cement. Available in moderate sulfate-resistant (MSR) and high sulfate-resistant (HSR) Grades." (ANSI/API 10A/ISO 10426-1-2001 2002)

As mentioned above, the baseline experiments in this thesis utilize API Class G cement. More precisely, Class G High-Sulfate Resistant Black Label cement from Dyckerhoff. The definition of the standardized chemical composition of this cement appears in **Table 3**.

High-Sulfate Resistant API Class G Cement	
Magnesium Oxide (MgO), maximum, %	6.0
Sulfur Trioxide (SO ₃), maximum, %	3.0
Loss on Ignition, maximum, %	3.0
Insoluble Residue, maximum, %	0.75

High-Sulfate Resistant API Class G Cement	
Tricalcium Silicate (C ₃ S), maximum, %	65
Tricalcium Silicate (C ₃ S), minimum, %	48
Tricalcium Aluminate (C ₃ A), maximum, %	3
Tetracalcium Aluminoferrite (C ₄ AF) plus twice the Tricalcium Aluminate (C ₃ A), maximum, %	24
Total Alkali Content expressed as Sodium Oxide (Na ₂ O) equivalent, maximum, %	0.75

Table 3: Chemical requirements for API Class G high-sulfate resistant cement (ANSI/API 10A/ISO 10426-1-2001 2002).

Not only are the chemical properties of API cement strictly standardized, but also their physical properties. Keeping the amount of mix water used and the curing conditions and time at the values as mentioned in the standard ensures meeting the required physical properties. The API standard then indicates a minimum compressive strength to be expected.

3.2 Portland Cement Hydration

The following section focus on the chemical reactions behind the hydration of the aluminate and clinker phases present in Portland cement. Understanding these phases and their corresponding hydration mechanisms is detrimental in understanding and monitoring the carbonation of these phases.

3.2.1 Clinker Phase Hydration

Controversies surrounded the hydration process of the cement clinker phases since the early 20th century, and even nowadays, not all facets of this hydration are fully understood. The most important mechanism is the hydration of C₃S since it makes up a significant portion of the cement and influences the hydration and hardening the most. Another influential part is C₂S, but since it behaves similarly to C₃S, this section will consider only the hydration of C₃S. Calorimetry readings lead to a split of the clinker hydration into five distinctive periods; **Figure 4** depicts these five distinct periods (Nelson and Guilloit 2006).

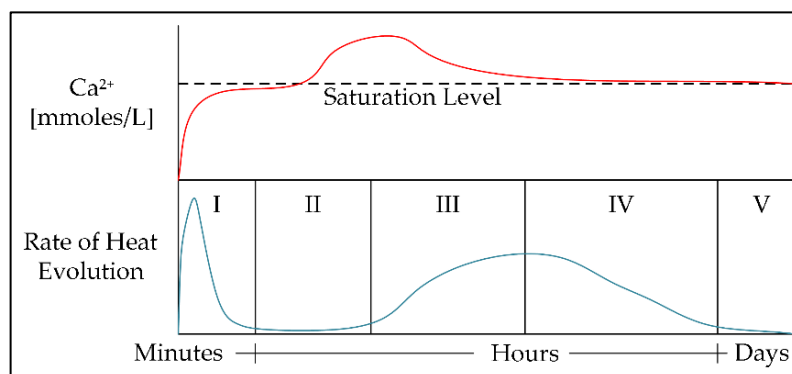
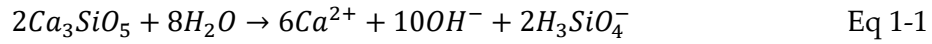


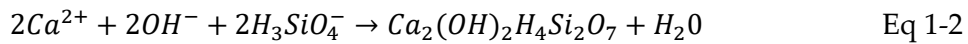
Figure 4: Simplified depiction of observations during clinker phase hydration (Nelson and Guilloit 2006).

3.2.1.1 Preinduction Period

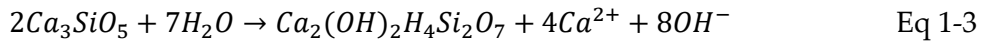
The first period, the preinduction period, starts when mixing the cement powder with water and lasts for a few minutes. A considerable heat output defines this period. This heat output stems from the wetting of the cement powder and the fast initial hydration. During this period, O^{2-} ions go into the liquid phase as OH^- ions and SiO_4^{4-} ions form silicic acid, as seen in **Eq 1-1** (P. Barret 1986).



Because the reaction of C_3S happens faster than the dissipation of the products off the surface, a layer of a C-S-H phase starts forming at the surface, as seen in **Eq 1-2**. (P. Barret 1986).



Combining **Eq 1-1** & **Eq 1-2** delivers the overall reaction taking place in the preinduction period. **Eq 1-3** shows the sum of these two equations and how, with continuing hydration, the lime content increases (Nelson and Guillot 2006).



3.2.1.2 Induction Period

As seen in **Figure 4**, after the initial exotherm, the dissipated heat declines back to zero. This period of zero heat dissipation marks the induction period. During this period, the precipitation of the C-S-H phase continues slowly, and the Ca^{2+} and OH^- concentrations increase. The actual process occurring during this induction period is still subject to discussion among cement scientists. There are multiple theories; this section only outlines the impermeable hydrate layer theory. These theories are not necessarily opposing but more complementary to one another (Nelson and Guillot 2006).

The impermeable hydrate layer theory hypothesizes, that due to the slower dissipation speed of the products of **Eq 1-1** compared to the reaction speed, an impermeable layer forms at this surface. This layer impedes the migration of water to the unhydrated reactants. It also prevents the Ca^{2+} and OH^- ions from going into the liquid phase. The build-up of this layer is the reason why the initially fast reaction comes to a halt. At room temperature, the induction period takes a few hours after which, the C-S-H layer becomes more permeable, and the hydration rate accelerates, noticeable by a rise in dissipated heat (Brown et al. 1984; Nelson and Guillot 2006).

3.2.1.3 Acceleration and Deceleration Period

After the first two periods, only a small amount of C_3S has hydrated. In the acceleration and deceleration period, commonly known as the setting period, the most hydration occurs. In the acceleration period, Portlandite $Ca(OH)_2$ crystals form, and the C-S-H phase occupies the available space, filled with water up to now. The acceleration period consumes pore space causing the total porosity to decrease. After a certain point in time, the hydration can no longer increase due to insufficient available pore space, marking the end of the acceleration period and the start of the deceleration period. Decreasing pore space and increasing hydrate deposits hinder the ion transport, causing the

hydration rate to decrease further. These two periods typically occur within several days and lead to a connection between hydrates, creating a network, and generating strength (Nelson and Guilloit 2006).

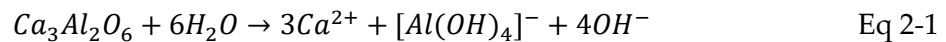
3.2.1.4 Diffusion Period

The diffusion period and deceleration period are not strictly separated. Whereas the deceleration period lasts several days, the diffusion period is indefinite. The total porosity of the cement system decreases slowly, resulting in slowed down hydration. As a consequence of this ever ongoing hydration, the system becomes denser, and the strength increases. During this period, Portlandite ($\text{Ca}(\text{OH})_2$) crystals entrap unhydrated C_3S phases. Due to this entrapment, the system can never achieve total hydration (Dent Glasser et al. 1978).

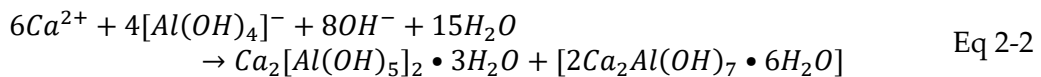
3.2.2 Aluminate Phase Hydration

Albeit that the clinker phase accounts for the most significant fraction of the cement composition, there is another phase, the aluminate phase, which is vital to early cement hydration and strength development. The aluminate phases, C_3A and C_3AF , show far more hydration at short times. This aluminate phase is responsible for the characteristic rheological properties of the cement slurry. Again, the hydration of C_3A is similar to that of C_3AF ; thus, this section only illustrates the hydration of C_3A in detail (Nelson and Guilloit 2006).

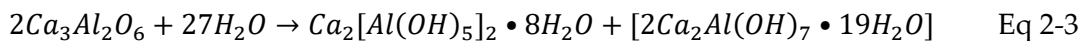
The first step of the reaction, mix water reaction with the anhydrous surface of the solids, resembles the hydration of C_3S . This hydration leads to aqueous ions in solution at the surface, as seen in **Eq 2-1** (P. Barret 1986).



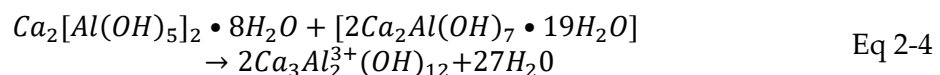
The concentration of these ions in the solution reaches saturation quickly, causing calcium aluminate hydrates to precipitate, as seen in **Eq 2-2** (Nelson and Guilloit 2006).



As with the hydration of the clinker phase, the sum of **Eq 2-1** and **Eq 2-2** shows the hydration of the aluminate phase and the formation of the calcium aluminate hydrates. **Eq 2-3** depicts this sum (Nelson and Guilloit 2006).



The calcium aluminate crystals from **Eq 2-3** materialize in a hexagonal crystal structure. At laboratory conditions, typically in several days, they react to form the more stable C_3AH_6 , which has a cubic crystal structure. **Eq 2-4** displays this transformation (Tumidajski and Thomson 1994).

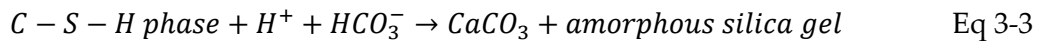
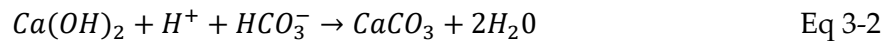
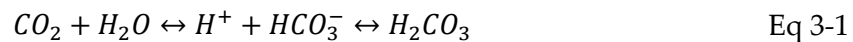


Silicate ions typically rekindle the charge imbalance within the cubic calcium aluminate crystal, resulting in Katoite ($\text{Ca}_3\text{Al}_2[(\text{SiO}_4)_{3-x}(\text{OH})_{4x}]$). The stable form of Katoite is with all charges balanced, meaning $x=3$, but x ranges from 1.5 to 3 (John W. Anthony 1995).

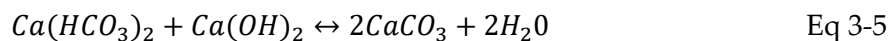
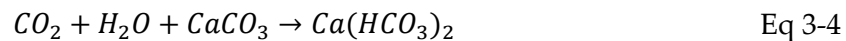
3.3 Portland Cement Carbonation

During the induction period of cement hydration, around 6% of the water content in Portland class G cement migrates out of the slurry. This expelled water is called free fluid. After pumping cement into a casing annulus, this free fluid will form in the annulus. The same free fluid build-up happens in the baseline experiment of this thesis. Once exposing the cement to carbon dioxide, a chain of reaction known as cement carbonation starts. The phenomenon of cement carbonation is well studied, and this carbonation process can destroy the integrity of a cement sheath by increasing the porosity and lowering the strength. This process is mainly dependent on the porosity of the cement. If carbon dioxide cannot diffuse into the cement, the carbonation will only affect the surface. The main issue is the feasibility of the cement mixture used in carbon dioxide EOR and storage operations. Often, the usage of high-tech cement is not possible due to the high costs. As mentioned in the CCS and carbon dioxide EOR chapter, the carbon dioxide injection happens in its supercritical form, or it will reach this form in the downhole conditions. Supercritical carbon dioxide requires less cement porosity to penetrate the surface as compared to high-density liquid carbon dioxide (Nelson and Guillot 2006).

The carbon dioxide reacts with water, forming carbonic acid, starting the process of carbonation. The water for the reaction either comes from the free fluid, inside the cement pores resulting from internal condensation or leftover water from hydration. Eq 3-1 to Eq 3-3 illustrate the main steps of this process (Onan 1984; Bruckdorfer 1986).



In this thesis, a sandstone sample kept at laboratory conditions mimics the geological formation. The sample will only contain whatever moisture it absorbs from the atmosphere. The water for the acid formation comes mostly from the cement mixing water. As mentioned above, this is either free fluid or water within the cement pores. For both experiments run in this thesis, the slurries showed a few percents free fluid per design. The aim was not to use reactive additives. The usage of reactive additives might influence the carbonation, and for the two slurries used here, carbonation was desired. As the carbonic acid diffuses into the cement pores, its dissociated ions react with calcium hydroxide and the C-S-H phase, forming new equilibria, as seen in Eq 3-4 and Eq 3-5 (Bruckdorfer 1986).



Due to an abundance of carbon dioxide, the calcium carbonate reacts with the bicarbonate. The bicarbonate is water-soluble and can migrate out of the cement when dissolved. Eq 3-5 illustrates how the bicarbonate and the calcium hydroxide react, forming water and carbonate. This water formation is why the carbonation process is detrimental to the cement integrity: the carbonation creates the water necessary to elutriate the bicarbonate. This cycle leaches cementitious material from the structure,

increasing porosity and permeability, and decreasing strength, ultimately, leading to loss of zonal isolation and well integrity. Increased temperatures favor the carbonation, and the prevention of this process is not possible without additives (Bruckdorfer 1986).

Chapter 4 Ultrasonic Detection of Cement Carbonation

One novelty of this thesis is the real-time detection of cement carbonation utilizing ultrasonic sensors. This chapter touches on the basic principle of ultrasonic analysis and explains in detail the method used in the experiments.

4.1 Physical Principles of Ultrasonic Analysis

The science of sound, also referred to as acoustics, characterizes the propagation of sound waves in solid, liquid, and gaseous media. Ultrasonics is a subsection of acoustics, referring to waves with a frequency higher than 20 kHz. These high-frequency waves enable the so-called non-destructive testing of materials. This type of testing also exercises mechanical forces on the tested material, but in such low intensity, that there is no damage to the material.

4.1.1 Piezoelectric Generation of Ultrasonic Waves

In 1880 the brother's Curie discovered the piezoelectric behavior of certain materials. These materials generate an electric charge at their surface when subjected to mechanical stress. In 1881, they discovered the inverse piezoelectric effect; when subjecting a piezoelectric material to a charge, it will change its form. These two effects are the basis for ultrasonic analysis using piezoelectric sensors. The same piezoelectric element can function as a transmitter and as a receiver. The difference is applying a charge to such an element or measuring the output charge. A prerequisite for a crystal structure to function as a piezoelectric element is that it does not have a center of symmetry. The presence of such a center of symmetry is often dependant on the temperature. The piezoelectric elements utilized for the cement analysis in this thesis work with modified lead zirconate titanate (PZT) as the piezoelectric material (Krautkrämer and Krautkrämer 1990).

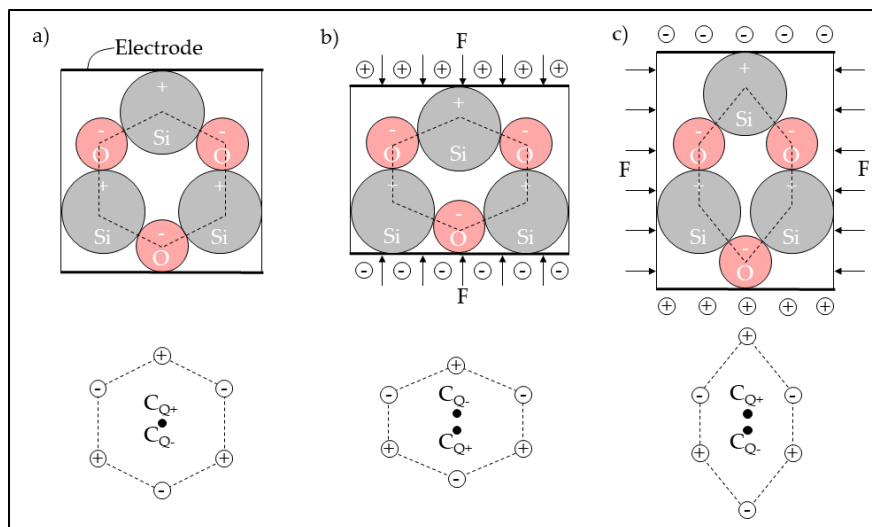


Figure 5: Simplified Quartz crystal illustrating the piezoelectric effect (Rupitsch 2019).

A rather simple way of explaining the generation of an electric charge under mechanical stress is a look at a simplified Quartz (SiO_2) crystal. Such a Quartz crystal only consists of the elements silicon (Si) and oxygen (O). There are electrodes attached to this hypothetical Quartz crystal at its respective top and bottom surface. **Figure 5** depicts such a set-up. In the first state, **a**), the Quartz crystal is in its original state, and the charges are balanced. C_{Q+} and C_{Q-} indicate the center of the positive and negative charges, respectively. In the original state, these centers are at the same geometric position, implicating that the system is electrically neutral. In state **b**), a force F causes a longitudinal and in state **c**), a transverse mode of the piezoelectric effect. Due to the force, the geometric positions of the positive and negative center of charge no longer coincide, causing the formation of a dipole. This dipole creates electric polarization depending on the distance between the centers of charge. The crystal then induces a charge in the electrodes to offset this internal imbalance (Rupitsch 2019).

The piezoelectric elements used for the cement analysis in this thesis, as seen in **Figure 6** Figure 6: The piezoelectric element utilized for the cement analysis in this thesis., consist of a modified PZT, often referred to as PIC255. Modifying means doping the crystals with ions of other elements like Nickel, Bismuth, Lanthanum, Neodymium, or Niobium. This doping enables a targeted optimization of the piezoelectric parameters of the material. The most critical aspect is Curie-Temperature. When heating the piezo element above its Curie-Temperature, it will lose its piezoelectric properties. Below the Curie-Temperature, the crystals form asymmetric tetragonal or rhombohedral crystal structures enabling the dipole formation. The Curie-Temperature of the modified PZT is between $200\text{ }^\circ\text{C}$ and $350\text{ }^\circ\text{C}$, and the manufacturer defines the operating temperature range to be $-20\text{ }^\circ\text{C}$ to $150\text{ }^\circ\text{C}$ (PI Ceramic GmbH 2020).



Figure 6: The piezoelectric element utilized for the cement analysis in this thesis.

By utilizing the inverse piezoelectric effect, the elements emit ultrasonic waves. In the set-up for the analysis in this thesis, a function generator generates the desired input function, and an amplifier delivers the electric function at a higher voltage to the piezoelectric element. There the electrodes on the surfaces of the PZT deliver electric energy, and the PZT transforms it into mechanical energy, and ultrasonic sound waves emanate. Three of these elements create the sensing array. One will generate the

ultrasonic waves, whereas two more of these elements receive refracted and reflected waves.

4.1.2 Ultrasonic Wave Propagation and Attenuation

A wave generally refers to a local disruption spreading through a medium. The term sonic, or ultrasonic, wave comes into play when this propagating disruption is pressure change. The sound moves through an elastic body through the vibration of said bodies, molecules, and atoms. Determining how the propagation of this wave changes its physical properties, is the basis of acoustic analysis.

In solids, three directions of propagation exist, depending on the particle oscillation. These three directions are longitudinal waves, shear waves, and surface waves. The waves of interest in ultrasonic testing are the longitudinal and shear waves. Longitudinal waves propagate through the oscillation of the atoms and molecules in the same direction as the wave. Longitudinal waves are also known as P-waves or pressure traction waves. These waves can propagate through all states of aggregation since the ongoing compression and expansion moves the energy through the material. Opposed to p-waves are the shear waves, also known as s-waves. S-waves cause a particle oscillation perpendicular to the propagation direction. Such a propagation depends upon a solid material; thus, these waves cannot effectively propagate in liquids and gases. **Eq 4-1** and **Eq 4-2** show the calculation of the propagation speed for p-waves and s-waves, respectively. In these equations, E_d is the dynamic Young's modulus, ρ the density, and ν_d the dynamic Poisson's ratio, all in SI-units (Burrascano et al. 2015).

$$v_p = \sqrt{\frac{E_d}{\rho} \frac{1 - \nu_d}{(1 + \nu_d)(1 - 2\nu_d)}} \quad \text{Eq 4-1}$$

$$v_s = \sqrt{\frac{E_d}{\rho} \frac{1}{2(1 + \nu_d)}} \quad \text{Eq 4-2}$$

When an acoustic wave collides with an interface between two different materials, for example, a discontinuity within the cement, a portion of the wave is reflected, whereas the remaining portion transmits into the other material. The ratio between reflection and transmission depends on the acoustic impedance of the two materials. There is a focus on the attenuation of materials later on. The higher the difference in attenuation, or acoustic impedance, the higher is the reflected portion. According to Snell's law, the angle of the original p-wave is the same as the angle of the reflected p-wave. **Figure 7** shows such a reflection and transmission scenario between two solids. All angles within **Figure 7** behave according to the law of Snellius-Descartes, as seen in **Eq 4-3**. In this equation, the velocities have the indices 1 and 2, referring to before and after the interface, respectively (Burrascano et al. 2015).

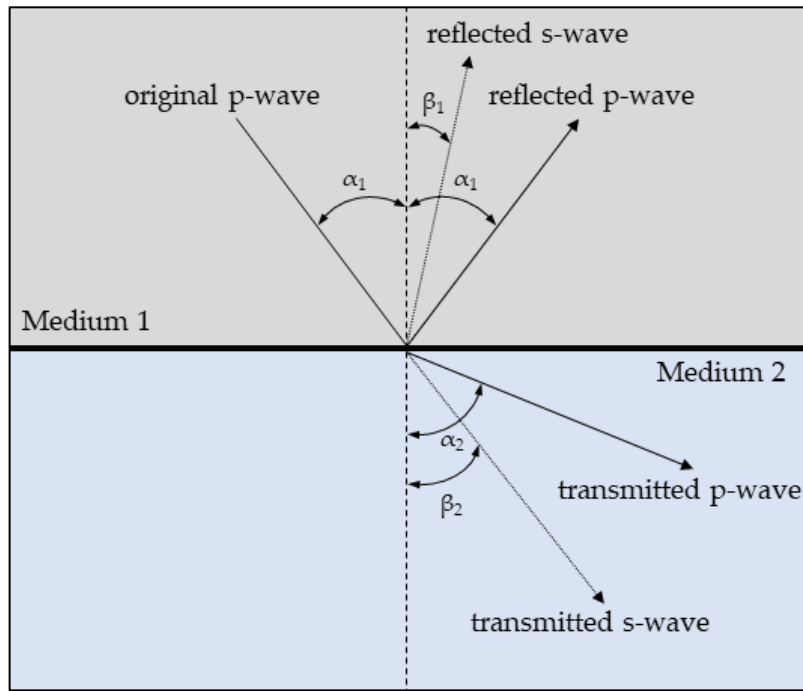


Figure 7: Graphical depiction of Snellius-Descartes law of refraction (Burrascano et al. 2015).

$$\frac{v_{P1}}{\sin\alpha_1} = \frac{v_{S1}}{\sin\beta_1} = \frac{v_{P2}}{\sin\alpha_2} = \frac{v_{S2}}{\sin\beta_2} \quad \text{Eq 4-3}$$

Three types of interfaces occur in the set-up for the cement analysis in this thesis. The first type is the interface between the transducer and receiver and the cell holding the cement. This interface is crucial, since a lousy coupling here, can lead to a loss of most of the energy. The second type of interface is between different materials, i.e., the cell and the cement or the cement and the sandstone. The third type of interface is, as mentioned before, defects within materials, leading to reflections of ultrasonic waves.

Poisson formulated a mathematical expression of a reflection and transmission coefficient, depending on the acoustic impedance, Z_1 , and Z_2 , of the two materials. These equations, Eq 4-4 and Eq 4-5, govern the transmission and reflection of an ultrasonic wave at an interface (Burrascano et al. 2015).

$$R = \frac{Z_2 - Z_1}{Z_2 + Z_1} \quad \text{Eq 4-4}$$

$$T = \frac{2Z_2}{Z_2 + Z_1} \quad \text{Eq 4-5}$$

A representative example of these factors is the interface between steel and water. Steel has an acoustic impedance of $Z_1=45 \cdot 10^6 \text{ kg/m}^2\text{s}$ and water of $Z_2=1.5 \cdot 10^6 \text{ kg/m}^2\text{s}$. Using these values in Eq 4-4 and Eq 4-5 delivers $R=-0.935$ and $T=0.065$. These numbers mean that at this interface, 93.5% of the wave energy reflects (the negative annotation indicates the phase reversal of the wave), and only 6.5% transmit through the interface into the water and propagate further (Krautkrämer and Krautkrämer 1990).

A common practice in acoustics is the generation of a logarithmic scale to depict the large variations in specific quantities. These quantities are the intensity of the acoustic wave

and its acoustic pressure. Calculating the sound pressure requires much information on the wave and this information accessible at the receiving side. Estimating the intensity of the wave, on the other hand, is possible. A method of approximating this intensity utilizes the power generated by or supplied to the piezo element. This calculation assumes that the maximum intensity of the wave cannot exceed the maximum power supplied to the piezo element. The basis of this calculation is electronics since a piezo element acts as a capacitive element in a circuit. The peak-to-peak voltage, frequency, and capacitance of the piezo element are the basis of this calculation. Eq 4-6 to Eq 4-10 illustrate the calculation of the current and power in the piezo element (Fleming 2009).

The maximum and minimum current of a sinusoidal wave is equal to (Fleming 2009):

$$I_{max,sine} = \pm V_{pp} \pi f C_p \quad \text{Eq 4-6}$$

The root-mean-square current derives from the maximum current. All calculations use root-mean-square values of voltage and current since it represents the effective value of such time dependant quantities.

$$I_{RMS} = \frac{I_{max,sine}}{\sqrt{2}} \quad \text{Eq 4-7}$$

$$V_{RMS} = \frac{V_{pp}}{\sqrt{2}} \quad \text{Eq 4-8}$$

$$P = V_{RMS} * I_{RMS} \quad \text{Eq 4-9}$$

$$I = \frac{P}{A} \quad \text{Eq 4-10}$$

The intensity calculated above is the basis for the evaluation of the sound level. In acoustics, it is common to express the ratio of the sound levels in Decibels. The reference is the intensity supplied to the transmitting piezo element, I_0 (Lerch et al. 2009).

$$L_p = 10 \log \left(\frac{I}{I_0} \right) \quad \text{Eq 4-11}$$

4.2 The Set-up

As described earlier, to generate an acoustic wave with piezoelectric elements, applying an electric signal to the element is necessary. For this thesis, an oscilloscope with an integrated function generator enables the evaluation of the sensor data and supplies the signal. An arbitrary waveform consisting of a two-cycle square wave is the basis. This two-cycle square wave has a frequency of 250 kHz and pulses every second. The generated function has a peak-to-peak voltage of 4 V, and the piezo element can withstand voltages in a range of -100 to 400 V. An amplifier with a gain of 20 amplifies the signal, effectively delivering a peak-to-peak voltage of 80 V. Not offsetting the function, generates the desired contractions and expansions in the element. The negative and positive peak of the sine wave is at 40 V. For cement analysis, this wave design showed promising results, with a decrease in the intensity of 11.5 dB/cm. The receiving elements connect to the oscilloscope, which collects the data. The element in use for this analysis is flexible. This flexibility ensures that the signal is transmitted nicely into the cell since the cell is cylindrical, and the element needs to adapt to the curvature.

Figure 8 depicts a schematic of this set-up and shows the position of the transmitter and receiver on the cell. Using high-temperature resistant tape together with ultrasonic coupling gel, delivered the best result in fixing the piezo elements to the cell. Measuring the acoustic travel time happens by attaching one receiver on the opposite side of the transmitter. Deducting the travel time of the cement happens, by deducting the previously collected travel times of the PEEK (polyether ether ketone) polymer, the carbon dioxide in the center, and the sandstone. The other receiver's position is below the transmitter. This receiver collects reflections. Changes in the cement cause changes in the reflection enabling structural health monitoring of the cement. Specific material properties correlate with the ultrasonic travel time. One such property in cement is its compressive strength—the compressive strength of fresh cement increases as the cement sets. Also, acoustic travel time decreases as the cement sets. The better connected the molecules within the cement are, the better the propagation of a p-wave is. The execution of a baseline test helps correlate compressive strength values of different cement ages and densities to their corresponding sonic travel times measured with this set-up.

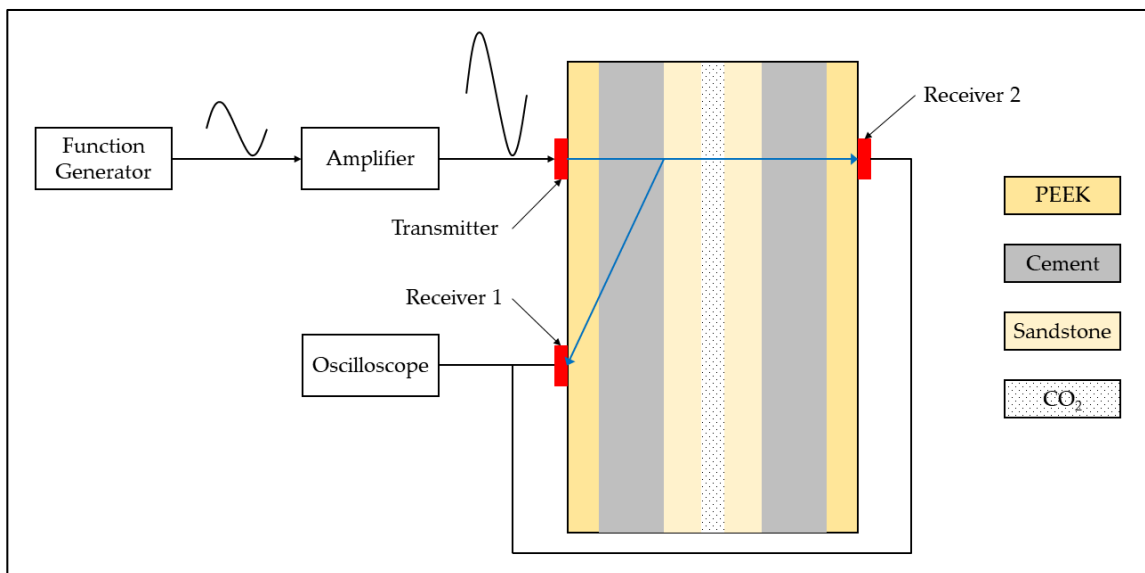


Figure 8: Set-up of the ultrasonic sensing system.

4.3 Compressive Strength Baseline Testing

A series of baseline tests help establish a better understanding of the results acquired with the ultrasonic set-up. Not only that, but it also provides a method to gauge the set-up. As previously stated, the compressive strength of cement increases over time and correlates with the increase of the sonic velocity of the cement. A 14 ppg and a 16 ppg neat class G cement slurry are the basis. Filling this slurry into cylindrical molds provides the hardened cement samples with 27 mm diameter and 54 mm length. The evaluation of the acoustic travel time and the compressive strength took place after 4, 6, 8, 10, and 12 days of curing. A destructive compressive strength tester supplied the compressive strength data of the samples. The evaluation of the acoustic travel time uses the one-cycle sine wave described earlier. A clamp and ultrasonic coupling gel establish a sufficient connection between the elements and the sample—the transmitter on one

face of the cylinder and the receiver on the other. **Figure 9** shows the oscilloscope reading of such an acoustic travel time evaluation. The red line is the voltage monitor of the amplifier output and depicts the voltage before gain. The blue line is the output of the receiving piezo element. The zoomed-in graph depicts which peak marks the arrival time. The choice for this peak comes from it being the first peak to show a decisive increase compared to the neutral. The time between the peak of the sine wave and the chosen peak of the receiver comes to 32.3 μs . The calculation delivered an acoustic velocity for this cement sample of 1889 m/s after four days of curing. This sample is not part of the tests shown on the next page because a compressive strength test did not take place.

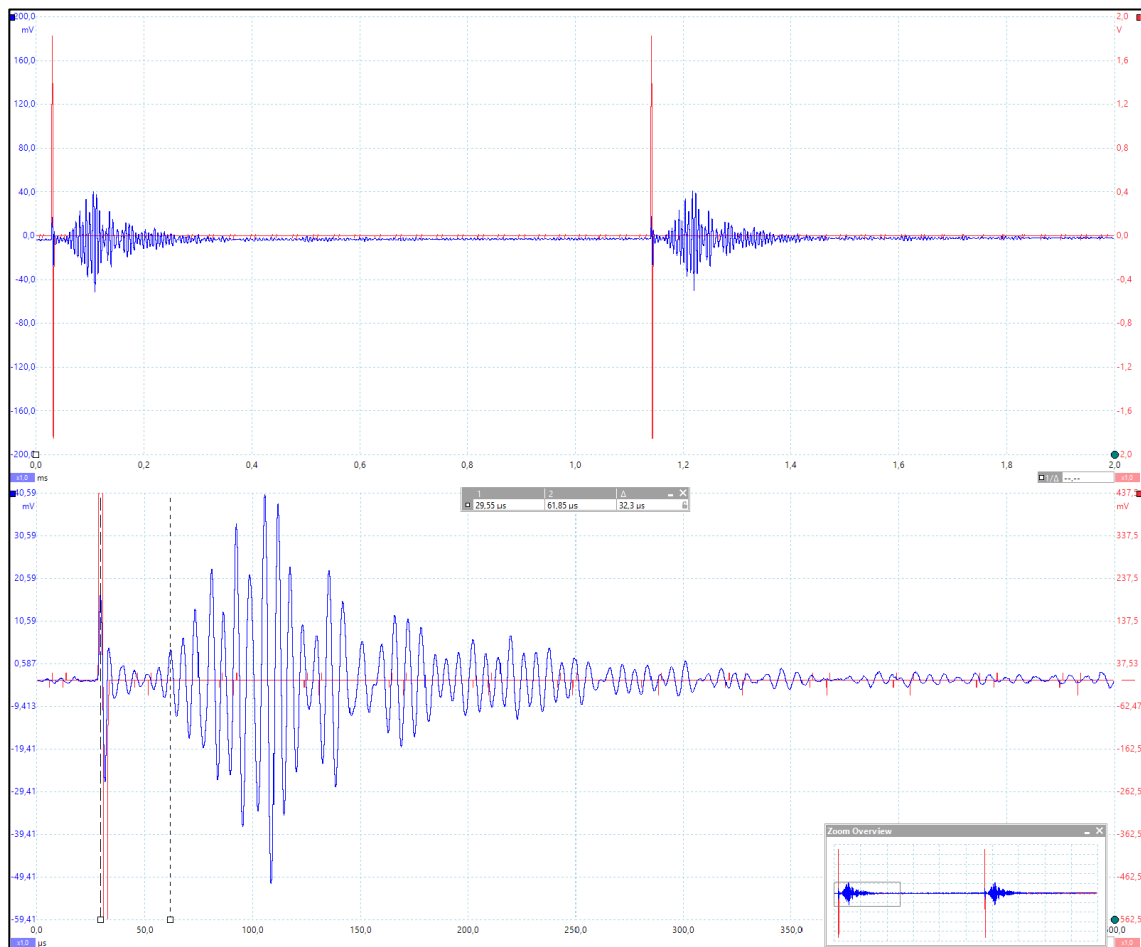


Figure 9: Evaluation of acoustic travel time in cement samples with different curing times.

Data gathering occurred with a 14 ppg and 16 ppg neat class G slurry and 15 ppg and 16 ppg class G slurry with 5% added Bentonite by weight of cement. To account for the water need of the Bentonite, an addition of 4.5% water per percent of Bentonite took place. Pouring the slurries into molds delivered the desired cylinder used for the compressional strength analysis. Before conducting the analysis, sanding the top and bottom of the cylinder ensured plane-parallel surfaces. The compressional strength testing machine requires this plan-parallelity. The piezo elements used for the acoustic analysis attach to the surfaces of the cylinders using a clamp and ultrasonic coupling gel.

Trying different frequencies and waveforms helped in finding the most suitable configuration. **Figure 10** shows a graphical depiction of the data collected during this analysis.

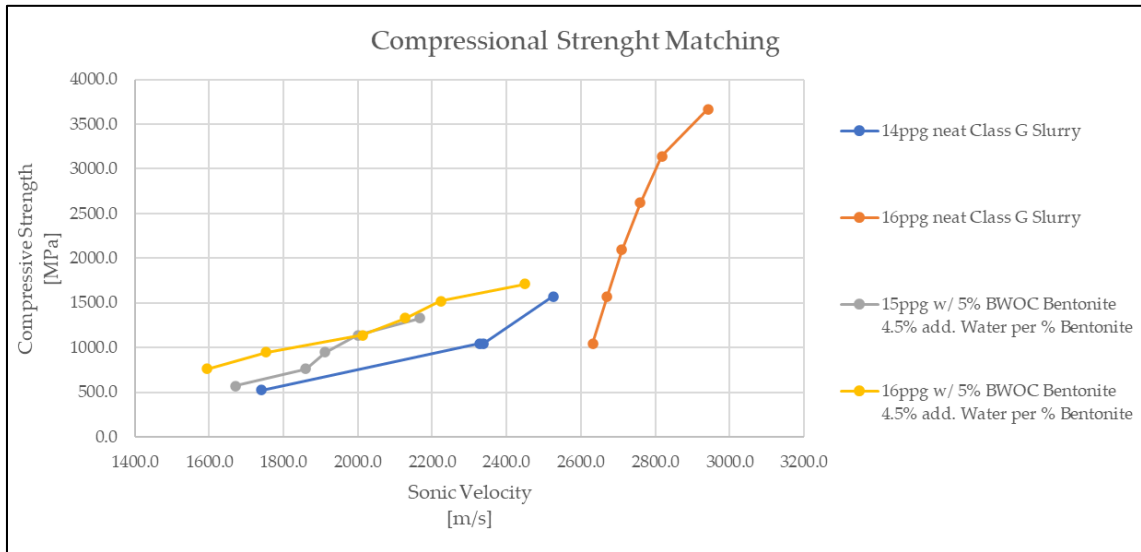


Figure 10: Graph showing the matching of sonic velocity to compressional strength for different density samples and periods of curing-.

As seen in the graph above, the increase in acoustic velocity correlates with an increase in compressive strength. Using the acoustic velocity to determine the compressive strength of a cement requires data of said cement. The only cement composition not behaving like the others in this baseline test was the neat 16 ppg slurry. While the other slurries exhibit a substantial increase in sonic velocity, this slurry only increases by about 350 m/s. Since the testing started at day four of curing for these samples, the compressive strength was already quite well developed. The 16 ppg slurry most likely hydrated faster in these four days, so that it was already an excellent acoustic conductor for the first test.

Chapter 5 Experiments

Every chapter leading up to this chapter explained the details of cement reactions and tools used to monitor reactions within the cement. The focus here lies on the set-up of the testing cell, the slurry preparation, and the analysis of the samples before, during, and after carbonation.

5.1 Previous Research on Oil Well Cement Carbonation

First, selected previous research shows approaches attempted in the past. The mention of this previous research will highlight the novelty in the real-time monitoring approach in this thesis.

5.1.1 Jobard et al. – Effect of Water and Supercritical CO₂ on Caprock/Cement Interface

Jobard et al. focused on the effect of supercritical carbon dioxide on the interface between a Callovo-Oxfordian clay rock and Portland class G cement. The slurry preparation happened according to API RP-10B-2. For their samples preparation, they placed a 25x17x10mm hydrated caprock sample in the middle of a 35x30x20mm silicone mold. After 24 hours of setting, they removed the silicone. After the setting period, Jobard et al. placed the samples in a reactor filled with a NaCl solution. The reactor simulated conditions of 100 bar and 80 °C, and they removed the first sample after seven days. In total, they cured eight samples for up to 30 days, either in solution, dry Nitrogen, or dry supercritical carbon dioxide. It is noteworthy that every time they removed a sample, a depressurization of the reactor, and the remaining samples, occurred. Their findings included alteration mechanisms, e.g., carbonate precipitation, cracking of the cement, and leaching of calcium-bearing phases. They also found that supercritical carbon dioxide leads to much stronger carbonation (Jobard et al. 2018).

5.1.2 Aiex et al. – Effect of Static CO₂ on Cement under High-Pressure & High-Temperature Conditions

Aiex et al. deduced an intermediate step in the carbonation reaction, by submerging the samples in carbonic acid and applying pressure with carbon dioxide onto the carbonic acid bath. The conditions inside the chamber were 137.9 bar and 73.9 °C. The samples used in their study were cement formulations, including different cement classes and a broad array of additives, i.e., viscosifiers, fluid-loss additives, expansion additives, dispersants, and more. The exposure time here goes up to one year. They also depressurized the chamber to withdraw samples for mechanical and chemical analysis. Amongst other observations, they concluded that reduced Portland cement mixed with freshwater delivered the best results after exposure in terms of strength (Aiex et al. 2015).

5.1.3 Lacerda et al. – Monitoring the Carbonation Front Progress

The aim of Lacerda et al. was to document the front of the cement carbonation using pH-probes and μ -CT scans. The cement prepared for this study was a high early strength Portland cement mixed with sand in a 1:3 ratio. They prepared 11 cylinder specimens with a diameter of 2 cm and a length of 4 cm. Lacerda et al. determined the baseline with one specimen, and the remaining 10 went into the curing chamber. The exposure here was not with supercritical carbon dioxide, but in a curing tank with 5% carbon dioxide, 28 °C, and relative humidity of 65%. They removed the specimens over a range of 25 days and conducted the pH and μ -CT analysis. One inexpensive method utilized here is the usage of phenolphthalein indicator to visualize the carbonation front on the samples. Lacerda et al. concluded that the indicator is not able to provide information on the carbonation of the innermost region, but that pH-values and binarized μ -CT scans lead to a much greater understanding of the carbonation (Lacerda E. et al. 2017).

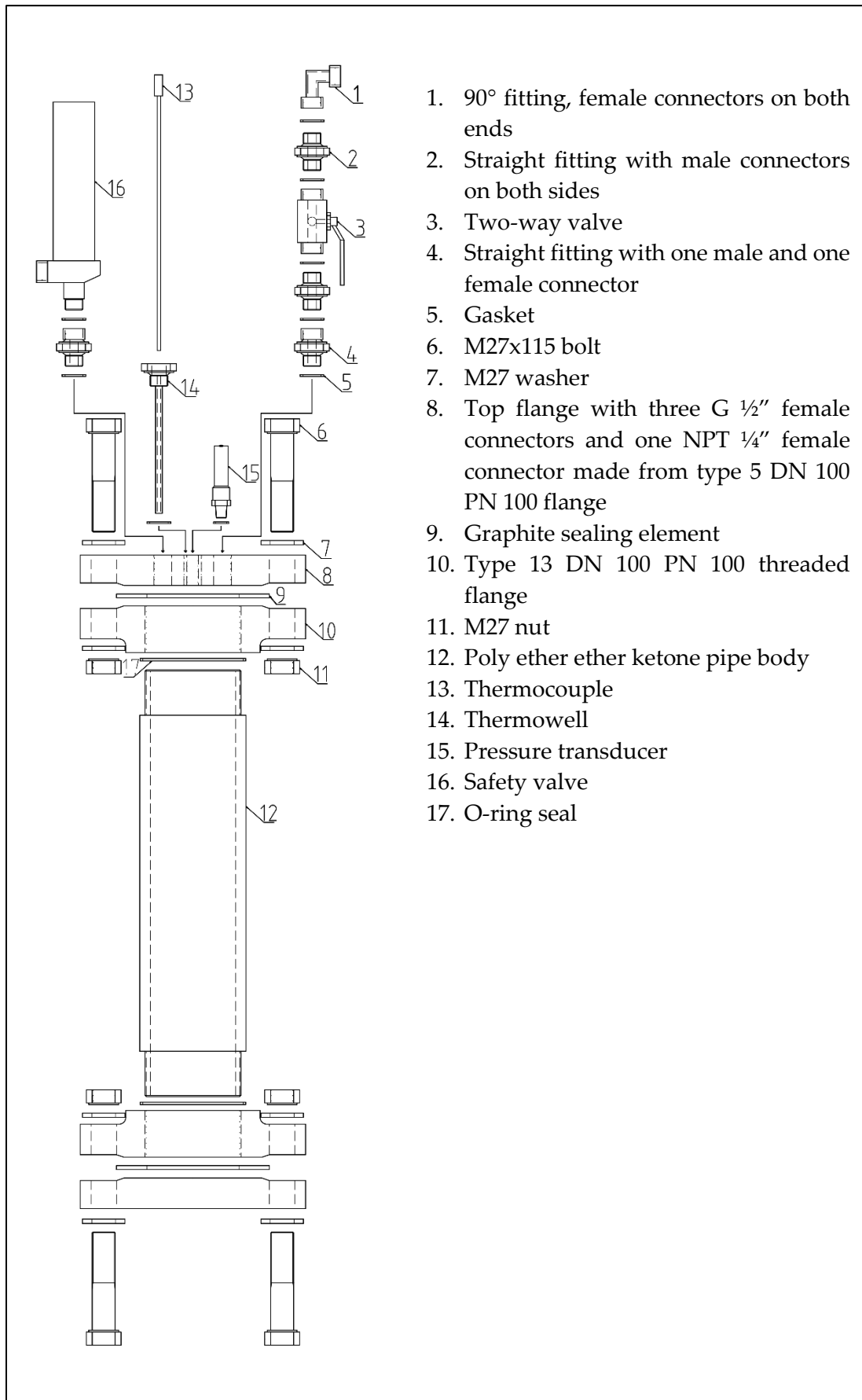
5.2 Construction of an Autoclave facilitating Real-time Carbonation Monitoring

The novelty of the set-up in this thesis lies in the ability of real-time monitoring of the cement carbonation, without disturbing the sample inside. This section discusses the design, construction, and testing of the autoclave enabling the experiments.

5.2.1 Designing the Autoclave

The utmost important requirement for this autoclave was the ability to use it in a medical CT-scanner. There are no developed methods to monitor the carbonation of oil well cement continuously. Thus, the CT-scans picture the inside of the autoclave and help develop other measurements capable of monitoring the carbonation. The issue here is that autoclaves typically comprise of steel or other metals, which render a CT-scan of the inside impossible. Constructing the pipe body from polyether ether ketone (PEEK) enables CT-scans. The design called for the monitoring of cement under conditions causing carbon dioxide to reside in its supercritical state. The configuration of the autoclave permits a maximum pressure of 100 bar and a maximum temperature of 120 °C. The PEEK, as well as other components, permit temperature of up to 350 °C, but sealing elements and other mountings limit this temperature at the moment.

Figure 11 shows a plan of the autoclave in the form of an exploded view. The first design remained largely the same during all stages of construction. Necessary alterations included the change to different types of fittings to ensure all appliances find space on the top flange. In a first design, the aim was to build a tapered thread on the pipe and establish a gas-tight connection to the threaded flange solely by torquing the tapered thread. This design changed quickly since the force necessary to tighten the connection was substantially too large. The choice fell to a straight thread and establish a gas-tight seal via thread glue, thread sealing rope, and Teflon tape. All of these methods did not deliver the desired results. The final design includes an o-ring groove on the shoulder below the thread, and the gas-tight connection originates from the compression of this o-ring between the threaded flange and the shoulder of the pipe-body.



1. 90° fitting, female connectors on both ends
2. Straight fitting with male connectors on both sides
3. Two-way valve
4. Straight fitting with one male and one female connector
5. Gasket
6. M27x115 bolt
7. M27 washer
8. Top flange with three G 1/2" female connectors and one NPT 1/4" female connector made from type 5 DN 100 PN 100 flange
9. Graphite sealing element
10. Type 13 DN 100 PN 100 threaded flange
11. M27 nut
12. Poly ether ether ketone pipe body
13. Thermocouple
14. Thermowell
15. Pressure transducer
16. Safety valve
17. O-ring seal

Figure 11: Exploded view of the autoclave, including all components.

5.2.2 The construction of the Autoclave

The standard EN 10226-1 has the specifications for the flanges used for the construction of this autoclave. Using standardized steel flanges reduces cost and necessary lead time. The PEEK pipe-body comes in the form of a pipe. Cutting this pipe to the desired length of 50 cm and threading it delivers the necessary pipe. As described earlier, the most efficient and easy to use gas-tight seal is the usage of an o-ring together with an o-ring groove in the PEEK pipe-body. This design makes it easy to assemble and disassemble the autoclave. The graphite sealing elements are standard gaskets as used in most pressure devices requiring gas-tight connections. Reusing the elements is possible, but a visual inspection is always necessary to make sure there is no damage. The same goes for the sealing surfaces on the flanges. If damage occurs on these surfaces, a gas-tight connection is most likely no longer possible. Closing off the top and bottom flange must happen according to the standard and carried out by a trained professional (DIN EN 10226-1:2004-19).

The construction of this autoclave occurred under the goal to reuse every part in every experiment. There are no waste parts since the cement does not bond to the PEEK polymer. The most important part is to repeat pressure testing after every disassembly of the threaded flanges from the PEEK pipe-body.

5.2.3 Testing the Autoclave

Multiple pressure tests using water established that the autoclave holds the design pressure. The execution of the tests utilized a hand pump capable of supplying 120 bar pressure. The highest pressure tested was 95 bar, since the safety valve actuates at 97 bar with an error of 3% and there is no benefit in causing an intended actuation. **Figure 12** illustrates the pressure decay during the first pressure test. The autoclave proved to seal sufficiently. The observed decay most likely stems from air pushed into the cell when pressurizing since there was no vacuum inside.

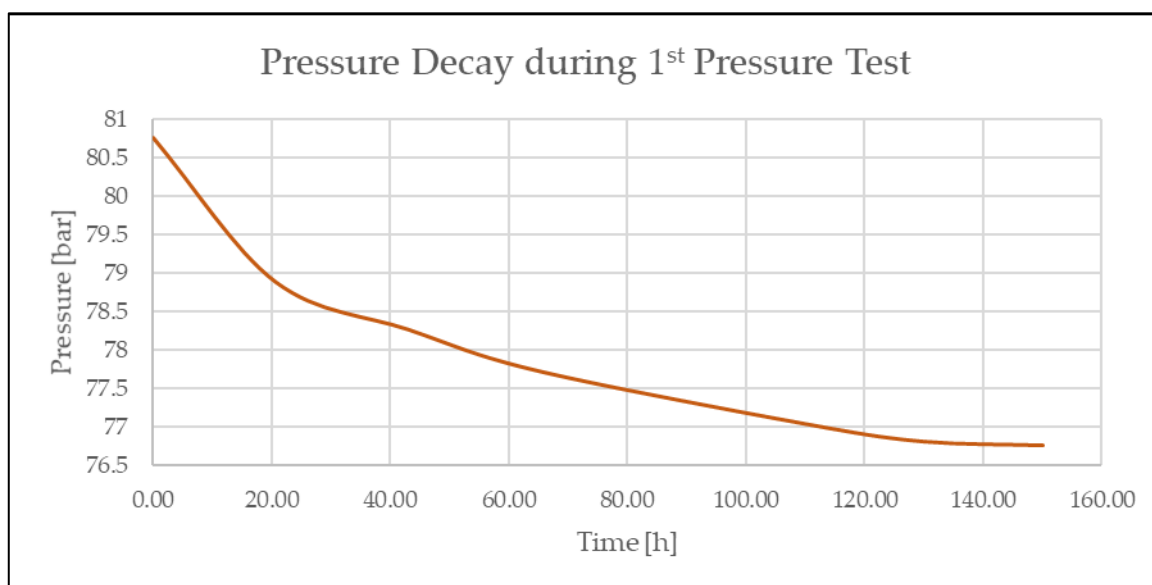


Figure 12: Graphical depiction of the pressure decay during the first pressure test.

5.3 Future Designs

The first ideas included a pressurized autoclave into which the displacement of cement occurred. Since the primary aim of this study is to find ways to monitor the cement carbonation, realizing these designs will happen later on. Constructing such an autoclave involves even more challenging concepts. When pumping a liquid slurry into the cell, check valves or other closing devices are required to keep the slurry from coming back out of the autoclave. On top of additional valves required, a displacement pump, as well as suitable flow lines, are necessary.

Another design, with a realization after the baseline tests, includes a dynamic carbonation monitoring. In this design, a backpressure valve on the bottom flange of the autoclave enables flow through the sample. Such design mimics real-life conditions even more closely since reservoirs always exhibit a certain degree of flow. How fast this flow is, depends on the experiment and can be determined as desired. This design would also enable the usage of the ultrasonic measurements to measure the flow inside the autoclave. In addition, an analysis of the discharged fluid and gas can help understand the speed of carbonation and elutriation of carbonate.

5.4 Experiment Procedure

In this section, a step by step outline of the procedure defines how to carry out the carbonation experiment. Defining such a procedure ensures a standardized way of conducting the experiment to guarantee reproducibility.

1. Slurry Mixing:
 - a. Mix cement slurry in the simulated batch mixer (prepare 7l, 3.2 l for the autoclave, and 3.8 l for slurry testing).
 - i. The batch mixer utilizes a stirrer, as seen in **Figure 13**.
 - ii. The batch mixer has three RPM settings: 197, 317 & 462.
 - iii. A stainless steel container, as seen in **Figure 14**, holds the slurry.



Figure 13: Stirrer utilized to mix the cement slurry in the batch mixer.



Figure 14: Stainless steel container used for slurry mixing in the batch mixer.

- iv. The mixing procedure consists of adding the liquid components into the container while mixing at 197 RPM and setting the speed to 462 RPM afterward. Adding the dry components uniformly into the stirred liquid ensures even distribution. Mixing the ingredients for 10 min establishes a proper slurry.
2. Preparing the autoclave:
 - a. Place the o-ring onto both threads of the PEEK pipe body.
 - b. Apply thread sealant to the flange threads and the pipe threads.
 - c. Screw the flanges onto the PEEK pipe body. Tightening by hand is sufficient to engage the o-ring seal.
 - d. Place the graphite sealing element onto one of the flanges and attach the blind flange. Tighten the bolts according to **Figure 15**.
 - e. Grease the inside of the PEEK body with high-temperature resistant grease to ensure easy removal of the cement after the carbon dioxide exposure.
 - f. Mount the formation core, according to **Figure 16**, using the core-centralizer. **Figure 17** depicts this placement.

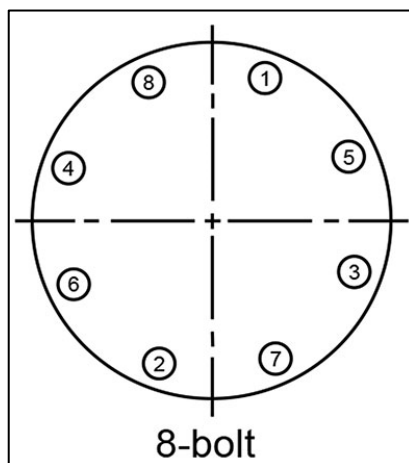


Figure 15: Sequential order to tighten bolts on flanges to ensure a gas-tight seal.

Experiments

- g. Fill the autoclave with cement slurry using a funnel and moving it in a circular pattern along the annular space to ensure uniform placement.

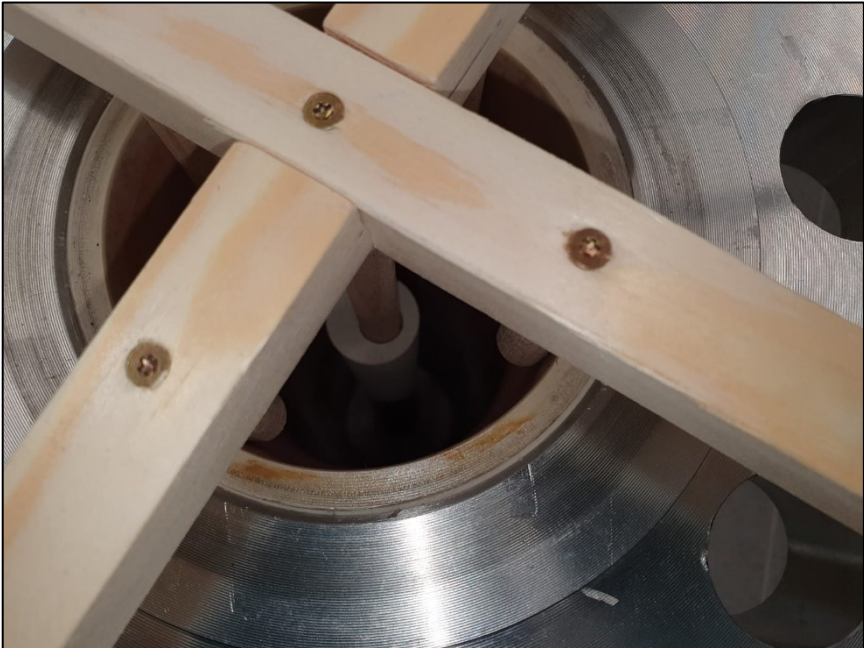


Figure 17: Core-centralizer used to place the formation core in the center of the autoclave.

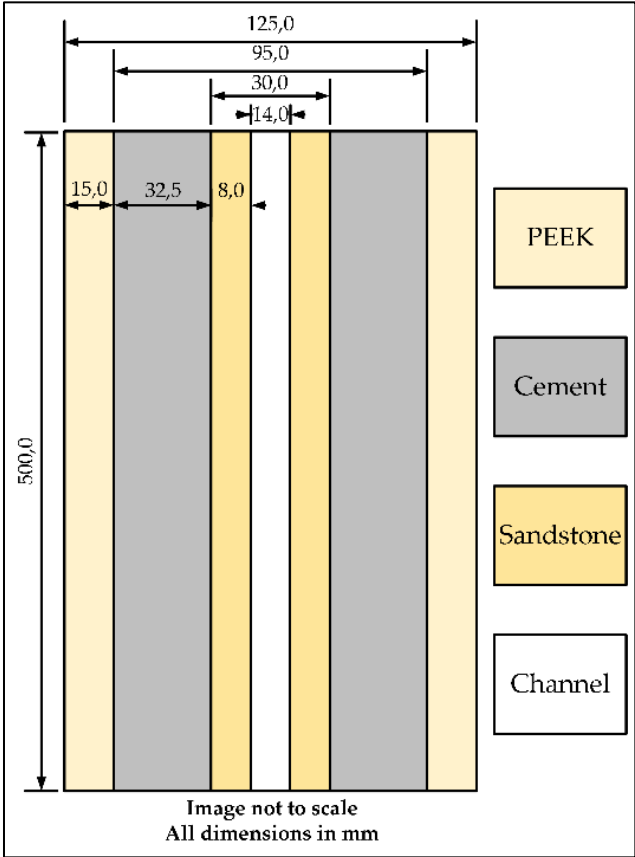


Figure 16: Schematic of the placement of the formation core inside the autoclave.

3. Conditioning the Slurry
 - a. Place the autoclave on the vibrating table and condition cement for 30 min. Preliminary experiments showed that this duration most accurately mimics the API RP 10B-2 slurry preparation scheme. **Figure 18** illustrates the vibrating table used for conditioning the cement after pouring it into the autoclave.
 - b. Place the stainless steel mixing container with the rest of the slurry on the vibrating table for conditioning, also for 30 min.

4. Conducting Conventional Slurry Tests:
 - a. Remove the stainless mixing container from the vibrating table.
 - b. Measure density and rheology of slurry (API RP 10B-2).
 - c. Start thickening time and UCA test (API RP 10B-2).
 - d. Start stirring fluid loss and free fluid test (API RP 10B-2).
 - e. Start the sedimentation test (API RP 10B-2).
 - f. Pour conditioned slurry into 12 cylindrical molds with 1" diameter and 2" length (these samples are for XRD/SEM and mechanical properties testing).
 - g. Evaluate stirred fluid loss and free fluid test (API RP 10B-2).
 - h. Evaluate the UCA and thickening time test (API RP 10B-2).
 - i. Evaluate the sedimentation test (API RP 10B-2).

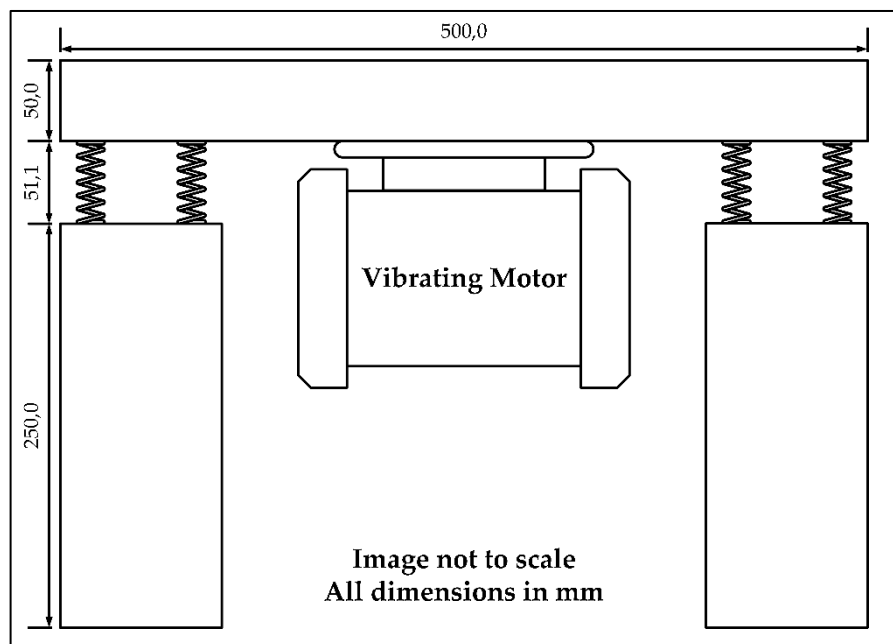


Figure 18: Schematic of the vibrating table used for cement slurry conditioning.

5. Curing the cement slurry in the autoclave.
 - a. Remove the autoclave from the vibrating table
 - b. Attach ultrasonic sensors to the outside of the pipe body and start recording the continuous sensor output.

Experiments

- c. Extract possible free fluid from the top of the cement sheath after 2 hours of curing. The goal should be to design a slurry without any free fluid.
- d. After 24 hours, move to e. Depending on the slurry, 24h does not guarantee the desired degree of curing. Refer to ultrasonic readings in comparison with UCA data to determine at what time the slurry has the required degree of curing.
- e. Close the top flange of the autoclave.
 - i. tighten bolts in 4 steps of the required torque of 250 Nm (25%, 50%, 75% & 100% of required torque). This tightening is done in a sequential bolt order, as seen in **Figure 15**.
 - ii. During the curing period, keeping the autoclave upright ensures that the liquid slurry does not change the position of the formation core with the autoclave. Including a centralizer in the top flange would enable putting the autoclave into a horizontal position right after filling the slurry, since the centralizer keeps the formation core in place.
 - iii. When the cement reaches the desired degree of curing, placing the autoclave in a horizontal position on the platform lift together with all appliances, ensures more accessibility and safer operations. **Figure 19** shows the position of the autoclave on the platform lift together with the appliances.

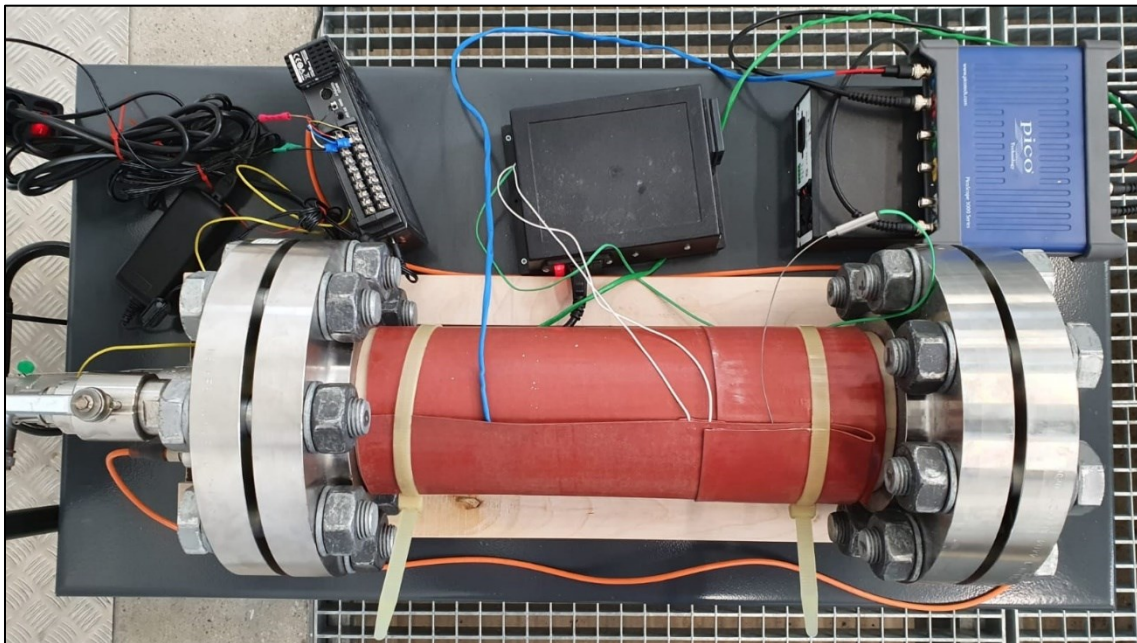


Figure 19: Position of the autoclave with appliances on the platform lift for the duration of the experiment.

6. Injecting carbon dioxide and evaluating the integrity of cement slurry in the autoclave.
 - a. Align the vacuum pump to autoclave and apply a 0.025 bar vacuum. Applying the vacuum helps in eliminating additional parameters influencing the carbonation. By doing so, the air (and its reactive components) leave the cell.
 - b. Close the ball valve to trap the vacuum.
 - c. Align the carbon dioxide bottle, open the ball valve, and apply 50 bar pressure (refer to f.)
 - d. Close the ball valve to shut-in the autoclave and establish a gas-tight, closed system.
 - e. Attach the heating jacket using temperature resistant zip ties (**Figure 19** shows the final set-up).
 - f. Heat the cell to 80°C to achieve supercritical conditions for carbon dioxide inside the autoclave. Calculating the precise pressure inside the autoclave resulting from the heating is not possible since the autoclave does not contain pure carbon dioxide. If a better vacuum can be achieved, and the pressure lowered to at least 20 mbar, the equation for isochoric processes stated, later on, could deliver accurate results.
 - i. The graphite sealing elements between the flanges, together with sealing elements in the threaded flanges ensure a gas-tight system.
 - ii. The carbonation consumes carbon dioxide, most likely leading to a pressure decay. The safety margin of roughly 10 bar gives room for pressure drop, while still being in the supercritical region of carbon dioxide. The pressure transducer in use has a full range of 103,4 bar with an error of 0,25% across the full range. This error leads to possible measurements of ca. 250 mbar. With this accuracy, interpretations of the molecular consumption of carbon dioxide are possible.
 - g. From this point, monitoring of pressure & temperature, as well as ultrasonic readings takes place.
 - h. Conduct first CT-scan.
 - i. Conduct CT scans according to carbonation speed (anticipated is one scan per day).
 - j. After 2 to 4 weeks (or earlier/later, depending on the degree of carbonation), the experiment comes to an end.

 7. After carbon dioxide Exposure:
 - a. Relieve the pressure. A needle valve attached to the 2-way ball valve enables an accurate way to relieve the pressure.
 - b. Loosen top flange.
-

- c. Remove cement and sandstone core from PEEK pipe
- d. Drill 12 1" diameter and 2" long cores from the cement sheath (these samples are for the mechanical analysis). The process for this is the usage of a coring bit. This coring bit needs to be actively cooled using water.
- e. Drill one horizontal core to also have a sample of the sandstone-cement interface for the chemical analysis.

5.5 Risk Assessment of the Testing Procedure

In order to guarantee the safest possible method of operation, this section focusses on a thorough risk assessment and possible mitigations. The method used in this assessment comprises of three steps. In the first step, the identification of risks associated with all operations takes place. This step is followed by an evaluation of the seriousness of the risks according to a risk matrix. In a final step, the mitigation of risks that pose a severe threat takes place.

5.5.1 Determining the Legal Basis of the Autoclave

Before identifying and evaluating the risks associated with the operation of the autoclave, it is crucial to determine the legal basis of it. In Austria, the pressure equipment monitoring regulation (in German: Druckgeräteüberwachungsverordnung, DGÜW-V) determines this legal status. This regulation divides pressure equipment into low- and high-risk equipment, depending on the medium within, the volume, the maximum allowed pressure, and the pressure containment product. The pressure containment product is an index without dimension resulting from the multiplication of pressure in bar and volume in liter. If the equipment in question falls into the high-risk category, a governmentally approved testing institution needs to carry out periodic examinations. In the case of low-risk equipment, the operator is in charge of the risk assessment and the examinations (Österreichische Bundesverfassung 2004).

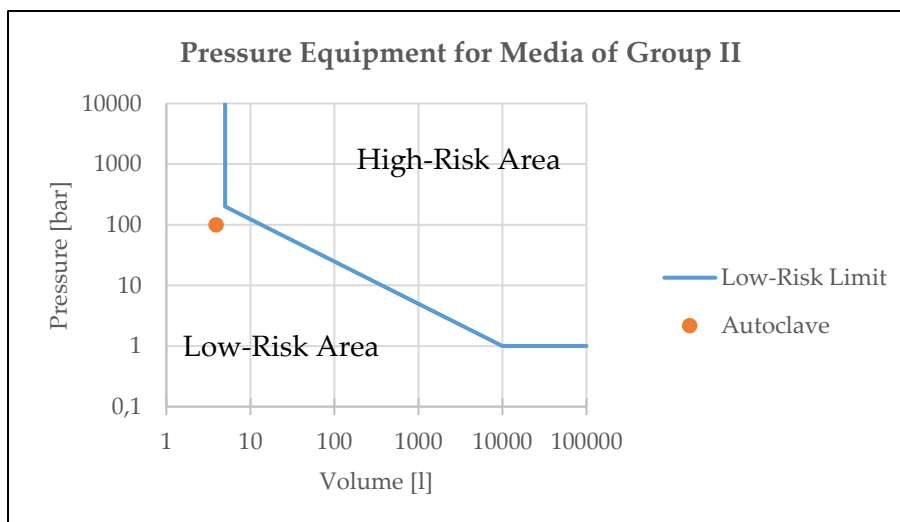


Figure 20: A schematic showing the distinction between low- and high-risk pressure equipment containing media of group II.

The first differentiation is between the media of group I and group II. The essence here is that media of group I pose serious safety hazards, whereas media of group II does not pose such a hazard. The medium within the autoclave in the experiments for this thesis is carbon dioxide and corresponds to a medium of group II. The second differentiation is in size. The regulation, as mentioned above, defines multiple classes according to the volume, maximum allowed pressure, and the pressure containment product. Knowledge of the group of the medium and the size and maximum allowed pressure leads to a definitive classification (Österreichische Bundesverfassung 2004).

The autoclave used in this thesis has a maximum allowed pressure of 100 bar and a total volume of 3.93 liters, resulting in a pressure containment product of 393. Pressure equipment filled with a medium of group II poses a high-risk if all of the following are true: a maximum allowed pressure greater than one bar, a volume greater than 5 liters, and a pressure containment product greater than 1000. This pressure containment product has the unit of bar*liter, but its only usage is legal status determination. Since two of these are not valid for the equipment in question, the legal status is that of pressure equipment posing low-risk. **Figure 20** depicts a graphical representation of this distinction (Österreichische Bundesverfassung 2004).

5.5.2 Risk Identification and Evaluation

Table 4 shows all risks associated with the operation of the autoclave split into the seven phases, as mentioned in the procedure. Assigning each risk a likelihood of occurrence and severity of impact enables the placement within a matrix. **Figure 21** shows the matrix used for the evaluation. Each field in this matrix refers to a product of likelihood and severity and classifies risks into low, mid, upper, and high. High-, upper-, and mid-risks require mitigation. The goal is that the remaining risk after mitigation classifies as low. This assessment does not include risks associated with the operation of machinery and equipment associated with the slurry analysis and the chemical and mechanical analysis of the specimens.

Procedure Phase	Risk No.	Task	Risk	Likelihood [1-5]	Severity [1-5]	Classification [1-25]
1	1.1	Slurry mixing	Loose hair or clothing getting caught in the stirrer	3	4	12
2	2.1	Autoclave assembly	Dropping heavy objects	2	3	6
3	3.1	Slurry conditioning	Stainless steel container or autoclave dropping off the vibrating table	2	3	6
5	5.1	Attaching ultrasonic sensors	Electrification	2	3	6
5	5.2	Injecting nitrogen	Nitrogen leak	2	1	2
6	6.1	Injecting carbon dioxide	Burst of the autoclave	1	5	5
6	6.2	Injecting carbon dioxide	Carbon dioxide leak	2	1	2
6	6.3	Heating the autoclave	Burst of the autoclave	1	5	5
6	6.4	Conducting CT scans	Dropping heavy objects	2	3	6
7	7.1	Relieving pressure	Carbon dioxide emission	5	1	5
7	7.2	Loosening flanges	Dropping heavy objects	2	3	6
7	7.3	Removing cement and formation core	Dropping heavy objects	2	3	6
7	7.4	Drilling test specimen	Loose hair or clothing getting caught in the drill	3	4	12

Table 4: Risk evaluation for the operation of the autoclave for continuous carbonation monitoring.

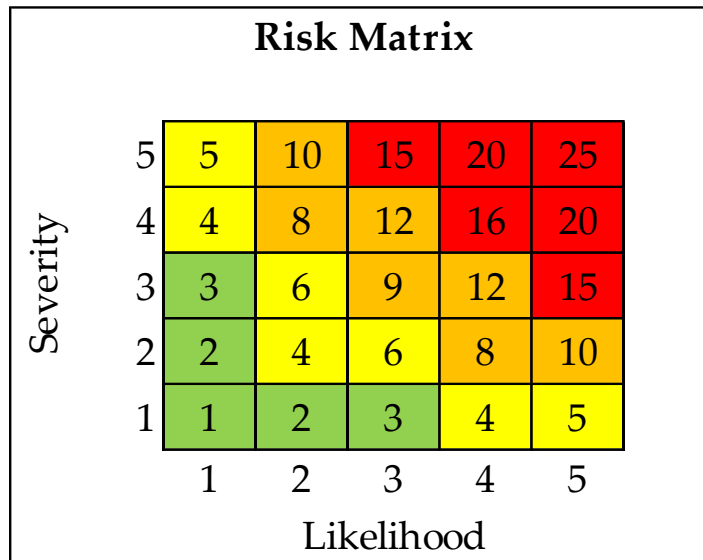


Figure 21: Risk matrix used to evaluate risks associated with the operation of the autoclave.

5.5.3 Risk Mitigation

Risk No.	Mitigation	Likelihood [1-5]	Severity [1-5]	New Classification
1.1	Do not wear loose clothing and tie hair	1	4	4
2.1	Always make sure parts are secured.	1	3	3
3.1	Use bolts to secure stainless steel container and autoclave to the vibrating table	1	3	3
5.1	Always turn off the amplifier when handling the ultrasonic transducer	1	3	3
6.1	To prevent a burst scenario, the autoclave was fitted with a safety valve actuating at 97 bar	1	2	2
6.3	To prevent a burst scenario, the autoclave was fitted with a safety valve actuating at 97 bar	1	2	2
6.4	Always make sure parts are secured.	1	3	3
7.1	Ensure ventilation when relieving the carbon dioxide	1	5	5
7.2	Always make sure parts are secured.	1	3	3
7.3	Always make sure parts are secured.	1	3	3
7.4	Do not wear loose clothing and tie hair	1	4	4

Table 5: Risks that require mitigation and the corresponding mitigation.

The mitigations for most of the works are straight forward. When working with rotational equipment, loose clothing and hair are not acceptable. Other than this, the autoclave does not pose as a dangerous experiment. Burst scenarios due to pressure cannot happen since the conduction of a pressure test is necessary after every disassembly. If material defects occurred, the pressure test with water safely reveals them. In general, all works associated with the autoclave and the experiments should not be carried out alone. There are many heavy objects and a few lifting procedures involved that require at least two people.

5.6 Experiment I – Heavy Carbonation Baseline

The first experiment run on this autoclave was with a light Portland Class G slurry with only Bentonite as an additive to control the free water. Initially, the plan was for the experiment to be three weeks in duration, but the carbonation occurred significantly faster than anticipated.

5.6.1 The Slurry Composition and Analysis

This experiment delivers the baseline of a cement subject to heavy carbonation to ensure that the CT scanner, as well as the acoustic measurements, work with measuring cement carbonation. The only additive in this slurry was Bentonite added to control free water. The base of the slurry is a high-sulfate resistant Portland Class G cement. The calculated density was 11.5 ppg (1.38 s.g.). **Table 5** shows the basic data of this slurry, **Figure 22** the rheological data, and **Figure 23** shows the data from the sedimentation test.

Slurry Composition for 6000cc Slurry Volume		
Cement [g]	Water [g]	Bentonite (15%BWOC) [g]
2848.4	4577.9	427.3
Measured Density [ppg]		
11.5 (1.38 s.g.)		
Free Fluid [%]		
3.72		
API Fluid Loss [ml]		
290.3		

Table 5: Slurry data of the 11.5 ppg slurry.

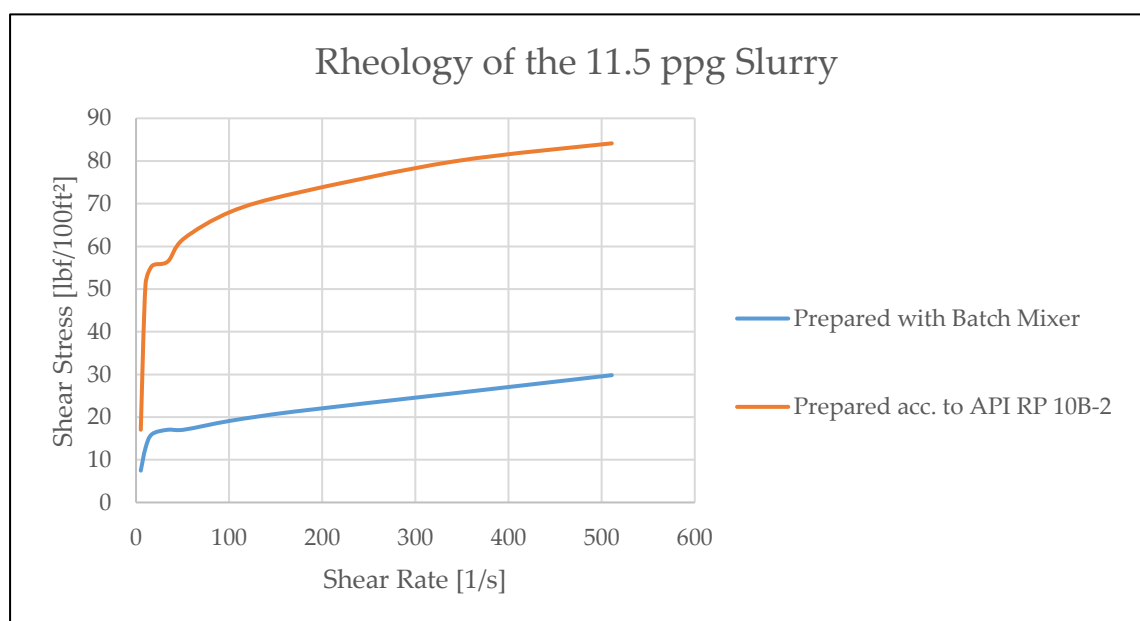


Figure 22: Rheological data of the 11.5 ppg slurry.

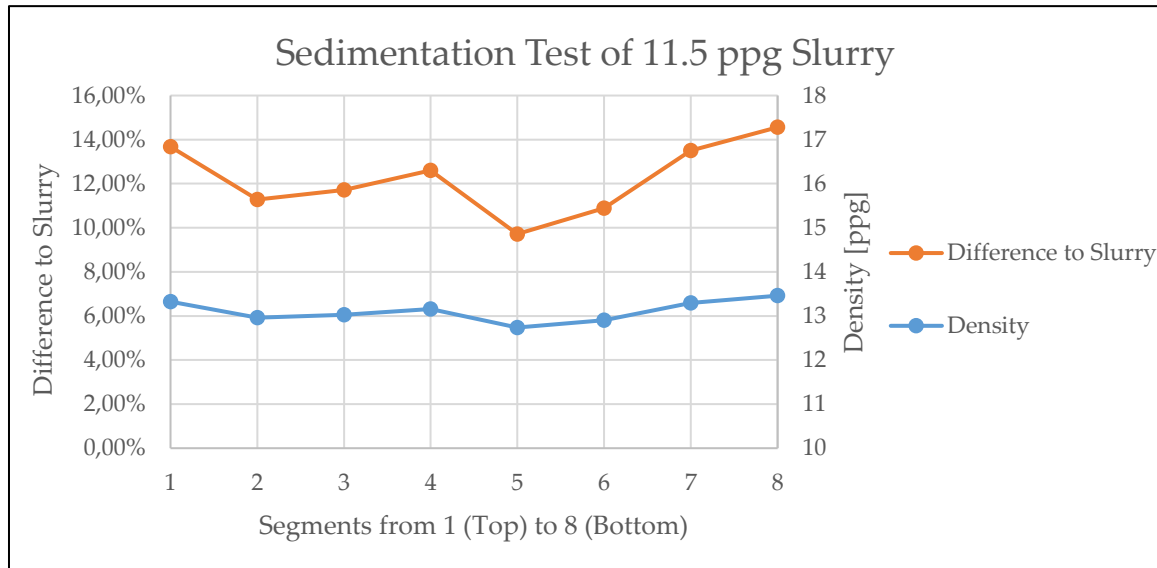


Figure 23: Sedimentation test of the 11.5 ppg slurry.

Mixing and conditioning of the slurry used for these tests and to fill the autoclave took place, as shown in the procedure. After adding the hydrated Bentonite into the stainless steel container, the batch mixer started agitating the liquid at low speed. Pouring the cement gradually into the stainless steel container ensures even distribution. After 10 minutes of mixing at high speed, conditioning of the slurry took place for 30 minutes on the vibrating table. Even though the preparation of the slurry with the batch mixer alters the rheology significantly compared to the API RP 10B-2 preparation, it was a desired side effect in this case. Before adding the Bentonite to the slurry, a one hour agitated hydration took place. Adding this prehydrated Bentonite to the slurry without any added water created a high viscous slurry when prepared according to API RP 10B-2, but an easy to handle, pourable slurry when mixed in the batch mixer. The added Bentonite proved to sufficiently control the free water; the same slurry without Bentonite emitted more than 20% free water, whereas, with Bentonite, it was only 3.72%. The sedimentation test showed that the slurry is stable and shows the typical profile with slightly higher densities at the top and the bottom. There is one inconsistency in the middle where the density drops by 0.42 ppg from segment 4 to segment 5. There were no visible defects at this point.

5.6.2 Preparing and Pressurizing the Autoclave

Succeeding the slurry preparation, pouring the slurry around the sandstone core held by the core-centralizers, ensures the creation of an evenly cemented annulus, after filling the annulus with cement slurry, the cement sets for 24 hours. After two hours, the extraction of the free fluid took place to eliminate additional variables created by the water in the autoclave. After a minimum of 24 hours, the slurry achieved the desired degree of curing, closing the autoclave results from fixating the top flange, according to the procedure. **Figure 25** shows the circuit used to create a vacuum within the autoclave and the circuit itself. This vacuum also includes the pressure regulator of the carbon dioxide cylinder. After lining up the circuit, turning on the vacuum pump creates the desired vacuum, in this case, 140 mbar. The heating remained off; thus, the temperature

corresponds to the ambient temperature of roughly 24 °C. **Figure 24** illustrates the temperature and pressure development during vacuum creation. After creating the vacuum, the flow circuit changed to facilitate the carbon dioxide injection.

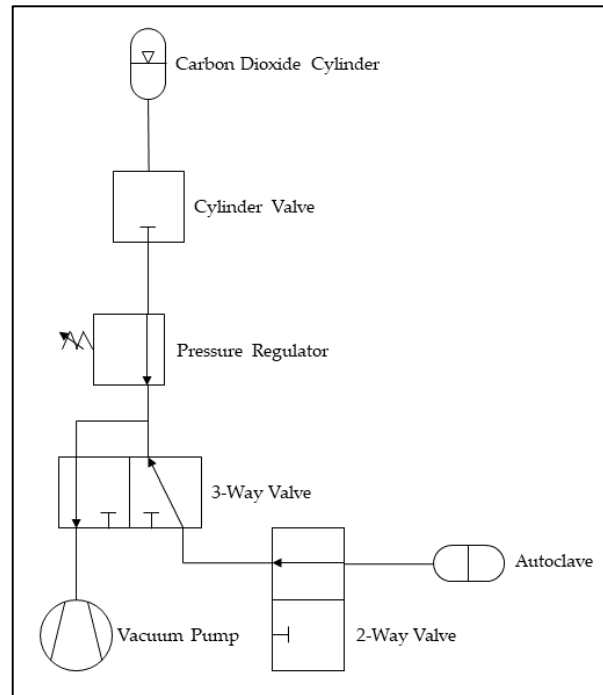


Figure 25: Schematic of the flow circuit used to create the vacuum.

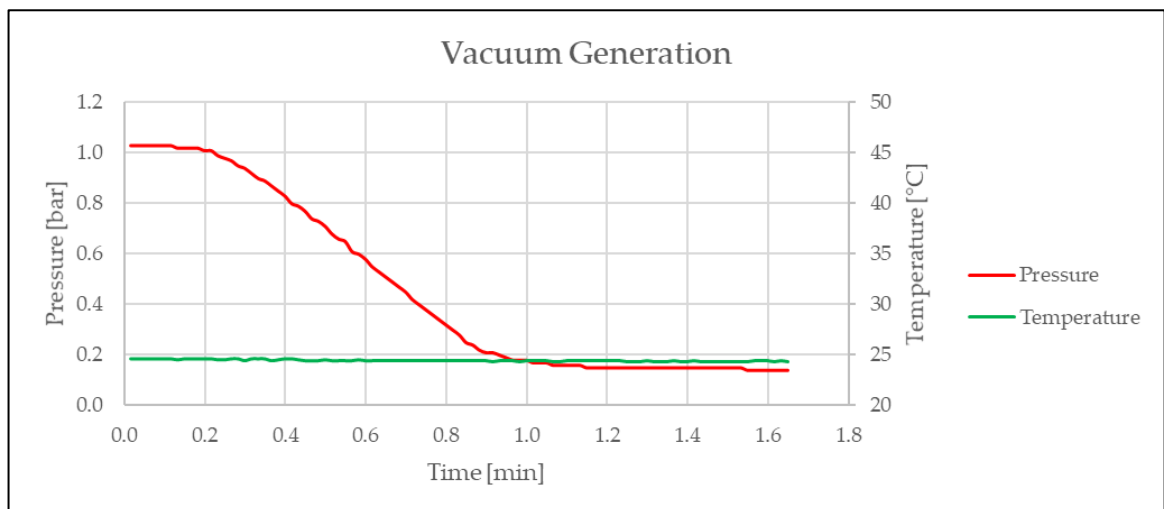


Figure 24: Pressure and temperature development during vacuum creation.

In the next step, carbon dioxide from the cylinder fills the autoclave. The pressure of the cylinder is 50 bar, and the starting pressure for this experiment is, subsequently, also 50 bar. The aim here was to gradually increase the pressure over a few minutes, so as not to disrupt the cement and its bonds. **Figure 26** illustrates the circuit used to pressurize the autoclave with carbon dioxide. It is the same circuit as in the vacuum creation phase with the difference that the three-way-valve cuts the vacuum pump from the circuit. **Figure 27** shows the pressure and temperature development during the injection. The pressure rises from 0.14 bar in the beginning, to 49.98 bar in the end. During the injection,

Experiments

the volumetric work of carbon dioxide leads to a temperature increase from 24 °C to 34 °C. After reaching the desired pressure of roughly 50 bar, closing the two-way valve on the autoclave creates a gas-tight system. After the closing, the removal of the flow circuit from the autoclave is possible. Immediately after reaching the maximum pressure, turning on the heating creates supercritical conditions within the cell. In theory, the cell mimics an isochoric process filled solely with carbon dioxide, which in turn should behave like an ideal gas. In such a process, the pressure and temperature changes occur according to Eq 5-1 (Gedde 2020).

$$\frac{p_2}{p_1} = \frac{T_2}{T_1} \quad \text{Eq 5-1}$$

Taking the starting temperature of 34 °C together with the desired final pressure of 80 bar leads to a necessary temperature increase of 20.4 °C. To account for discrepancies

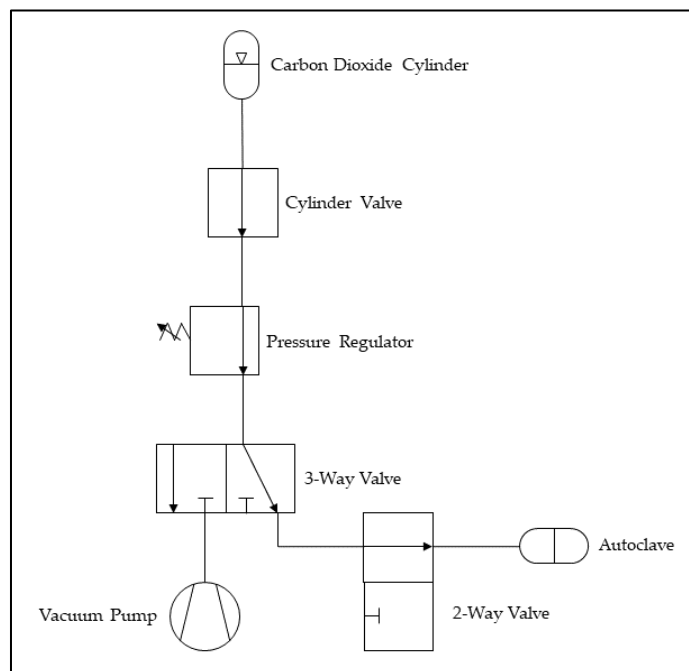


Figure 26: Schematic of the circuit used to inject the carbon dioxide into the autoclave.

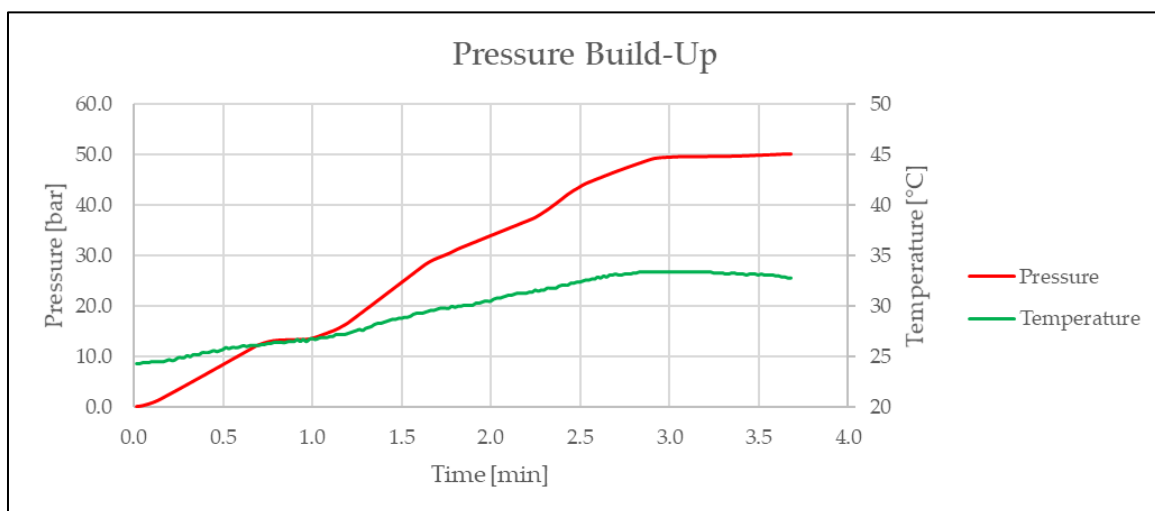


Figure 27: Pressure and temperature development during carbon dioxide injection.

and impurities of the carbon dioxide, the heating jacket heated the autoclave to 50 °C at first, while monitoring the pressure closely.

5.6.3 Monitoring the Carbonation

Monitoring the closed autoclave took place for 162 hours. **Figure 28** illustrates the pressure and temperature development inside the autoclave over this period. Immediately after disconnecting the carbon dioxide cylinder, the pressure started decaying. There was no point in heating-up the autoclave to a higher temperature since the gas expansion would not deliver the desired supercritical conditions. The carbonation monitoring took place continuously throughout the experiment. This monitoring occurred through several CT-scans and acoustic measurements at the start and end of the experiment.

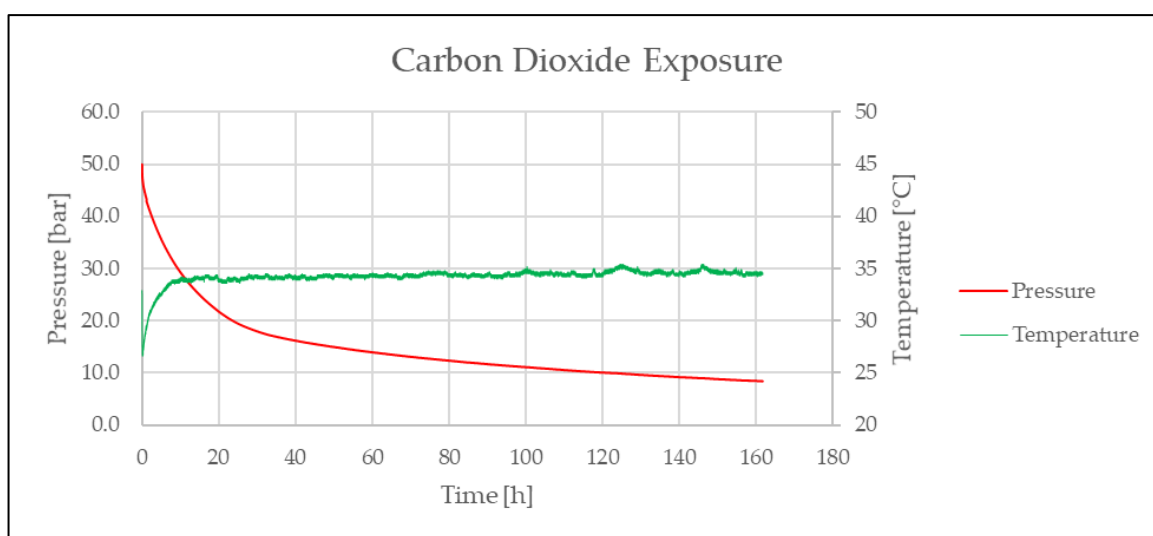


Figure 28: Pressure and temperature development during the experiment.

5.6.3.1 Acoustic Measurements

As described earlier, piezo elements attached to the autoclave are one way of monitoring the carbonation continuously. Attaching three piezo elements, one acting as a transducer and two acting as receivers enables this analysis. One receiver, attached vis-a-vís from the transmitter, delivers a transit time of the signal across the entire autoclave. The other receiver, attached roughly five cm below the transmitter, functions as a pulse-echo type set-up. **Figure 29** shows an image of the array of acoustic sensors. The sensor with the green cable is the transmitter. Baseline tests delivered the necessary data to understand the acoustic readings taken from the autoclave.

Additionally, comparing the data from the ultrasonic compressive strength test, according to API RP 10B-2 with the data from the sensors on the autoclave, enables conclusions on the condition of the cement inside. **Figure 30** shows the development of the compressive strength of the 11.5 ppg slurry inside the autoclave, tested according to API RP 10B-2. The sample stems from the same slurry batch as the cement in the autoclave, and testing took place over 188 hours. The data from the ultrasonic compressive strength test gives a baseline. Using this baseline as a reference for two

Experiments

distinct acoustic readings enables an analysis of the cement inside. These two readings are from before the carbon dioxide injection, and at the end of the carbon dioxide exposure. The compressive strength from the API RP 10B-2 test gives a value of 156 psi after 24 hours and 212 psi after 162 hours.

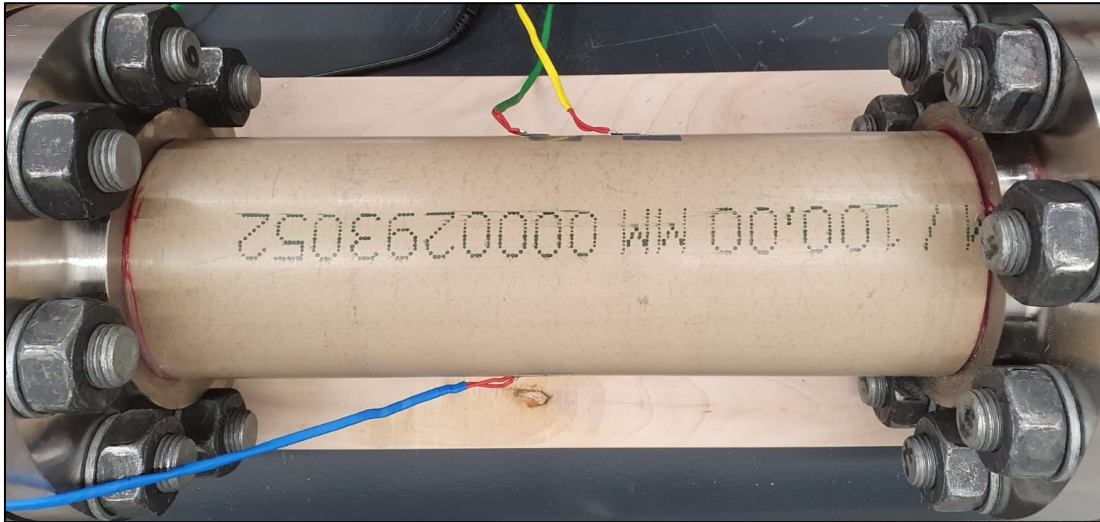


Figure 29: Photograph of the PEEK pipe-body with attached flanges and acoustic sensors.

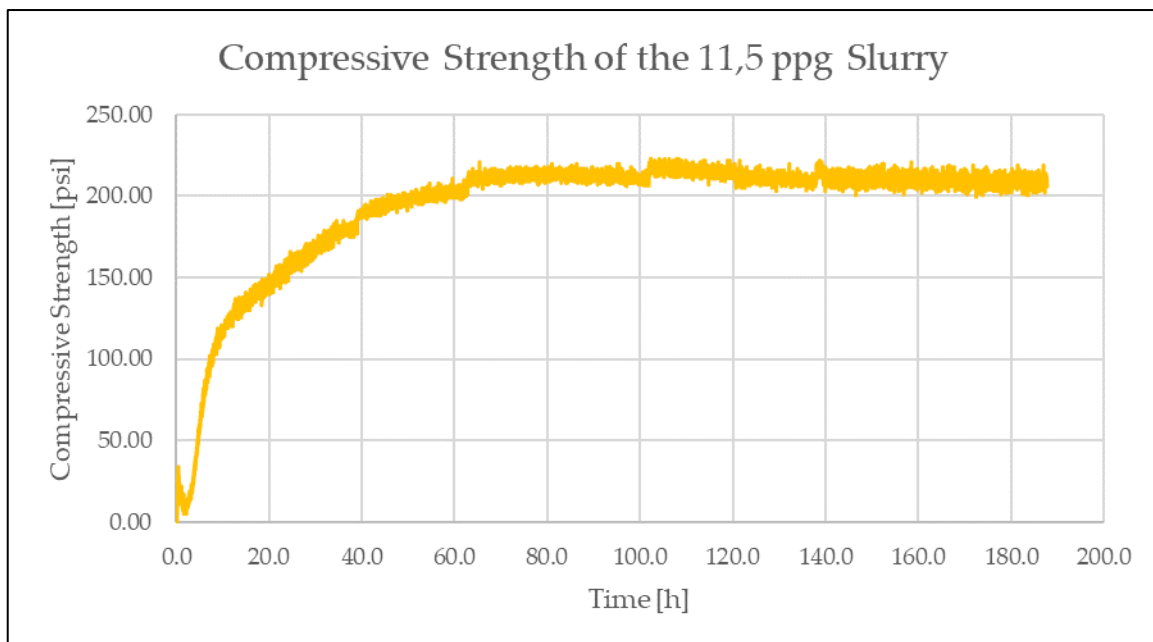


Figure 30: Compressive strength development of the 11.5 ppg slurry tested according to API RP 10B-2.

During this first experiment, it became clear that the pulse-echo type set-up of the acoustic elements delivers more usable results for cement evaluation. In order to properly evaluate the data from the acoustic measurements, knowing the precise distances the signal travels is necessary. **Figure 32** shows a drawing of the distances the signal travels.

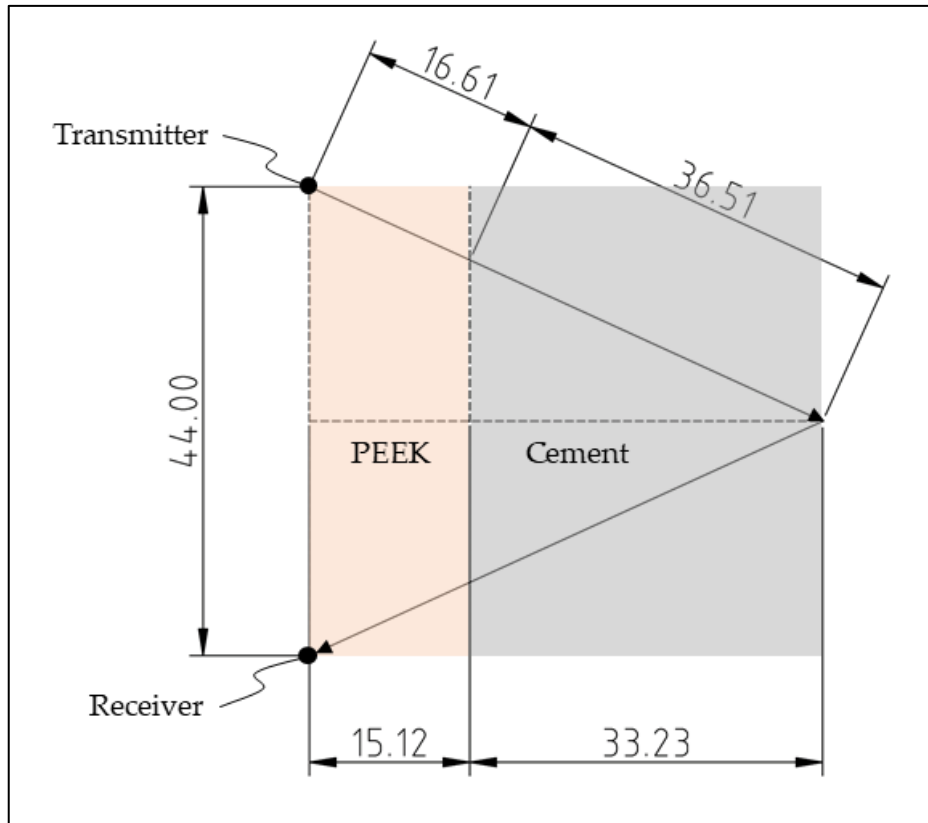


Figure 32: Distance traveled by the acoustic signal through the 11.5 ppg cement in the pulse-echo set-up.

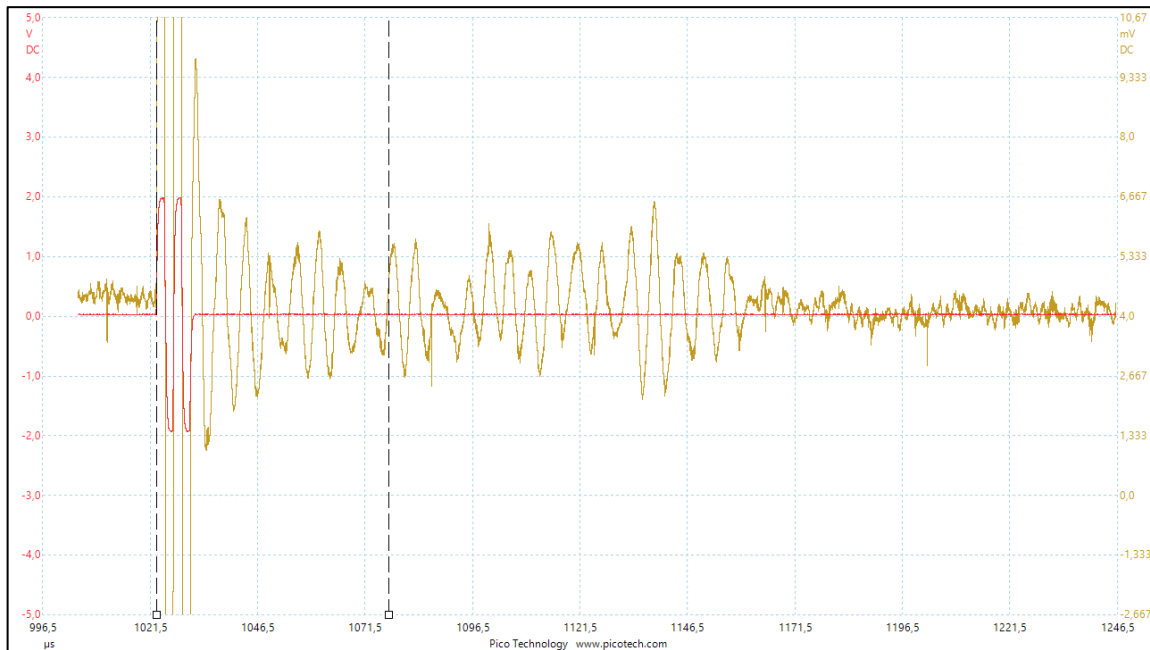


Figure 31: Excerpt from the oscilloscope readings of the pulse-echo receiver before the carbon dioxide injection.

The total distance from the transmitter to the receiver, reflected at the cement-sandstone interface, is 106.24 mm. These values come from digital measurements of the CT-scans. The signal used is a two-cycle square wave with a frequency of 250 kHz. For this

Experiments

frequency and the temperature of the autoclave, the sonic velocity of PEEK is roughly 2700 m/s. From the total distance, 33.22 mm account for the distance through the PEEK, meaning that 12.3 μs of the total transit time are from the transit through the PEEK pipe-body. **Figure 31** shows an excerpt from the oscilloscope readings of the receiver of the pulse-echo set-up. The dashed lines mark the beginning of the transmitted signal and the arrival of the mentioned echo. The measured time between the dashed lines is 54 μs . Subtracting the known transit time through the PEEK pipe-body and using the cement distance 73.02 mm, the acoustic travel time of the cement in the autoclave after 24 hours comes to 1751.2 m/s. This value corresponds to a compressive strength of 174 psi.

Applying the same procedure to the acoustic data after 162 hours results in a travel time of 1772.5 m/s corresponding to a compressive strength of 194 psi compared to 212 psi as reported by the compressive strength test according to API RP 10B-2. **Figure 33** shows the acquisition of the total transit time after 162 hours of carbon dioxide exposure.

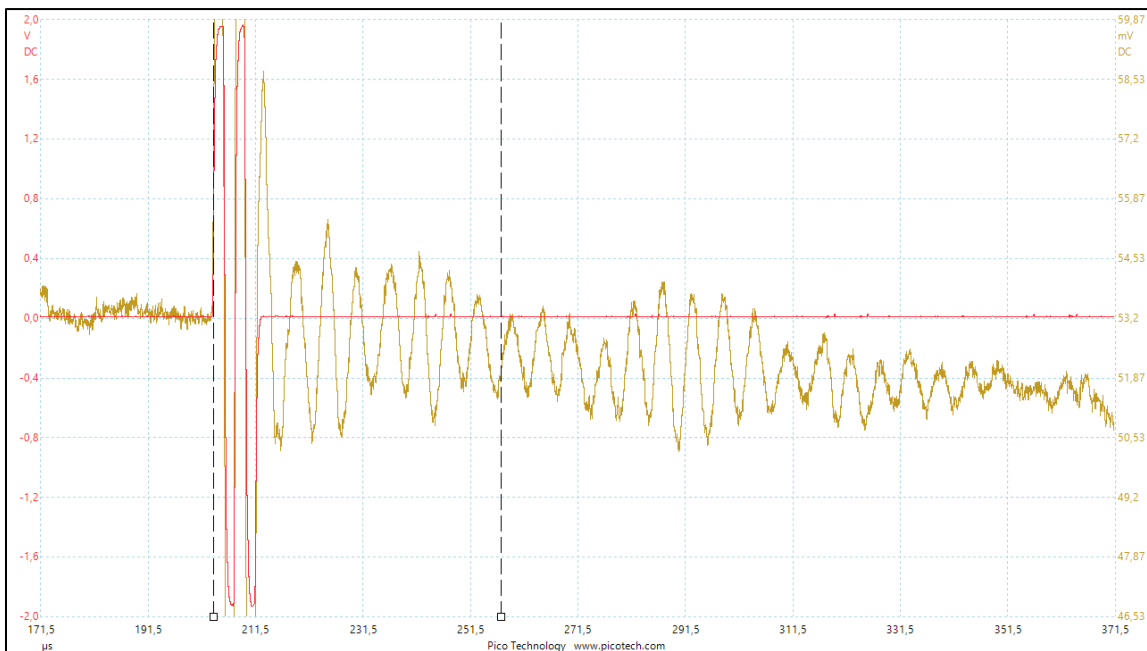


Figure 33: Excerpt from the oscilloscope readings of the pulse-echo receiver after 162 hours of carbon dioxide exposure.

5.6.3.2 CT-Scan Analysis

Accompanying the acoustic analysis is a sequence of CT-scans conducted throughout the experiment. The PEEK pipe-body of the autoclave enables the CT-scans as compared to conventional autoclaves made from steel. For this first experiment, ten scans build the basis for the analysis. **Figure 35** shows a photograph of the autoclave inside the CT-scanner. Marking the position on the CT-scanner table ensures the same placement of the autoclave every time, which in turn alleviates image processing.



Figure 35: Photograph of the autoclave inside the CT-scanner.

The first scan took place before the carbon dioxide injection to establish a reference. **Figure 34** shows a cross-sectional view of this first scan. The cement is distinguishable from the sandstone, PEEK, steel, and voids. Due to the low viscosity of the 11.5 ppg slurry and the hydrostatic pressure of the annular slurry column, a cement displacement back into the sandstone channel occurred. This displacement limited the study to the first ten centimeters, where carbon dioxide diffuses through the sandstone into the cement.

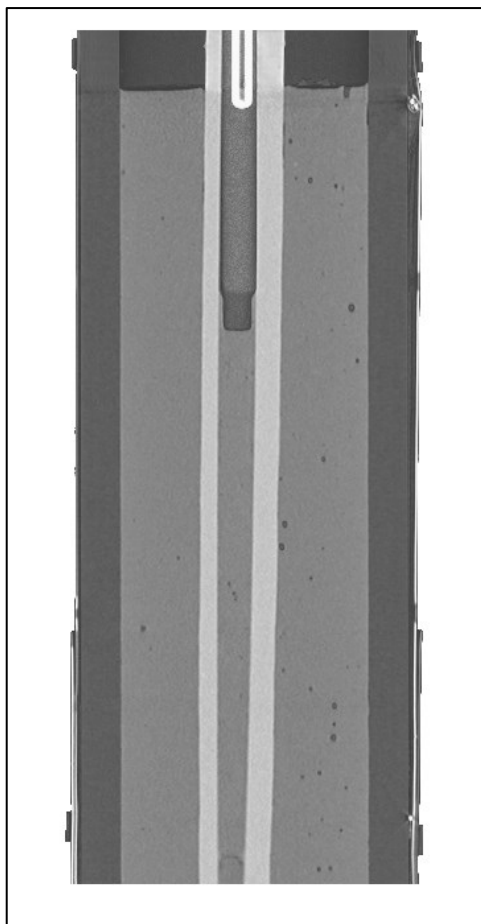


Figure 34: Cross-sectional view of the first CT-scan.

Experiments

The second scan took place after the carbon dioxide injection. Even though the cement acquired 174 psi in compressive strength over the 24 hour curing period, the injected pressure led to fractures throughout the cement. **Figure 36** shows this crack. Due to this crack, the experiment went differently than anticipated. Three cracks formed, but one of them resulted in a void of circa one millimeter. Because of this, the diffusion did not occur through the sandstone, and the carbon dioxide diffused mostly through the crack directly into the cement.

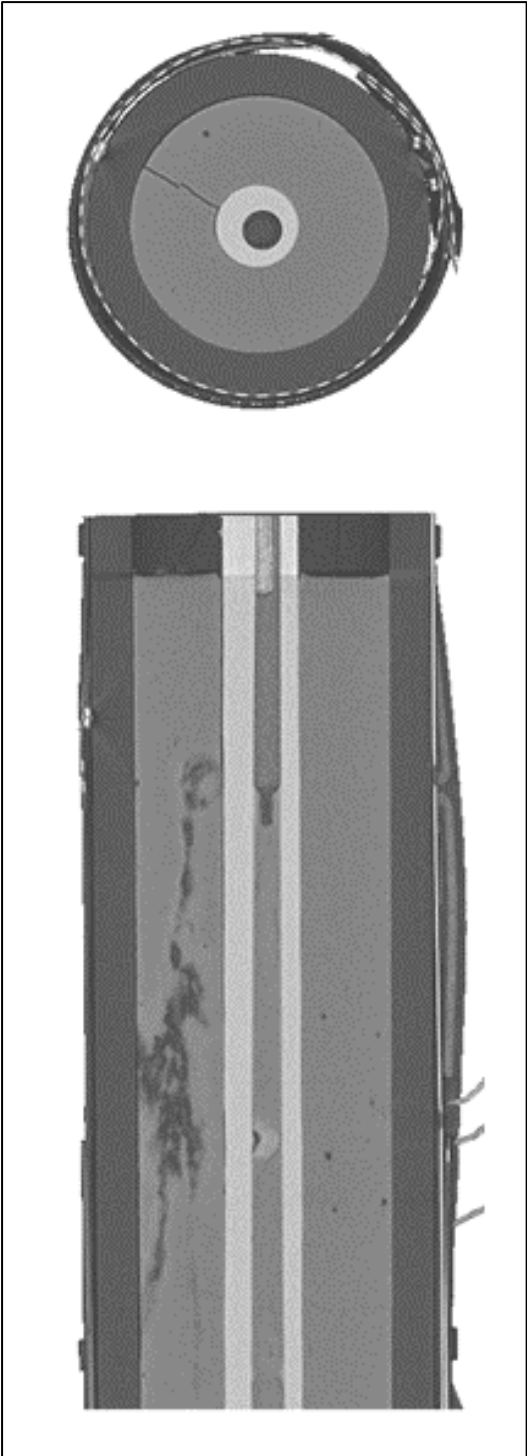


Figure 36: Top- and side-cross-sectional view exposing the crack formed during carbon dioxide injection.

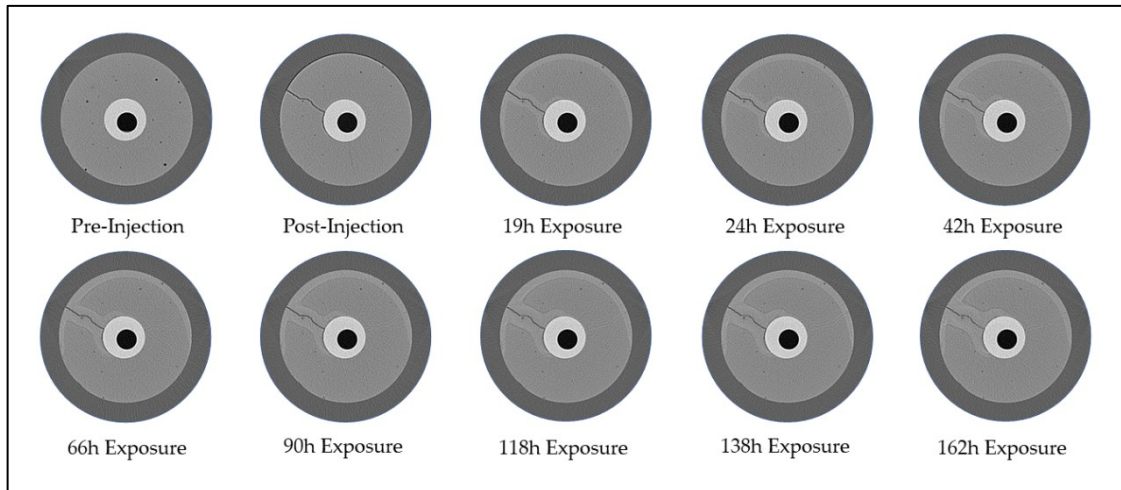


Figure 37: Carbonation progression of the 11.5 ppg cement visualized with single slices of the corresponding CT-scans.

The carbonation progressed evenly along debonded interfaces and cracks. **Figure 37** shows a comparison of the same slice of the CT-scans at various exposure times. This 11.5 ppg cement carbonated heavily. After 19 hours of carbon dioxide exposure, the carbonation front has already progressed by up to 4.5 mm. Towards the end of the carbon dioxide exposure duration, the carbonation along the debonded interfaces seemed to halt, whereas the carbonation along the major crack kept progressing. **Figure 38** depicts a graph showing the progression of the carbonation at a debonded interface and the major crack. The measurements stem from digital analysis of the CT-scans.

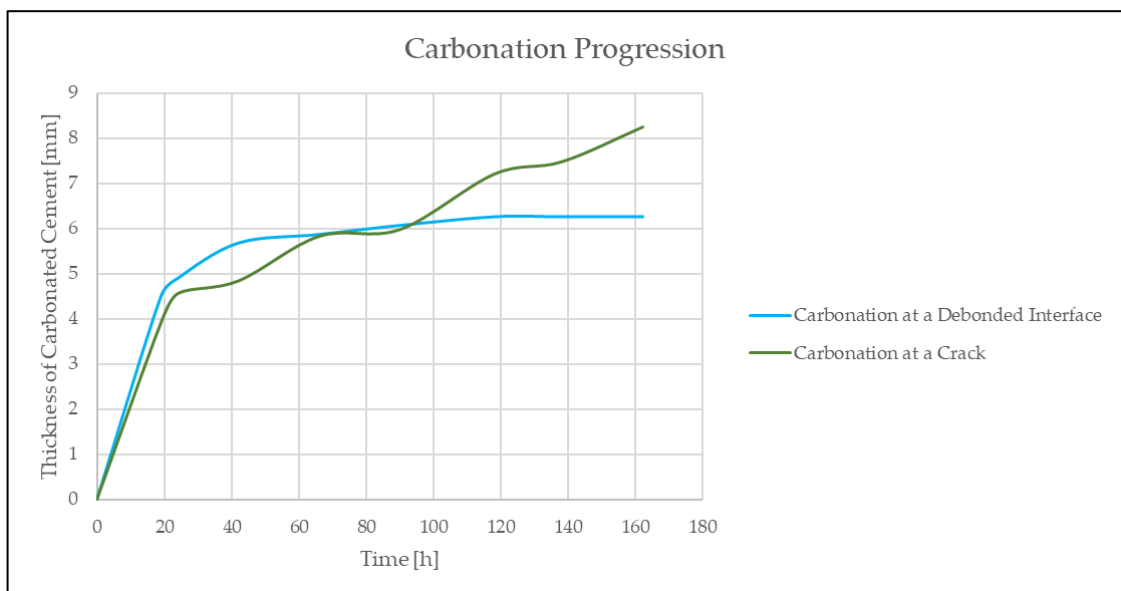


Figure 38: Graphical depiction of the carbonation progression at different locations in the cement sample.

5.6.4 Termination of the Experiment

After 162 hours, the experiment concluded. Bleeding off the remaining pressure of roughly 8.5 bar occurred by gradually opening the two-way valve on the autoclave. **Figure 39** depicts the progression of pressure and temperature during this phase.

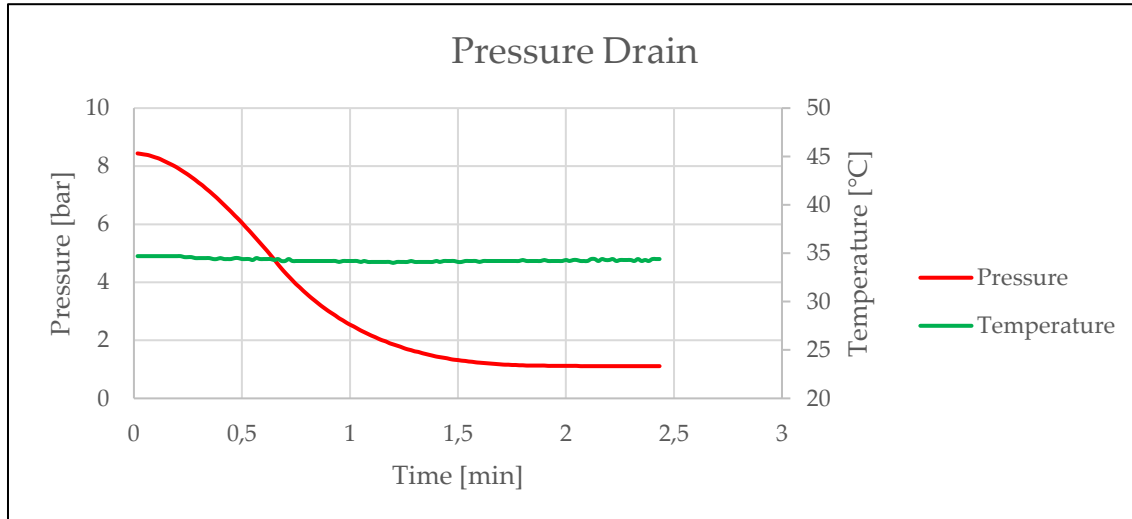


Figure 39: Pressure and temperature progression during the bleeding off of the pressure.

Once the internal pressure reached the atmospheric level of one bar, opening the autoclave became possible. The extraction of the sandstone/cement sample inside occurred after the removal of the top and bottom flange. After the opening of the top flange, water was visible on top of the cement. The measurement produced an amount of 40 ml. Due to the cracks within the cement and the significant debonding along the sandstone interface, the sample broke into multiple pieces. Due to the sample breaking, the manufacturing of one-inch diameter and two-inch lengths cylinders was more difficult than anticipated. The preparation of these samples was necessary for further analysis. **Figure 40** shows a photograph of the sample right after the extraction from the autoclave.



Figure 40: Photograph of the cement and sandstone after extracting it from the autoclave.

The cement looked water-saturated almost entirely, with one exception along one of the fractures. This exception is clearly visible in the photograph where there is light grey shading compared to the darker grey of the water-saturated cement. In the photograph, the top is on the left and the bottom on the right. This distinction is essential since exposure of the top surface to carbon dioxide occurred. When looking closely on the CT-scans, a second front is visible within the carbonation. The brown areas in the photograph appear to be this second front. **Figure 41** shows a photograph of a cut and dried piece from one of the segments of the 11.5 ppg cement sample. The outer, brownish front crumbles to dust when touched. Also, the carbonated cement is only loosely consolidated. The interface between the carbonated cement and the uninvaded cement has no bond.



Figure 41: Cut and dried piece from one of the segments of the 11.5 ppg cement after carbon dioxide exposure.

5.6.5 Experiment I – Conclusion

As anticipated before conducting the experiment, the 11.5 ppg slurry delivered the heavy-carbonation baseline desired. The degree of carbonation and the speed with which it occurred surprised. The plan was for the experiment to take up to three weeks and keep supercritical conditions throughout. Due to the reaction occurring more or less immediately after carbon dioxide injection, the pressure within the autoclave never reached supercritical conditions. The expected pressure increase from the gas expansion due to temperature increase never occurred. On the contrary, due to the massive reaction, the pressure started declining as soon as removing the carbon dioxide cylinder. Since the entire set-up passed the pressure test, this pressure decay does not come from a leakage.

Unfortunately, acoustic measurements were not possible while the autoclave was in the CT-scanner, because the CT-scanner created interference in the acoustic signal. This interference is the cause, why only two readings occurred, one at the start and one at the end. The decision made was that the autoclave remains inside the CT-scanner in the

Experiments

exact position over the entire duration to enable easier image processing. The priority was to prove the suitability of the CT-scanner to detect the carbonation. As the images show, this suitability is proven, and the same goes for the autoclave. The autoclave holds the pressure and enables measurements of all types due to the construction of the pipe-body from PEEK.

The two acoustic measurements taken, delivered suitable results. The measurement of the cement before carbon dioxide injection delivered a result very close to the compressive strength test, according to API RP 10B-2. The result from the second measurement taken after 162 hours of exposure, delivered a significantly lower compressive strength. This lower compressive strength entails that the carbonation caused an ample decay of integrity in the cement.

Another important fact to mention is the fracturing of the cement when injecting the carbon dioxide. In terms of well integrity, this cement sheath lost its integrity as soon as confronted with pressure. The created fractures went continuously throughout the cement, creating flow paths for all media.

5.7 Experiment II – Light Carbonation Baseline

The second experiment run on this autoclave aims to establish a baseline for cement that only shows light to no carbonation. The choice fell to a heavy neat class G slurry without additives.

5.7.1 The Slurry Composition and Analysis

The slurry for this second experiment utilizes the same cement as with the first experiment, a high-sulfate resistant Portland Class G cement. Compared to the first slurry, there are no additives in this slurry; it only consists of cement and water. A calculated density of 17 ppg delivered a slurry with a measured density of 16.8 ppg. This difference stems from pouring the cement too quickly into the batch mixer, causing the formation of clumps. This heavy slurry has a water-cement ratio of 0.346 as compared to 1.61 of the first slurry. **Table 6** shows the basic data of this slurry, **Figure 42** shows the rheological data, and **Figure 43** shows the data from the sedimentation test.

Slurry Composition for 6000cc Slurry Volume	
Cement [g]	Water [g]
9096.4	3148.4
Measured Density [ppg]	
16.8 (2.02 s.g.)	
Free Fluid [%]	
2.2	
API Fluid Loss [ml]	
47.1	

Table 6: Slurry data of the 17 ppg slurry.

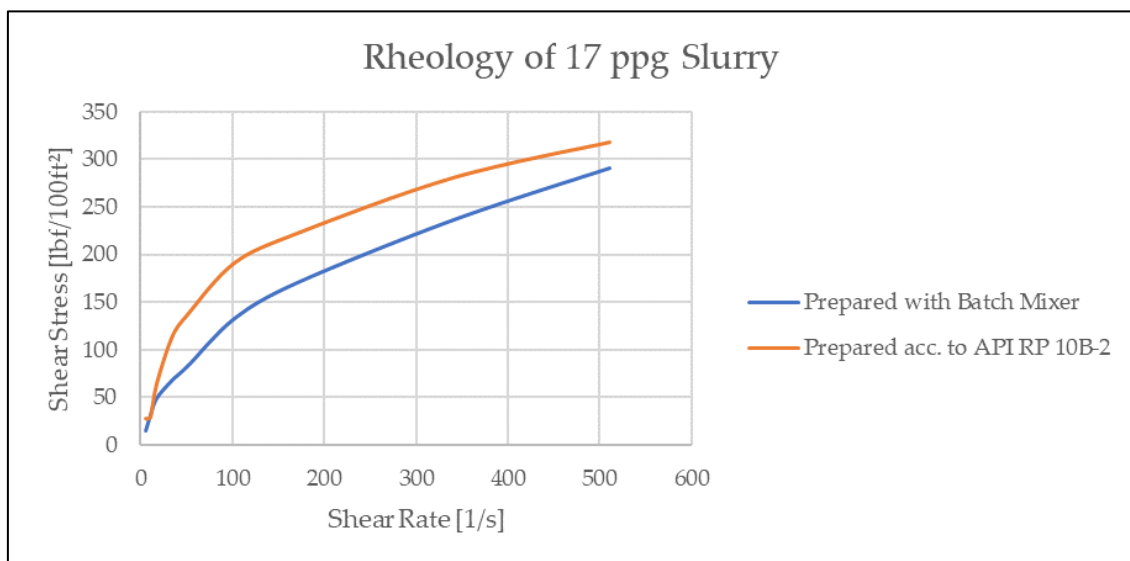


Figure 42: Rheological data of the 17 ppg slurry.

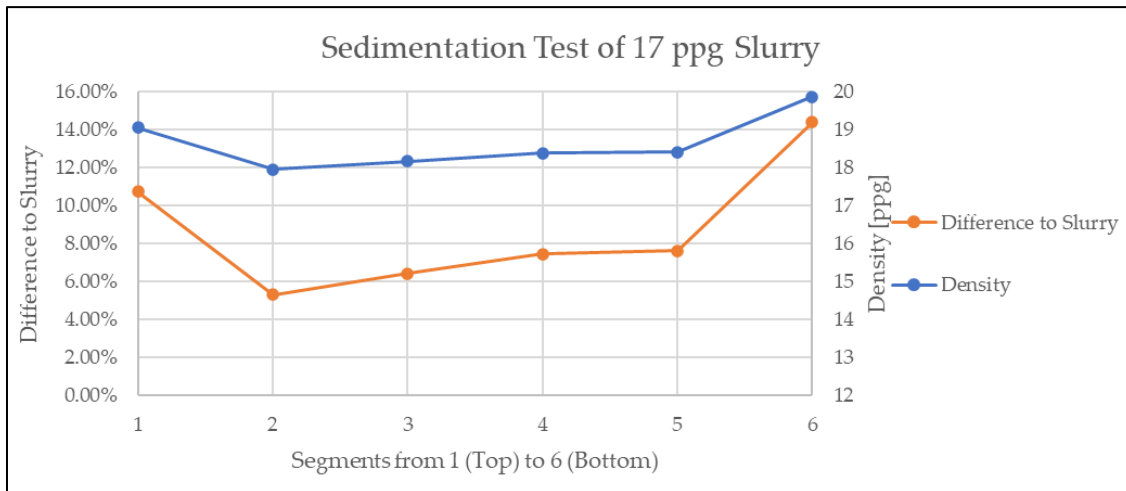


Figure 43: Data from the sedimentation test of the 17 ppg slurry.

The mixing and conditioning of the 17 ppg slurry, as with the 11.5 ppg slurry, occurred according to the procedure. Setting the batch mixer with the water in the stainless steel container to low speed while adding the cement ensured even distribution. The density difference in calculated and measured slurry density demonstrated that adding the cement even slower is necessary. As with the 11.5 ppg slurry, mixing the 17 ppg slurry for 10 minutes at high speed followed by 30 minutes of conditioning on the vibrating table created the desired properties. Due to the significantly lower water-cement ratio, the slurry required no free-fluid control additive. The low free fluid amount of 2.2 % proved this. The added Bentonite in the first slurry causes a significant difference in the rheology when comparing the data from the slurry mixed according to API RP 10B-2 and the batch mixer. This difference was considerably lower with the second slurry. The sedimentation test delivered data similar to the first slurry but showed higher stability. Except for the top and bottom segment of the sedimentation test, the 17 ppg slurry showed minimal deviation.

5.7.2 Preparing and Pressurizing the Autoclave

After preparing the slurry, filling the autoclave happened as with the 11.5 ppg slurry. A core-centralizer held the sandstone core in place, and pouring the slurry occurred in a circular fashion around the sandstone. The slurry was considerably more viscous than the 11.5 ppg slurry, which made the displacement into the autoclave more difficult. After displacing the slurry into the autoclave, the slurry set for 24 hours. Also, with the 17 ppg slurry, extraction of the free fluid occurred after two hours of curing. The pressurization procedure began after the curing period. The same flow circuits, as pictured in **Figure 25** and **Figure 26**, enabled the vacuum creation and subsequent pressurization. **Figure 44** illustrates the pressure and temperature development of the autoclave with the 17 ppg slurry during the vacuum generation. The process was the same as with the 11.5 ppg slurry. The maximum vacuum reached was 150 mbar. The heating remained off; thus, the temperature corresponds to the ambient temperature of roughly 24 °C. Once reaching 150 mbar, keeping the vacuum pump turned on did not deliver a lower pressure. Even after 10 minutes of running the vacuum pump, the pressure did not decline further. The graph does not include these additional eight minutes.

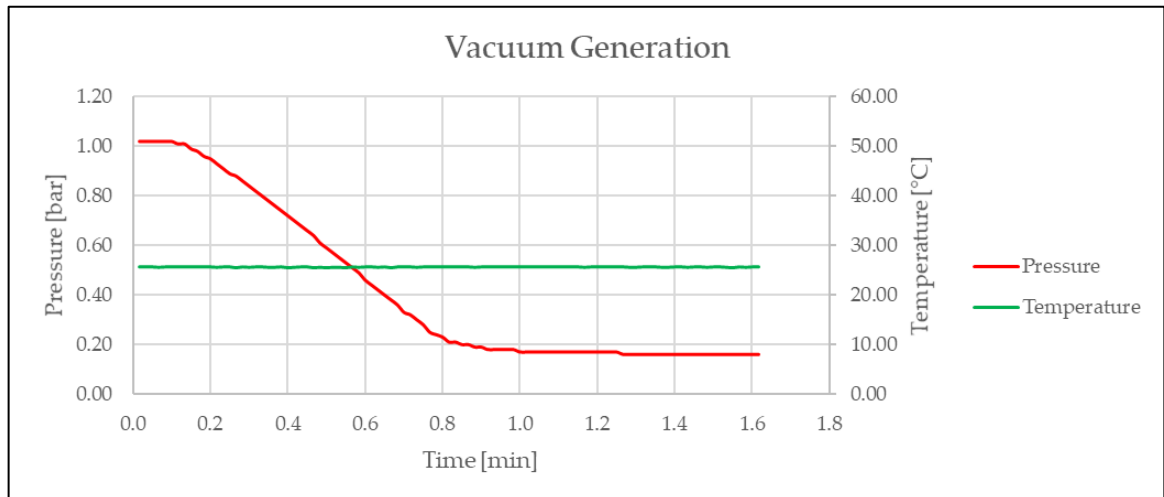


Figure 44: Pressure and temperature development during vacuum generation.

After the vacuum creation, altering the flow circuit enabled the pressurization of the autoclave. This pressurization resulted from aligning the carbon dioxide gas cylinder. The pressure of the gas cylinder was slightly higher than before at 50.98 bar, and the maximum pressure came subsequently to 50.98 bar. The attempt was to create a pressure of 80 bar by heating the gas and raising the pressure through gas expansion. Also, with the 17 ppg cement, the pressure started declining immediately after disconnecting the carbon dioxide cylinder. **Figure 45** illustrates the pressure and temperature development during the pressurization. The volumetric work of the carbon dioxide caused a temperature increase of 27 °C. A gradual increase in the output pressure from the carbon dioxide cylinder ensured that no fractures occur within the cement. Immediately after disconnecting the autoclave from the flow circuit, turning on the heating jacket to 50 °C, as with the 11.5 ppg cement, should deliver the desired 80 bar. The pressure-temperature relation is the same as with the first experiment and behaves according to Eq 5-1 if the carbon dioxide inside behaves like an ideal gas.

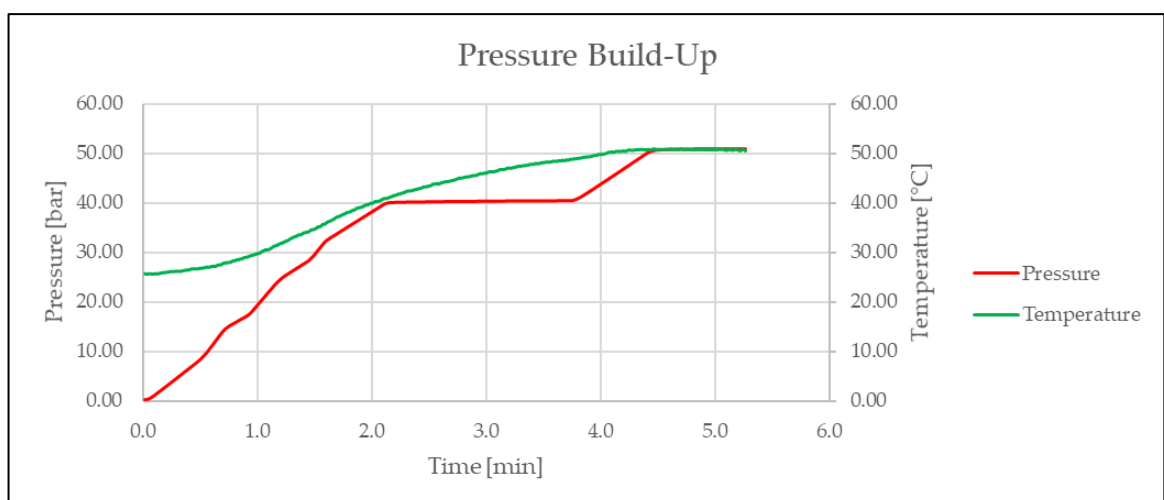


Figure 45: Pressure and temperature development during the pressurization of the autoclave.

5.7.3 Monitoring the Carbonation

Monitoring the carbonation inside the closed autoclave took place for 168 hours. **Figure 46** illustrates the pressure and temperature development throughout the experiment. As mentioned earlier, the pressure started declining immediately after disconnecting the carbon dioxide cylinder. The heating held 50 °C on the outside of the cell, and the inside stayed stable at roughly 40 °C. As with the first experiment, the execution of acoustic measurements occurred at the start and end of this experiment. One CT-scan builds the baseline, taken before the carbon dioxide injection, from there on, CT-scanning continued in a 24-hour interval.

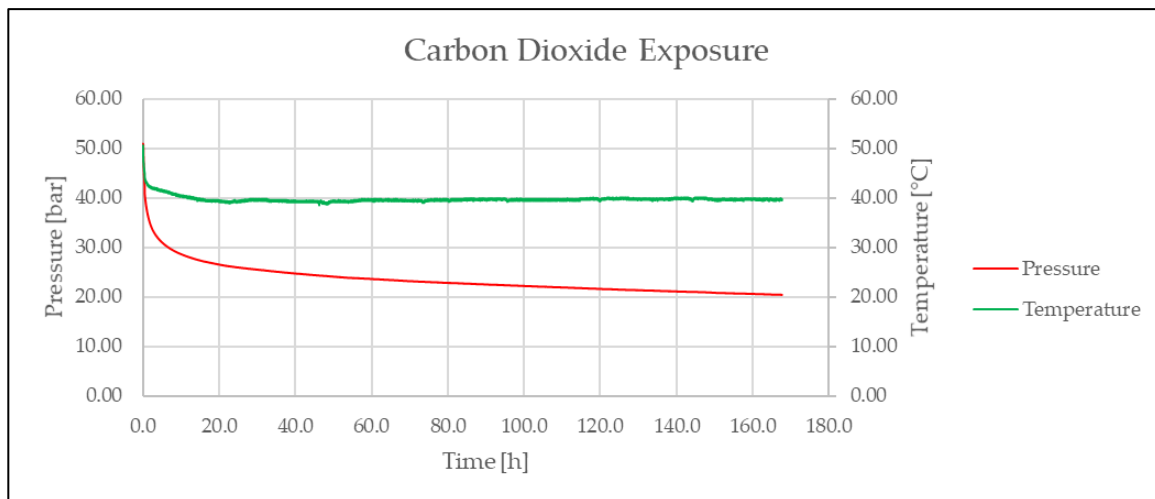


Figure 46: Pressure and temperature development during the experiment.

5.7.3.1 Acoustic Measurements

The basis of this analysis is again the collected baseline data as well as the ultrasonic compressive strength test according to API RP 10B-2. **Figure 47** shows a graphical depiction of the data from the ultrasonic compressive strength test of the 17 ppg slurry, according to API RP 10B-2. The test ran for 194 hours, and matching the data helps understand the influence of the carbonation on the cement inside the autoclave. The conditions of the ultrasonic compressive strength test mimicked the conditions present within the autoclave to ensure the best comparability. For this analysis to deliver reliable results, the exact distance traveled by the acoustic signal is necessary. **Figure 48** shows this distance. The values in this figure stem from digital measurements taken in the CT-scans. As with the acoustic analysis of the cement in the first experiment, a sonic velocity value is necessary for the PEEK pipe-body. Using the same value as before, 2700 m/s, delivers comparable results. The set-up comprised of one transmitter and two receivers. Attaching one receiver vis-a-vis from the transmitter and one receiver in line with the transmitter facilitates a thorough analysis.

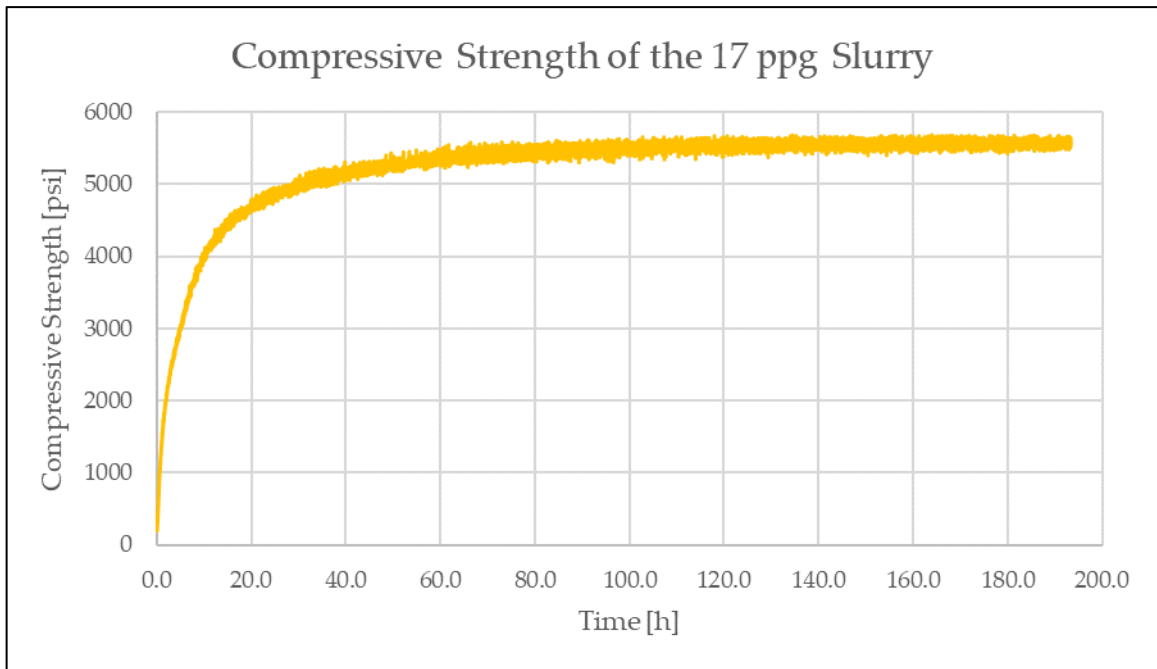


Figure 47: Compressive strength development of the 17 ppg slurry tested according to API RP 10B-2.

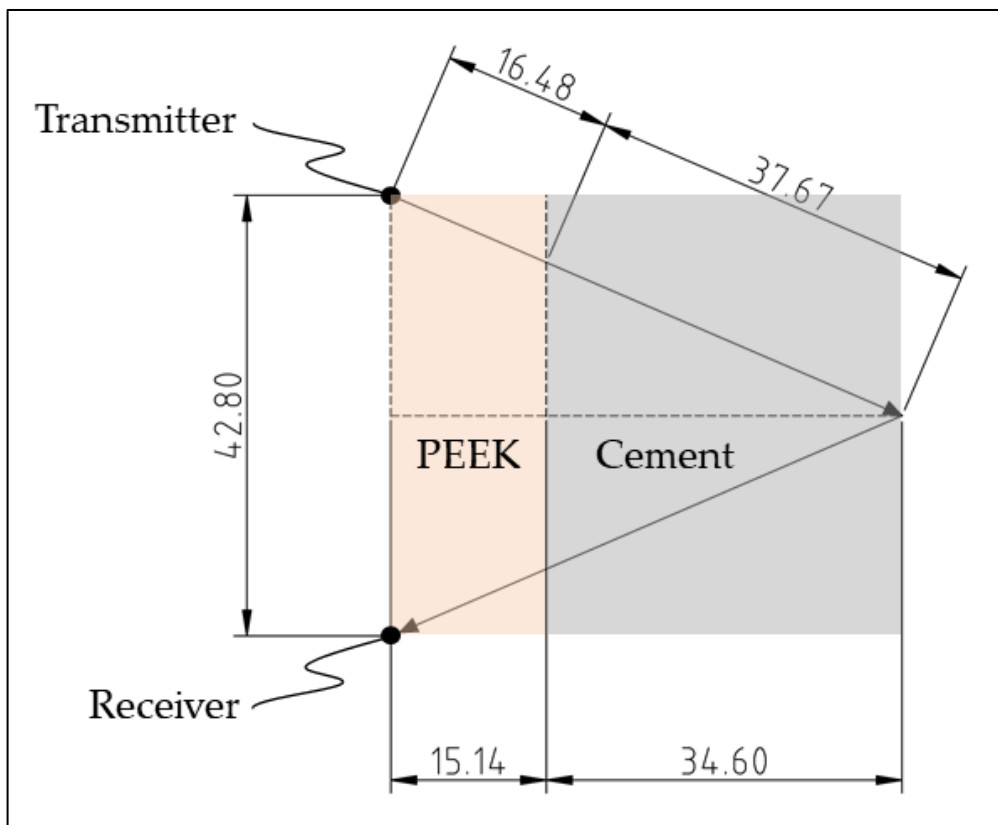


Figure 48: Distance traveled by the acoustic signal through the 17 ppg cement in the pulse-echo set-up.

Experiments

The first data comparison is after 24 hours. This reading comes from the cement before the carbon dioxide injection. For this reading, the deduced compressive strength is supposed to be similar to the compressive strength determined by the test conducted according to API RP 10B-2. After 24 hours, the compressive strength, according to API RP 10B-2, comes to 4760 psi. **Figure 49** shows the acoustic signal collected after 24 hours of curing. The red curve depicts the signal sent to the transducer at a twentieth scale. The yellow curve depicts the signal from the pulse-echo type receiver. The dashed line marks the arrival time of the signal reflected from the cement sandstone interface. Taking this travel time and subtracting the travel time through the PEEK pipe-body gives a sonic velocity of 3244.3 m/s leading to a compressive strength of 4004 psi.

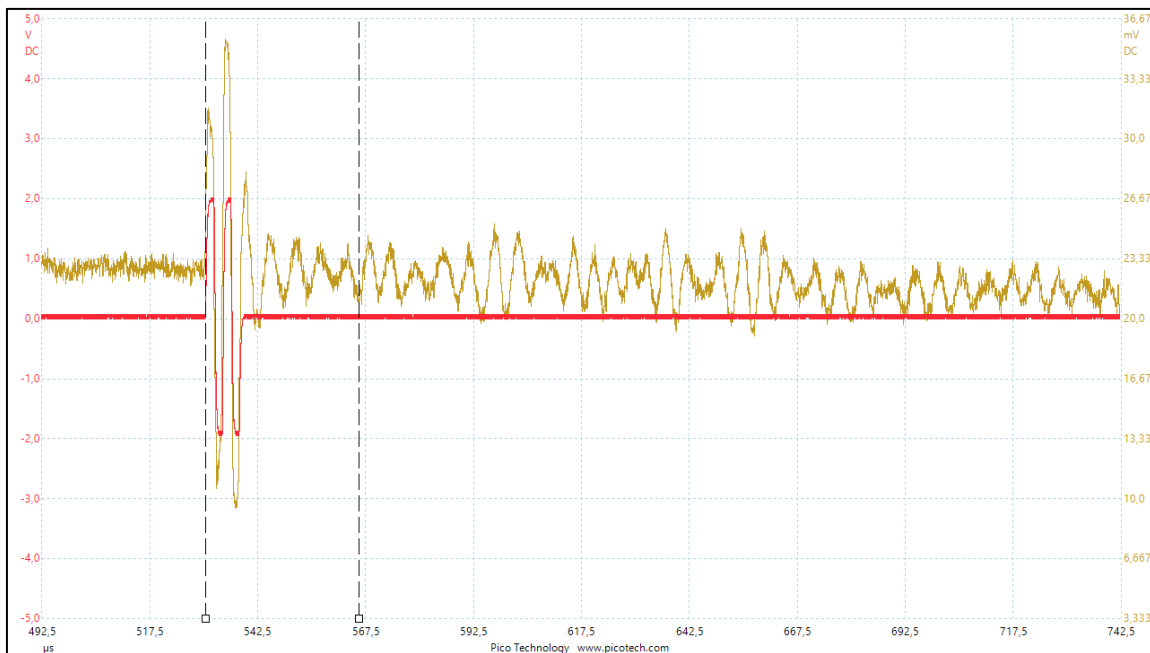


Figure 49: Acoustic signal collected after 24 hours curing.

The second comparison is at the end of carbon dioxide exposure, after 168 hours. The ultrasonic compressive strength test, according to API RP 10B-2, yielded a compressive strength of 5592 psi. **Figure 50** shows the acoustic reading taken after 168 hours of carbon dioxide exposure. The red curve depicts the transmitter signal and the yellow curve the pulse-echo type receiver signal. The dashed line marks the arrival. The signal taken from the pulse-echo type receiver after 168 hours of carbon dioxide exposure was significantly weaker than the one taken after 24 hours of curing. Due to the small signal amplitude, finding the correct arrival was difficult. The dashed line marks the supposed arrival. The sonic velocity calculated from this arrival is 3317.1 m/s leading to a compressive strength of 4430 psi.

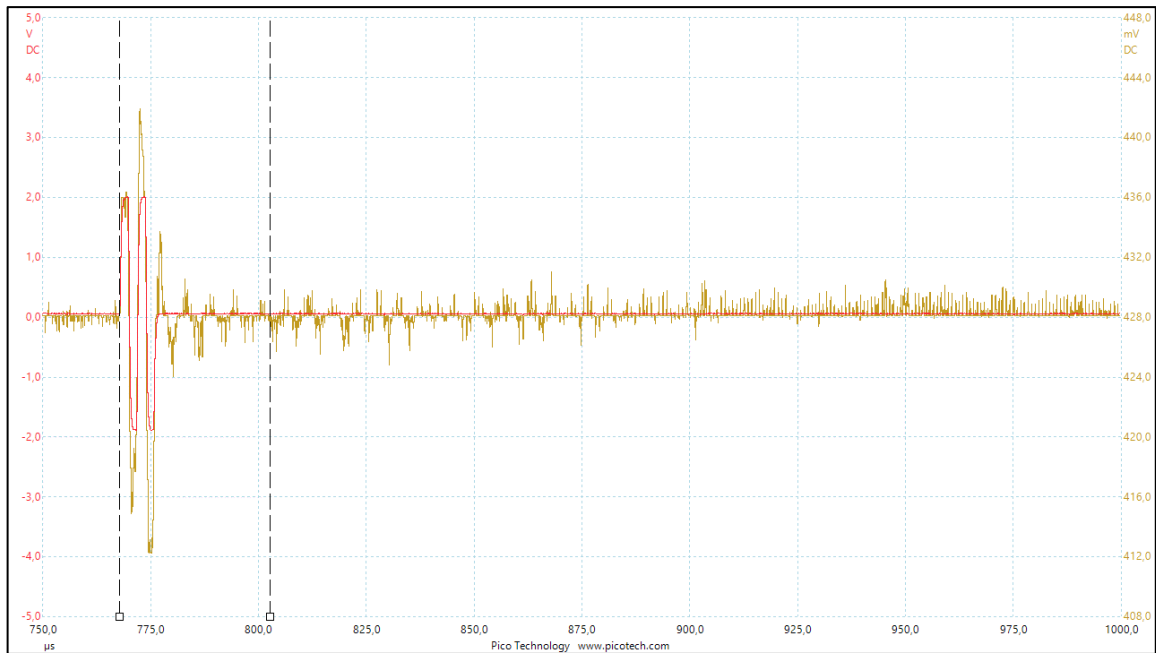


Figure 50: Acoustic signal collected after 168 hours of carbon dioxide exposure.

5.7.3.2 CT-Scan Analysis

The realization of the first scan took place prior to carbon dioxide injection to establish a baseline. This baseline also aids in monitoring for fractures as they occurred in the first experiment. The second scan followed after the carbon dioxide injection. From then on, CT-scan execution occurred every 24 hours up until the end of the experiment. **Figure 51** shows a cross-sectional image taken from this baseline CT-scan. Although the 17 ppg slurry exhibited high viscosity, a displacement of slurry into the channel within the sandstone occurred. The extent of this invasion was significantly lower than with the 11.5 ppg slurry. The slurry trapped a noticeable amount of air, also resulting from the high viscosity. This air entrapment hindered the acoustic analysis since the air is a bad acoustic conductor, and the presence of such entrapments along the acoustic travel path massively influence the readings.

The baseline CT-scan showed a slight curvature along the upper part of the sandstone core, which did not exist when cementing the core into the autoclave. Along this curvature, a debonding of the cement from the sandstone occurred, creating a flow path for carbon dioxide. Another big difference to the first experiment is the density difference between the cement and the sandstone. While the cement was easily distinguishable from the sandstone in the first experiment, this distinction is far more difficult in the second experiment. A close look still identifies the interface between the cement and the sandstone.

A second CT-scan taken immediately after the carbon dioxide injection shows the influence the pressure increase had on the cement and if the pressure caused any disruptions. **Figure 52** shows a cross-sectional view of this CT-scan. The high early compressive strength of this 17 ppg cement prevented fracturing. The small debonded section along the curved sandstone did not lead to a further debonding. Even right after the injection, changes in the CT-scan are visible.

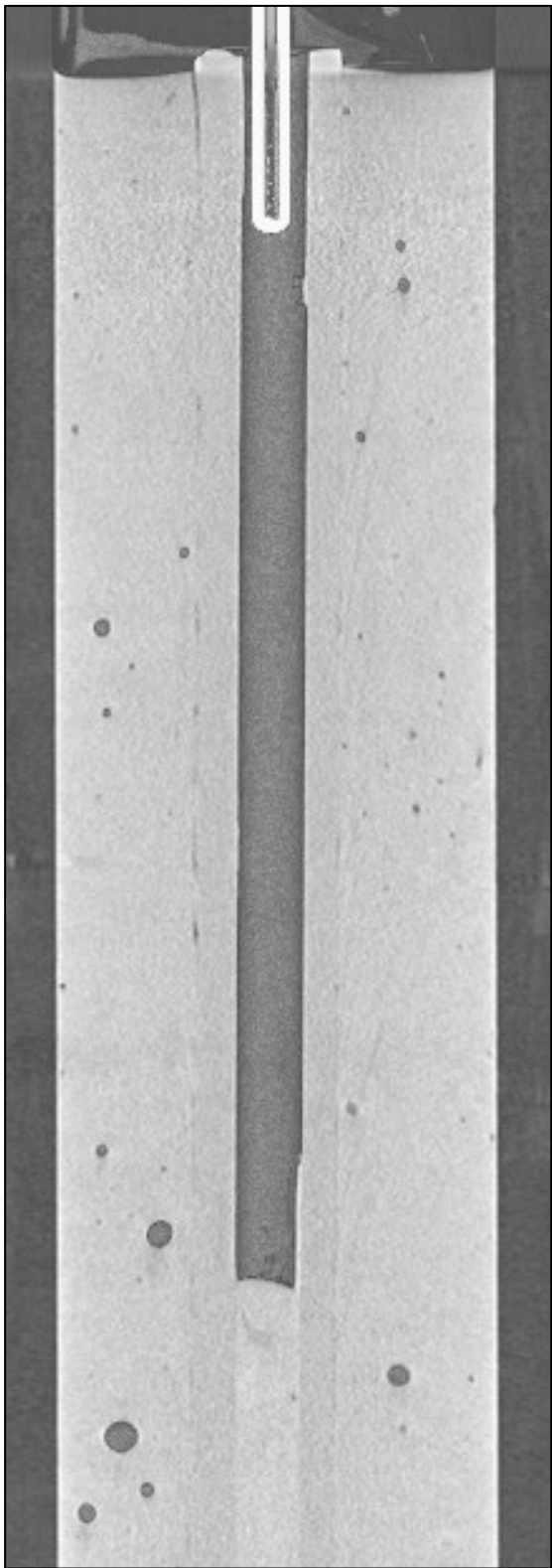


Figure 51: Baseline CT-scan of the 17 ppg cement before carbon dioxide injection.

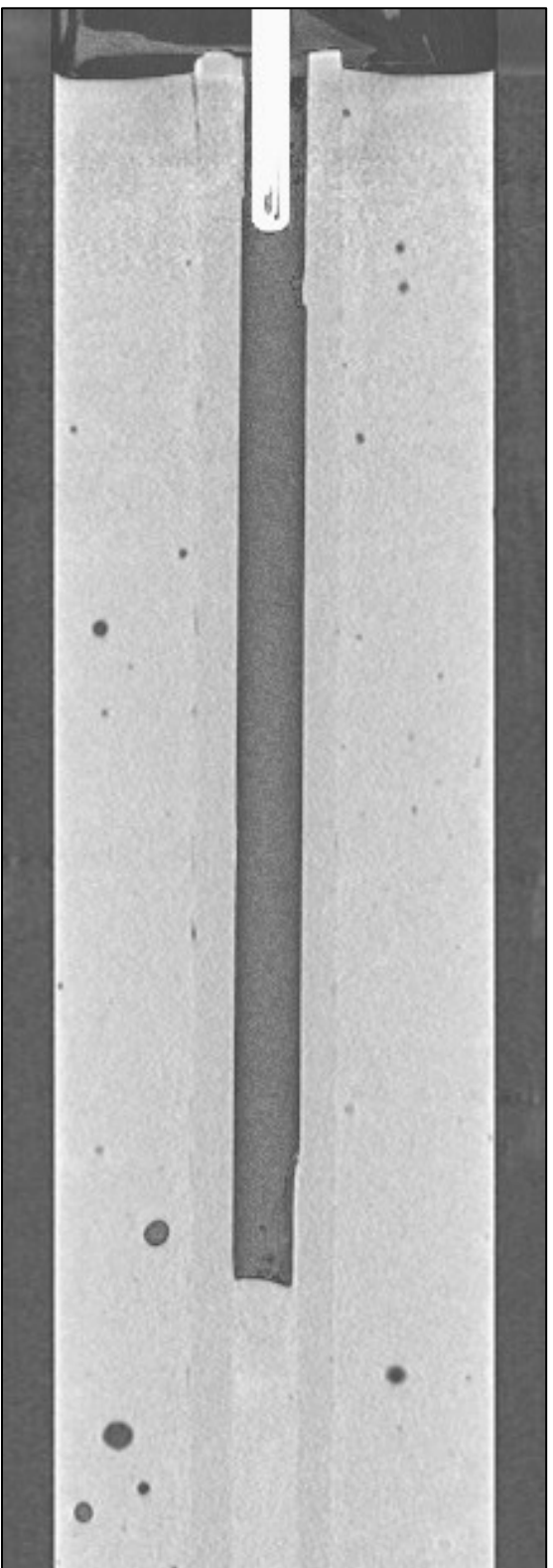


Figure 52: CT-scan taken immediately after carbon dioxide injection.

The next comparison gave the best insight into the carbonation for the 11.5 ppg cement. Comparing individual slices from different exposure times enables an easy way to monitor for carbonation along the sandstone. **Figure 53** shows this comparison. The problem with the 17 ppg slurry is, that the carbonation, as anticipated, only occurs marginally. The CT-scan comparison shows the development of a white corona around the sandstone. This corona is the carbonation. The carbonation leads to an increase in density, also causing the grayscale value to increase.

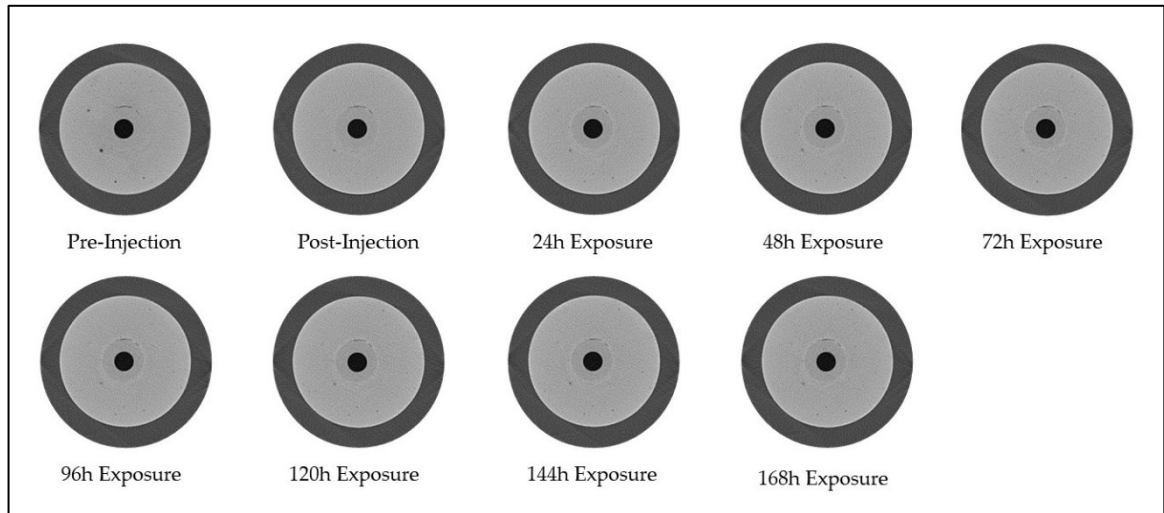


Figure 53: Comparison of individual slices from CT-scans taken at different times of carbon dioxide exposure.

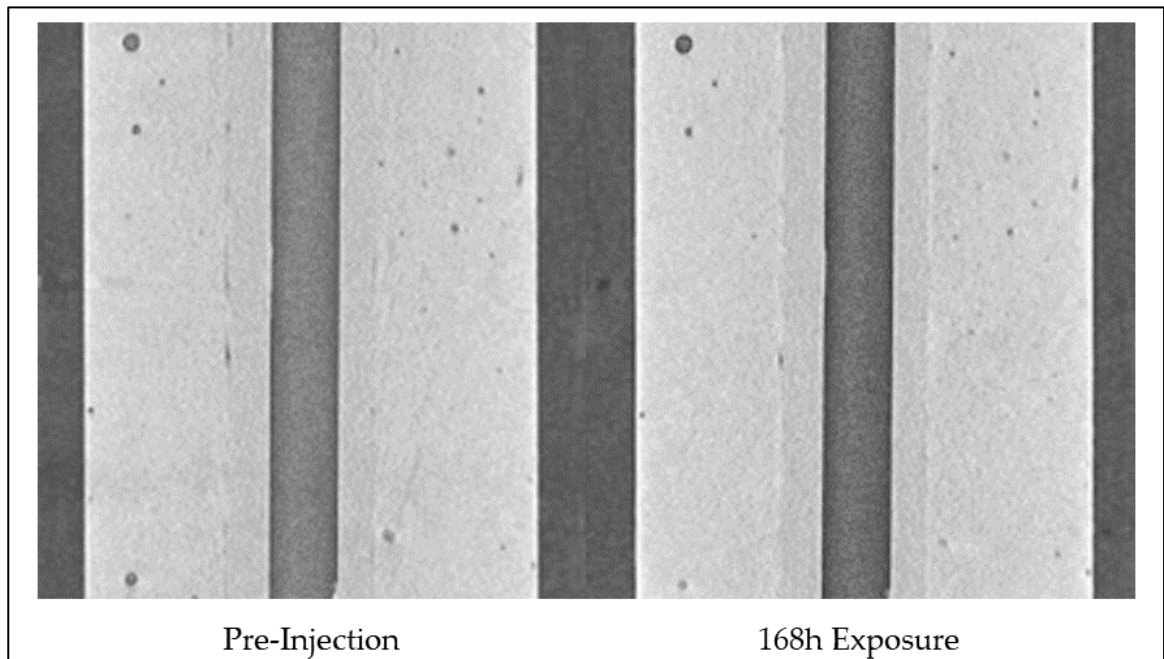


Figure 54: Comparison of a cross-section from a CT-scan before injection and after 168 hours of exposure.

Figure 54 shows a comparison of two cross-sections from different CT-scans. Comparing a pre-injection image, to the one with the most prolonged carbon dioxide exposure should give the most considerable differences. In this comparison, the images are different, but the carbonation only materializes as a white line along the sandstone.

5.7.4 Termination of the Experiment

After a total carbon dioxide exposure time of 168 hours, the experiment concluded. Bleeding off the remaining pressure of roughly 21 bars at a low and controlled rate ensures that the sample inside does not take damage. A fast pressure release could lead to deterioration of the fragile carbonate and bicarbonate. **Figure 55** illustrates the pressure and temperature development during the bleeding-off of the pressure.

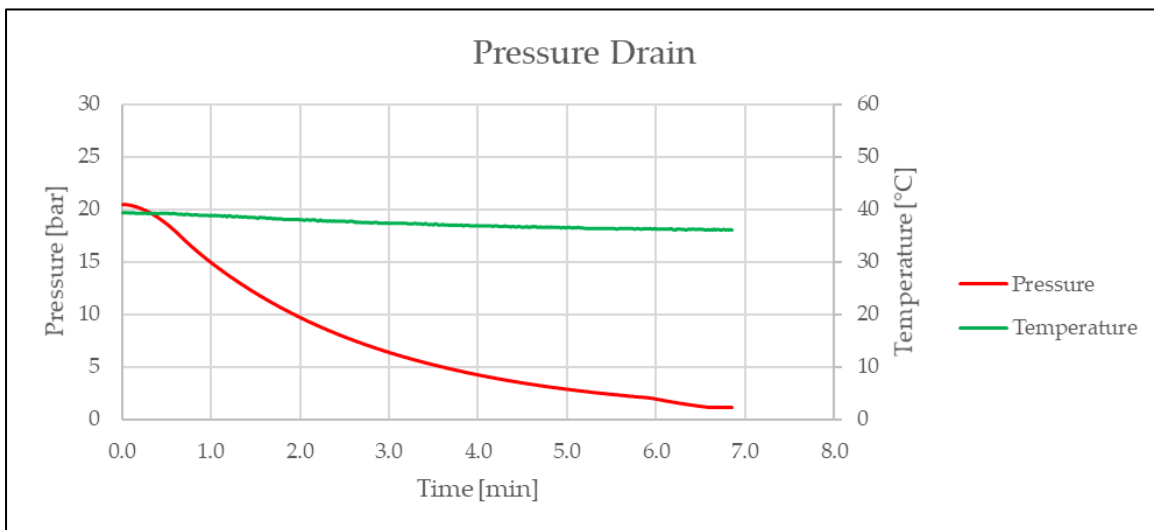


Figure 55: Pressure and temperature development during the pressure drain.

Once the pressure inside the autoclave reached the atmospheric level, loosening the flanges started. As with the 11.5 ppg cement, a noticeable amount of water was on top of the sample. The measurement of said water yielded an amount of 10 ml. After removing both flanges, the extraction of the sample started. This extraction proved to be more complicated than with the 11.5 ppg cement. The reason for this is most likely the far lower shrinkage of the 17 ppg cement; thus, the sample held better inside the autoclave. Eventually, the removal happened, and the sample stayed whole. The fractures inside the 11.5 ppg cement lead to it breaking into multiple pieces, whereas the sample of the 17 ppg cement stayed intact. Drilling and cutting disks and cylinders from the sample produced specimens for further analysis. **Figure 56** shows a photograph of a cut and dried disk from the 17 ppg cement after removal from the autoclave. The bond between the sandstone and cement was intact. Not even drilling or cutting specimens disrupted this bond.

5.7.5 Experiment II – Conclusion

The second experiment delivered the desired results. This experiment had the intention of delivering a baseline for a cement design that is not subject to considerable carbonation. Although some carbonation occurred as expected around the sandstone, the integrity of the bond stayed intact.

Right at the start, this experiment encountered the same issues as the first experiment. Immediately after disconnecting the carbon dioxide cylinder, the pressure started declining. Heating the entire autoclave did not increase the pressure inside. The reason for this decline in the first experiment was the rapid carbonation that occurred within the first 24 hours of the experiment. In this second experiment, almost no visible changes occurred within this period, but the pressure declined faster than in the first experiment. The pressure reached a stable plateau shortly after that and remained constant until the termination of the experiment.

The acoustic readings taken during the second experiment delivered results similar to the first experiment. One issue was that the reading at the end of carbon dioxide exposure, after 168 hours, only showed extraordinarily weak amplitudes, which made the evaluation of the data exceedingly harder. The value for the compressive strength of the 17 ppg cement taken from this reading is 4430 psi, which is 21% lower than the value from the compressive strength test according to API RP 10B-2. The carbonation subsequently caused a decrease in compressive strength of 21%. This decrease has an impact on the integrity of the cement, but the remaining compressive strength is still high. The examination of the sample and the bond between cement and sandstone proved the integrity of the cement as well.



Figure 56: Cut and dried disk of the 17 ppg cement after extraction from the autoclave.

5.8 Chemical and Mechanical Analysis

The analysis of the carbonation in this thesis was supposed to include a thorough chemical and mechanical analysis of samples created before and after the carbonation. Unfortunately, the results from the chemical and mechanical analysis did not arrive in time to be included in this thesis and will subsequently be the focus of a future publication. The types of tests conducted, as well as results from other publications, are the content of this chapter.

5.8.1 Mechanical Analysis

The primary intention of the mechanical analysis is to establish if the carbonation, and more so the degree of carbonation influence the compressive strength. The tests run in this analysis include a load-controlled uniaxial compressive strength test and a Brazilian test. The determination of these values occurs for cement poured into molds kept at atmospheric conditions for the same amount of time as the same slurry in the autoclave. Then drilling same-size samples from the cement sample within the autoclave delivers post-carbonation samples. Since the carbonation shows a front and does not occur evenly distributed throughout the cement, the choice of location where the samples stem from within the cement from the autoclave determines the degree of carbonation. Both samples, pre- and post-carbonation, have a one-inch diameter and are two-inches long. The comparison of the mechanical analysis of these samples enables concluding on the cement integrity.

5.8.2 Chemical Analysis

The primary intention of the chemical analysis is to deliver a thorough analysis of the dominant chemical species in the carbonated regions within both experiments. The tests to show this are scanning electron microscopy (SEM), x-ray diffraction (XRD), and thorough mineralogical analysis based on these two. **Figure 57** shows a comparison of two such SEM pictures. While the before-picture shown on the right, consists of the typical cement phases of calcium hydroxide, C-S-H-phases, and calcium silicates, the after-picture shows a different situation. The carbonation reaction leads to the formation

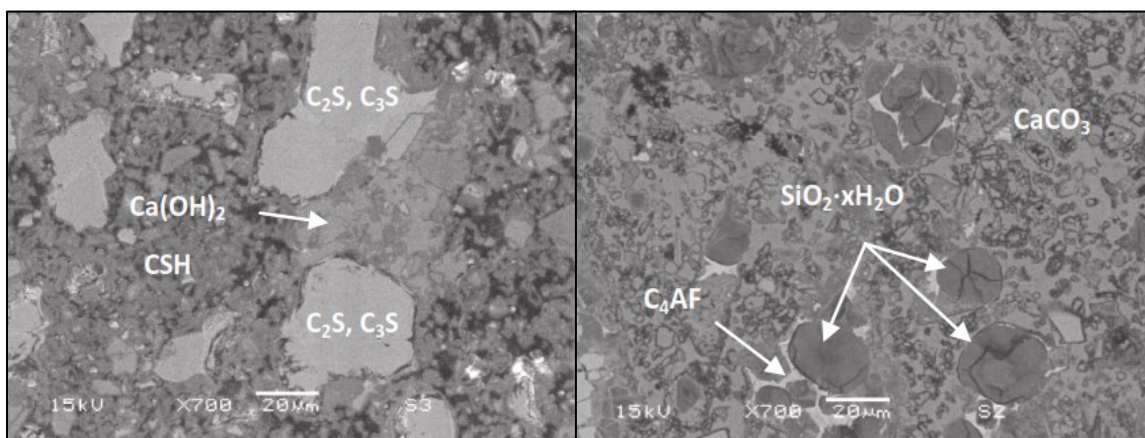


Figure 57: Comparison of two SEM pictures taken before carbonation (left) and after carbonation (right) (Urbonas et al. 2016).

of calcium carbonate and silica gel. The round beads, marked with $\text{SiO}_2 \cdot x\text{H}_2\text{O}$, are amorphous silica gel. These pictures show that the carbonation of this cement has wholly altered the chemical composition. **Figure 58** shows another interesting study of SEM pictures. In this study, the preparation of samples occurred by putting a caprock sample into a silicon mold and pouring cement slurry around it. Carbon dioxide exposure of these samples occurred under different conditions. Keeping one sample under a nitrogen atmosphere established the reference. The picture on the left shows that no debonding or other alterations occurred under the nitrogen atmosphere. The picture on the right is of the sample kept in carbon dioxide in solution. The bond between the caprock and the cement deteriorated, and calcium carbonate crystals started precipitating (Jobard et al. 2018).

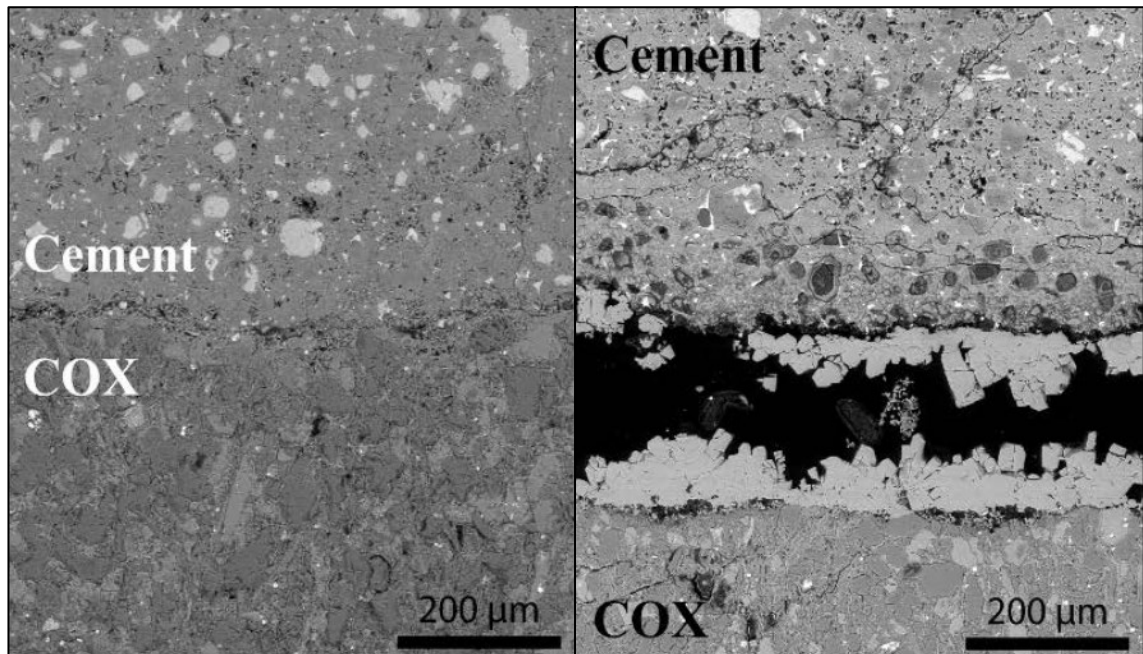


Figure 58: Comparison of two SEM pictures of the cement-cap rock taken after the same exposure in nitrogen (left) and carbon dioxide in solution (right) (Jobard et al. 2018).

Chapter 6 Comparison of the Experiments

This chapter focuses on the comparison of the collected data from the two experiments. This comparison facilitates more enhanced conclusions in terms of carbonation monitoring and shows the progress made in understanding the carbonation and its influencing factors.

6.1 Comparison of the Pressure and Temperature Data

Figure 59 shows graphs of the pressure and temperature development of both experiments spanning the entirety of carbon dioxide exposure. When injecting the carbon dioxide, both experiments showed a temperature increase due to the volumetric work of carbon dioxide. This temperature increase was significantly higher in the second experiment. The reason for this is the lower permeability and porosity of the 17 ppg cement. The carbon dioxide could not diffuse into the cement as quickly as with the 11.5 ppg cement, leading to a more substantial temperature increase. The heating provided 50 °C to the outside of the autoclave for both experiments. In experiment one, this leads to a stable temperature inside of roughly 35 °C and 40 °C in experiment two. The difference in the inside temperature resulting from the same heating temperature attributes to more effective heat conduction of the 17 ppg cement.

The pressure behaves differently in the experiments as well. The two most significant differences are the rate of pressure decline and the final pressure. Both experiments started with approximately the same pressure of 50 bar. In experiment one, the final pressure was 8 bar, and in experiment two, it was 20 bar. The cause of this difference is the amount of carbonation. The 11.5 ppg cement showed more diffusion of carbon dioxide due to higher permeability and porosity of the cement. Deeper diffusion leads to a higher degree of carbonation, causing a higher consumption of carbon dioxide. The other difference, the rate of pressure decline, is also noteworthy. The bulk of the pressure decline in experiment one happened within 20 hours, whereas it only took five hours in the second experiment. The decline within these 20 hours in experiment one was 30 bar, and the decline within five hours in experiment two was 20 bar. This difference in pressure decline is contrary to the diffusion assumption because the faster decline in the second experiment suggests that the gas diffused more quickly than in the first experiment. The planned diffusion path for both experiments is the channel inside the sandstone core. From there, the carbon dioxide diffuses through the sandstone towards the sandstone-cement interface and causes the carbonation. While the second experiment went according to plan, the pressure caused fractures within the cement in the first experiment. Due to these fractures, the carbon dioxide did not diffuse through the sandstone, but directly into the cement through the fractures. The main fracture in this experiment had a width of 1.5 mm, giving the carbon dioxide a large amount of additional space. It would have been interesting if the carbonation progresses at the same speed when the diffusion path is through the sandstone.

Both experiments did not reach the supercritical conditions for carbon dioxide, which start at 31.0 °C, and 73.8 bar. At first, the assumption was that the gaseous carbon dioxide would not cause significant carbonation within either of the types of cement, but the experiments showed that even the gaseous carbon dioxide carbonated both types of cement. Also, the time necessary for visible carbonation was exceedingly lower than anticipated. This assumption was three weeks for the first experiment, but most of the carbonation occurred within 24 hours. The second experiment would most likely have carbonated further, but for reasons of comparability, termination of the experiment took place after the same exposure period as the first experiment.

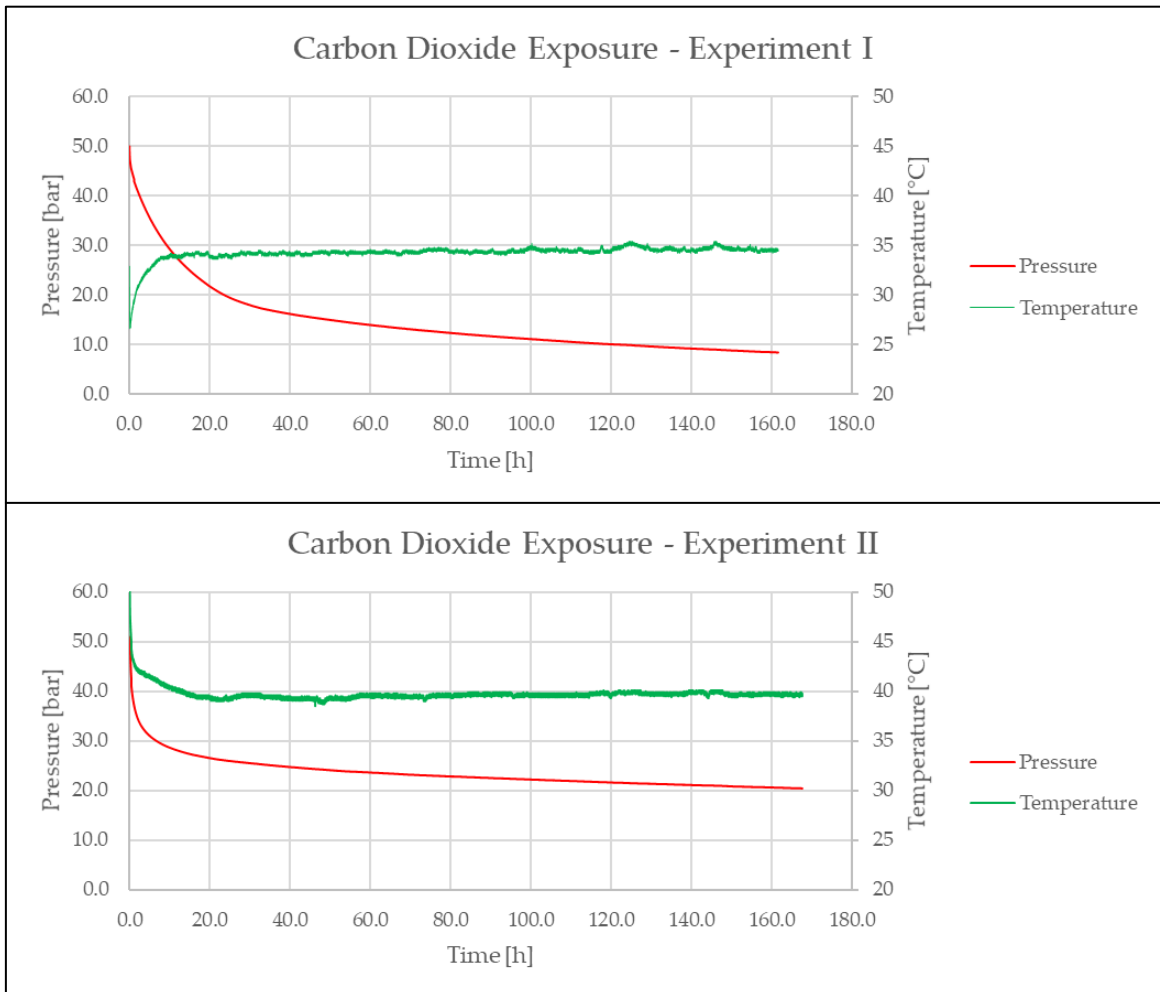


Figure 59: Pressure and temperature development during carbon dioxide exposure in both experiments.

6.2 Comparison of the CT-Scans

The main focus of these experiments was to prove that CT-scans make the carbonation of cement visible. The heavy-carbonation baseline generated by the first experiment showed vast differences in the carbonated cement versus the uncarbonated one. Even in the light-carbonation baseline generated by the second experiment, carbonation was visible. For these experiments, the focus was on the CT-scans over the acoustic readings. This decision meant keeping the autoclave at the same position in the CT-scanner. The

Comparison of the Experiments

electromagnetic field of the CT-scanner caused interference of the acoustic readings, leading to only two readings of each experiment. Keeping the autoclave at the same position in the CT-scanner enables far easier processing of the generated images.

Figure 60 shows four cross-sectional views, two from the first and two from the second experiment. For both experiments, the images stem from before carbon dioxide injection and at the end of carbon dioxide exposure. The first noticeable difference is the greyscale value of the cement. A higher density has a higher greyscale value, which is visible when comparing the CT-scans of the 11.5 ppg cement to the ones from the 17 ppg cement. The carbonation leads to a significant density increase in the 11.5 ppg cement, making the carbonation distinctly visible. The carbonation only causes a marginal density increase in the 17 ppg cement, leading to a white corona around the sandstone. When comparing the two scans of the 17 ppg cement, there is a noticeable difference. Whereas the interface between cement and sandstone was hardly visible before the carbon dioxide injection, this interface is distinctly visible after 168 hours of carbon dioxide exposure.

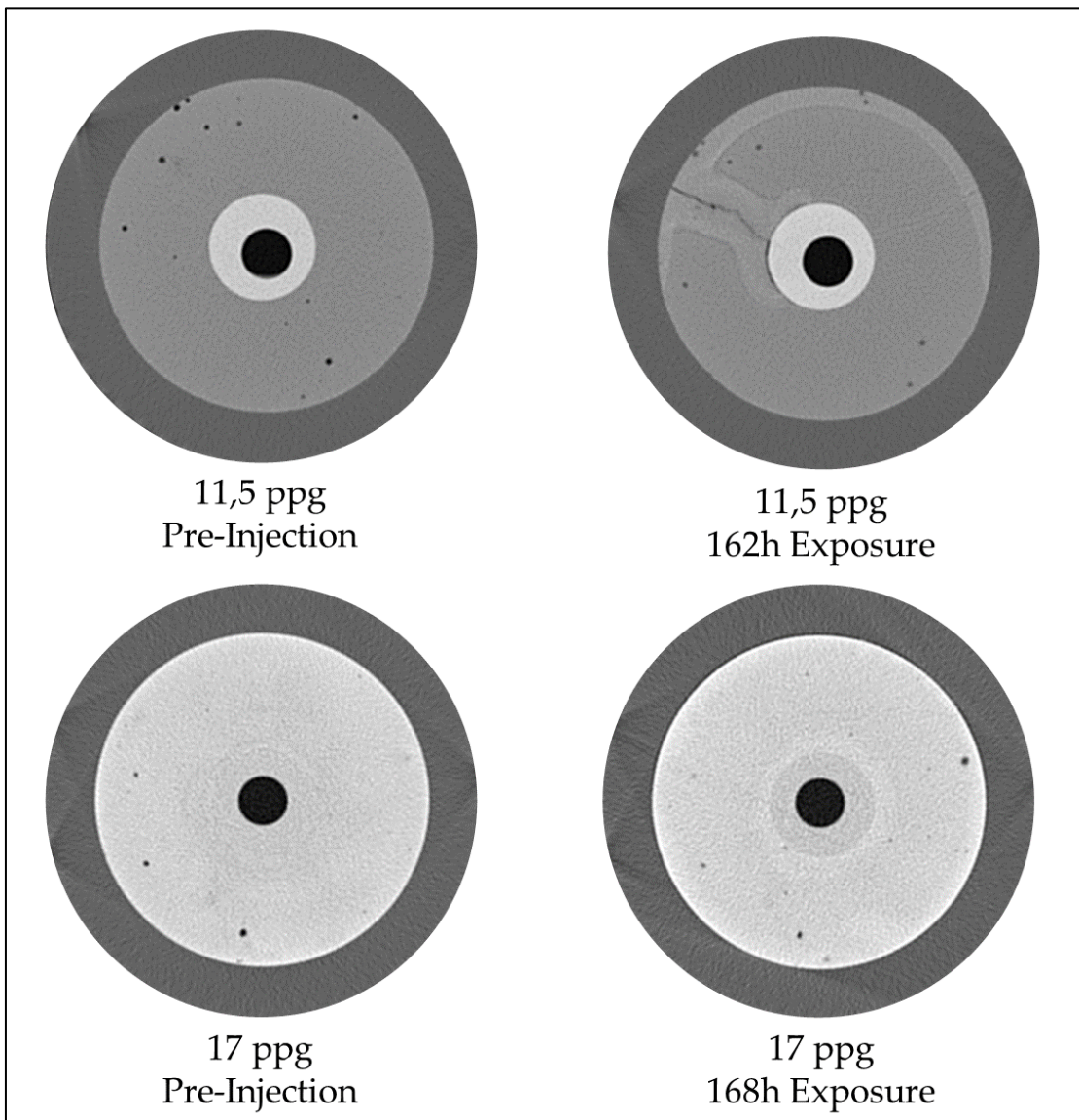


Figure 60: Comparison of cross-sectional views of both experiments.

When looking at a cross-sectional view of the CT-scans from the side, as pictured in **Figure 61**, the understanding of the carbonation at a larger scale becomes easier. In the 11.5 ppg cement, even though the pressure fractured the cement, creating additional flow paths, the carbon dioxide diffused through the sandstone towards the cement. The fracture in the 11.5 ppg cement caused one side to carbonate heavier. This side is the side of the fracture. The cement debonded from the sandstone in an interval that closely matches the non-cemented channel. Here the debonding comes from the carbon dioxide that diffused through the sandstone. On the other side, the scan from the second experiment shows precisely what was anticipated. The carbon dioxide diffused evenly through the sandstone, creating a uniform layer of carbonation along the cement-sandstone interface. As mentioned earlier, the density difference of the carbonated to uncarbonated cement is noteworthy. With the 11.5 ppg cement, this difference is significant, whereas, with the 17 ppg slurry, this difference is marginal.

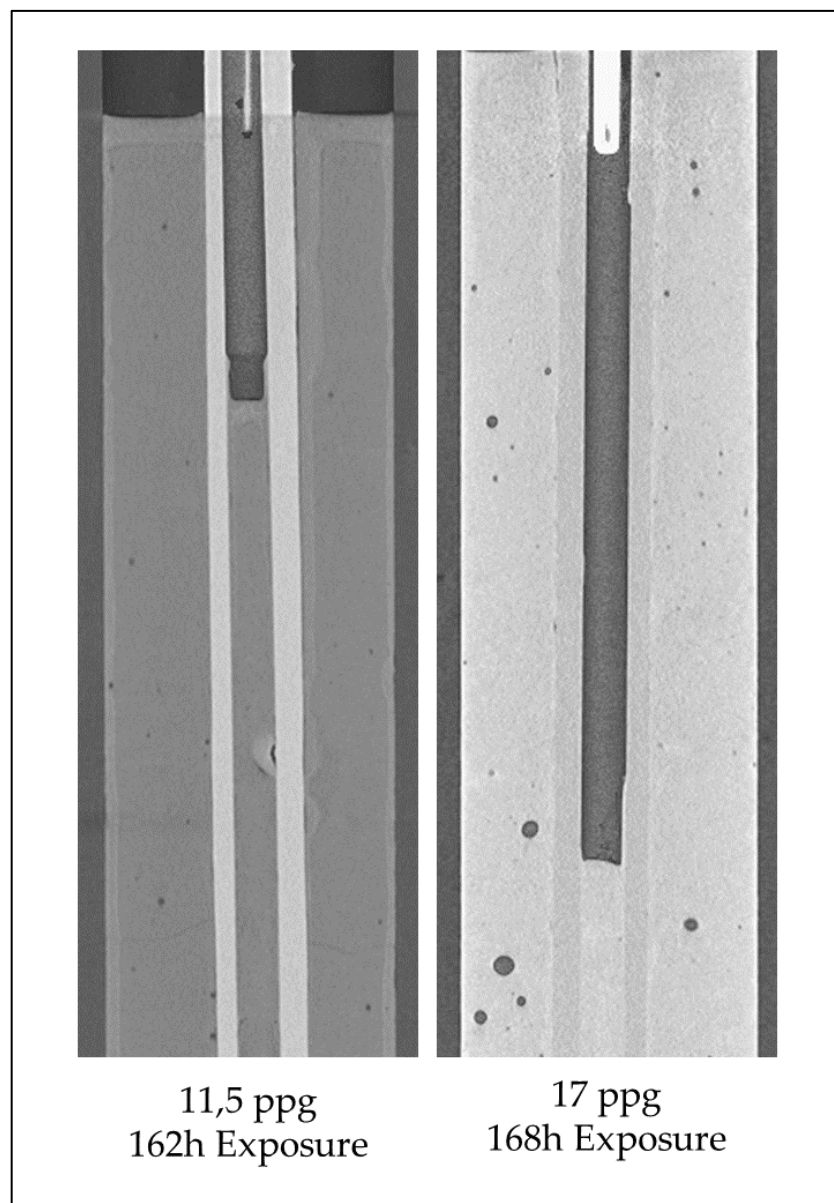


Figure 61: Comparison of a side cross-sectional view of both experiments at the end of carbon dioxide exposure.

Chapter 7 Conclusion

This thesis found two suitable ways to monitor the carbonation of cement caused by carbon dioxide in a supercritical state, in real-time. The autoclave built to facilitate these real-time measurements proved applicable. The design provides a gas-tight autoclave in which the interface of a formation core and cement can be studied under the influence of carbon dioxide.

The gas expansion due to temperature increase should generate the supercritical condition for carbon dioxide for both experiments in this thesis. The autoclave filled with carbon dioxide mimics an isochoric process, meaning that a temperature increase leads to a pressure increase. Due to the rapid speed of the carbonation reactions and a sub-optimal vacuum within the autoclave, reaching supercritical conditions for carbon dioxide never occurred. On the contrary, the carbonation and carbon dioxide diffusion into the cement and sandstone cause the pressure to drop as soon as the carbon dioxide cylinder was disconnected. Thus, the creation of supercritical conditions for carbon dioxide by gas expansion in this autoclave is disproven. A pump is necessary to create the supercritical conditions as well as for measuring the exact amount of carbon dioxide injected into the autoclave.

Along with the design and construction of the autoclave, two methods of monitoring the carbonation in real-time were tested, one of them conclusively proven. The first method is the analysis of the carbonation through CT-scanning. For this purpose, the autoclave design had to permit CT-scans, and the pipe-body of the autoclave was subsequently manufactured from PEEK polymer. The CT-scans taken over the carbon dioxide exposure periods of both experiments showed that the carbonation is visible. In the high-carbonation baseline taken from the first experiment, the carbonation happened quickly and to a much further degree than anticipated. The CT-scans from this experiment show a clear differentiation between the carbonated and uncarbonated cement. From these scans, the generation of carbonation progression curves was possible. The light-carbonation baseline taken from the second experiment also delivered suitable data. The difference in densities of carbonated versus uncarbonated cement in the second experiment was significantly lower than in the first. This lower difference made the characterization of the carbonation on the CT-scans more challenging. Still, the detection of carbonation was possible, but not as conclusively as in the first experiment.

The second method of cement carbonation detection is the usage of ultrasonic signals and their attenuation and travel times. The collected data showed promising results for determining the compressive strength of the cement in the autoclave from acoustic signals. For a more precise and more comfortable process of using the acoustic signals, a more extensive database is necessary. This database needs to include cement designs as used in the autoclave, at various densities and compositions.

The carbonation of cement created in the experiments of this thesis showed how extreme even the influence of gaseous carbon dioxide is on cement and its integrity. The types of cement utilized in carbon capture and storage need to conclusively be studied for their carbonation immunity before being used in the field.

Bibliography

Aiex, C., Campos, G., Deshpande, A. et al. 2015. An Experimental Study on Effects of Static CO₂ on Cement under High-Pressure/High-Temperature Conditions. In *Offshore Technology Conference*. Offshore Technology Conference. <https://doi.org/10.4043/25659-MS>.

Air Liquide. Gas Encyclopedia, <https://encyclopedia.airliquide.com/>.

Allinson, W. G., Nguyen, D. N., and Bradshaw, J. 2003. The Economics of Geological Storage of CO₂ in Australia. *The APPEA Journal* **43** (1): 623. <https://doi.org/10.1071/AJ02035>.

ANSI/API 10A/ISO 10426-1-2001, *API Specification for Cements and Materials for Well Cementing*. 2002. Washington D.C.: American Petroleum Institute.

Bert Metz (ed.). 2005. *IPCC Special Report on Carbon Dioxide Capture and Storage*. Cambridge: Cambridge Univ. Press.

Bock, B., Rhudy, R., Herzog, H. et al. 2003. *Economic Evaluation of CO₂ Storage and Sink Enhancement Options*. <https://doi.org/10.2172/826435>.

Brown, P. W., Franz, E., Frohnsdorff, G. et al. 1984. Analyses of the Aqueous Phase During Early C₃S Hydration. *Cement and Concrete Research* **14** (2): 257–262. [https://doi.org/10.1016/0008-8846\(84\)90112-1](https://doi.org/10.1016/0008-8846(84)90112-1).

Bruckdorfer, R. A. 1986. Carbon Dioxide Corrosion in Oilwell Cements. In *SPE Rocky Mountain Regional Meeting*. Society of Petroleum Engineers. <https://doi.org/10.2118/15176-MS>.

Burrascano, P., Callegari, S., Montisci, A. et al. (eds.). 2015. *Ultrasonic Nondestructive Evaluation Systems: Industrial application issues*. Cham: Springer. <https://doi.org/10.1007/978-3-319-10566-6>.

Chris Hendricks, Wina Crijns-Graus, Frank Bergen. 2004. Global Carbon Dioxide Storage Potential and Costs. *INIS* **35** (26).

Dent Glasser, L. S., Lachowski, E. E., Mohan, K. et al. 1978. A Multi-Method Study of C₃S Hydration. *Cement and Concrete Research* **8** (6): 733–739. [https://doi.org/10.1016/0008-8846\(78\)90082-0](https://doi.org/10.1016/0008-8846(78)90082-0).

Fleming, A. J. 2009. A Megahertz Bandwidth Dual Amplifier for Driving Piezoelectric Actuators and Other Highly Capacitive Loads. *Rev Sci Instrum* **80** (10): 104701. <https://doi.org/10.1063/1.3234261>.

Gedde, U. W. 2020. *Essential Classical Thermodynamics*, firstst ed. twentiethtwentieth. Cham: Springer International Publishing; Springer.

Goel, M., Sudhakar, M., and Shahi, R. V. 2018. *Carbon Capture, Storage and Utilization: A possible climate change solution for energy industry*. Boca Raton, FL: Routledge, Taylor & Francis Group.

- IEA. 2016. 20 Years of Carbon Capture and Storage - Accelerating Future Deployment, 27 March 2020, <https://www.oecd.org/publications/20-years-of-carbon-capture-and-storage-9789264267800-en.htm> (accessed 27 March 2020).
- Institute for 21st Century Energy. 2012. *CO₂ Enhanced Oil Recovery*.
- Jobard, E., Sterpenich, J., Pironon, J. et al. 2018. Experimental Modelling of the Caprock/Cement Interface Behaviour under CO₂ Storage Conditions: Effect of Water and Supercritical CO₂ from a Cathodoluminescence Study. *Geosciences* **8** (5): 185. <https://doi.org/10.3390/geosciences8050185>.
- John W. Anthony. 1995. *Handbook of Mineralogy*. Chantilly, VA, USA: Mineralogical Society of America.
- JRC / PBL. Emission Database of Global Atmospheric Research (EDGAR), <http://edgar.jrc.ec.europa.eu/>.
- Krautkrämer, J. and Krautkrämer, H. 1990. *Ultrasonic Testing of Materials*, fourthth Fully Revised Edition. Berlin, Heidelberg: Springer. <https://doi.org/10.1007/978-3-662-10680-8>.
- Lacerda E., Magalhaes, A. G., Bernardes E.E. et al. 2017. Monitoring the carbonation front progress in a cementitious composite having its pore structure analyzed through μ -CT imaging. *Rev. IBRACON Estrut. Mater.* **10** (3): 653–668. <https://doi.org/10.1590/s1983-41952017000300006>.
- Lerch, R., Sessler, G. M., and Wolf, D. 2009. *Technische Akustik: Grundlagen und Anwendungen*. Berlin, Heidelberg: Springer Berlin Heidelberg. <https://doi.org/10.1007/978-3-540-49833-9>.
- Mathez, E. A. and Smerdon, J. E. 2018. *Climate change: The Science of Global Warming and our Energy Future*, Second edition. New York: Columbia University Press.
- Nelson, E. B. and Guillot, D. 2006. *Well Cementing*, secondnd ed. Sugar Land, Tex.: Schlumberger.
- Onan, D. D. 1984. Effects of Supercritical Carbon Dioxide on Well Cements. In *Permian Basin Oil and Gas Recovery Conference*. Society of Petroleum Engineers. <https://doi.org/10.2118/12593-MS>.
- Österreichische Bundesverfassung. 2004. *Verordnung des Bundesministers für Wissenschaft, Forschung und Wirtschaft über sicherheitstechnische Bestimmungen für Prüfungen bei der Inbetriebnahme und während des Betriebes von Druckgeräten (Druckgeräteüberwachungsverordnung): DGÜW-V*.
- P. Barret (ed.). 1986. *Hydration Mechanism of Calcium Silicates (C₃S, C₂S), Cement Compounds, Through the General Concepts of the Reactivity of Solids*.
- PI Ceramic GmbH. 2020. Fundamentals of Piezo Technology, <https://www.piceramic.com/>.
- Rupitsch, S. J. 2019. *Piezoelectric Sensors and Actuators: Fundamentals and Applications*. Berlin, Heidelberg: Springer Berlin Heidelberg. <https://doi.org/10.1007/978-3-662-57534-5>.

Bibliography

Saini, D. 2017. *Engineering Aspects of Geologic CO₂ Storage: Synergy between Enhanced Oil Recovery and Storage*. Cham, s.l.: Springer International Publishing. <https://doi.org/10.1007/978-3-319-56074-8>.

Seevam, P. N., Downie, M. J., and Race, J. M. 2007. Transport of CO₂ for Carbon Capture and Storage in the UK. In *SPE Offshore Europe Oil and Gas Conference and Exhibition*. Society of Petroleum Engineers. <https://doi.org/10.2118/109060-MS>.

Tumidajski, P. J. and Thomson, M. L. 1994. Influence of cadmium on the hydration of C3A. *Cement and Concrete Research* **24** (7): 1359–1372. [https://doi.org/10.1016/0008-8846\(94\)90121-X](https://doi.org/10.1016/0008-8846(94)90121-X).

Acronyms

<i>API</i>	American Petroleum Institute
<i>C-S-H-Phase</i>	Calcium Silicate Hydrate Phase
<i>CCS</i>	Carbon Capture and Storage
<i>CT</i>	Computer Tomography
<i>μ-CT</i>	X-ray Microtomography
<i>DGÜW-V</i>	Druckgeräteüberwachungsverordnung Pressure Equipment Monitoring regulation
<i>DIN</i>	Deutsches Institut für Normung German Institute for Standardization
<i>DN</i>	Diamètre nominal Nominal Pipe Size
<i>EN</i>	European Norm
<i>EOR</i>	Enhanced Oil Recovery
<i>HSR</i>	High Sulfate Resistant
<i>IEA</i>	International Energy Agency
<i>MSR</i>	Moderate Sulfate Resistant
<i>PEEK</i>	Poly Ether Ether Ketone
<i>PN</i>	Pressure Nominal Nominal Pressure
<i>PZT</i>	Lead Zirconate Titanate
<i>RP</i>	Recommended Practice
<i>RPM</i>	Revolutions Per Minute
<i>SEM</i>	Scanning Electron Microscopy
<i>UCA</i>	Ultrasonic Compressive Strength Analysis
<i>US\$</i>	United States Dollar
<i>WAG</i>	Water Alternating Gas
<i>WTI</i>	West Texas Intermediate
<i>XRD</i>	X-ray Diffraction

Symbols

A	Area	[m ²]
C_p	Capacitance Piezo	[F]
E_d	Dynamic Young's Modulus	[-]
f	Frequency	[kHz]
I	Intensity	[W/m ²]
$I_{max,sine}$	Maximum Current of a Sine Wave	[A]
I_{RMS}	Root Mean Square Current	[A]
L_p	Sound Level	[dB]
m	Mass	[g, kg, t, Gt]
P	Power	[W]
p	Pressure	[bar, mbar, psi]
π	Pi	[-]
R	Reflection Coefficient	[-]
ρ	Density	[kg/m ³ , ppg, s.g.]
s	Distance	[mm, cm, m, km, “]
T	Temperature	[°C]
T	Transmission Coefficient	[-]
t	Time	[μs, min, h]
V	Volume	[ml, l, cc]
V_{rms}	Root Mean Square Voltage	[V]
v_p	p-Wave Velocity	[m/s]
v_s	s-Wave Velocity	[m/s]
Z	Acoustic Impedance	[kg/m ² s]

List of Figures

Figure 1: Comparing the amount of CO ₂ emission to the total amount of greenhouse gas emission (JRC / PBL).	1
Figure 2: Worldwide locations of carbon dioxide storage activities (Bert Metz 2005).	3
Figure 3: Three basic systems of carbon dioxide capture (IEA 2016).....	4
Figure 4: Simplified depiction of observations during clinker phase hydration (Nelson and Guillot 2006).	11
Figure 5: Simplified Quartz crystal illustrating the piezoelectric effect (Rupitsch 2019).	16
Figure 6: The piezoelectric element utilized for the cement analysis in this thesis.	17
Figure 7: Graphical depiction of Snellius-Descartes law of refraction (Burrascano et al. 2015)...	19
Figure 8: Set-up of the ultrasonic sensing system.	21
Figure 9: Evaluation of acoustic travel time in cement samples with different curing times.	22
Figure 10: Graph showing the matching of sonic velocity to compressional strength for different density samples and periods of curing-.	23
Figure 11: Exploded view of the autoclave, including all components.	26
Figure 12: Graphical depiction of the pressure decay during the first pressure test.	27
Figure 13: Stirrer utilized to mix the cement slurry in the batch mixer.	28
Figure 14: Stainless steel container used for slurry mixing in the batch mixer.	29
Figure 15: Sequential order to tighten bolts on flanges to ensure a gas-tight seal.	29
Figure 16: Schematic of the placement of the formation core inside the autoclave.	30
Figure 17: Core-centralizer used to place the formation core in the center of the autoclave.....	30
Figure 18: Schematic of the vibrating table used for cement slurry conditioning.	31
Figure 19: Position of the autoclave with appliances on the platform lift for the duration of the experiment.....	32
Figure 20: A schematic showing the distinction between low- and high-risk pressure equipment containing media of group II.	34
Figure 21: Risk matrix used to evaluate risks associated with the operation of the autoclave. ...	36
Figure 22: Rheological data of the 11.5 ppg slurry.	37
Figure 23: Sedimentation test of the 11.5 ppg slurry.....	38
Figure 24: Pressure and temperature development during vacuum creation.....	39
Figure 25: Schematic of the flow circuit used to create the vacuum.	39
Figure 26: Schematic of the circuit used to inject the carbon dioxide into the autoclave.....	40
Figure 27: Pressure and temperature development during carbon dioxide injection.	40
Figure 28: Pressure and temperature development during the experiment.....	41
Figure 29: Photograph of the PEEK pipe-body with attached flanges and acoustic sensors.	42
Figure 30: Compressive strength development of the 11.5 ppg slurry tested according to API RP 10B-2.	42
Figure 31: Excerpt from the oscilloscope readings of the pulse-echo receiver before the carbon dioxide injection.	43
Figure 32: Distance traveled by the acoustic signal through the 11.5 ppg cement in the pulse-echo set-up.....	43
Figure 33: Excerpt from the oscilloscope readings of the pulse-echo receiver after 162 hours of carbon dioxide exposure.	44
Figure 34: Cross-sectional view of the first CT-scan.	45
Figure 35: Photograph of the autoclave inside the CT-scanner.....	45
Figure 36: Top- and side-cross-sectional view exposing the crack formed during carbon dioxide injection.....	46

List of Figures

Figure 37: Carbonation progression of the 11.5 ppg cement visualized with single slices of the corresponding CT-scans.	47
Figure 38: Graphical depiction of the carbonation progression at different locations in the cement sample.....	47
Figure 39: Pressure and temperature progression during the bleeding off of the pressure.	48
Figure 40: Photograph of the cement and sandstone after extracting it from the autoclave.	48
Figure 41: Cut and dried piece from one of the segments of the 11.5 ppg cement after carbon dioxide exposure.....	49
Figure 42: Rheological data of the 17 ppg slurry.	51
Figure 43: Data from the sedimentation test of the 17 ppg slurry.	52
Figure 44: Pressure and temperature development during vacuum generation.	53
Figure 45: Pressure and temperature development during the pressurization of the autoclave.	53
Figure 46: Pressure and temperature development during the experiment.	54
Figure 47: Compressive strength development of the 17 ppg slurry tested according to API RP 10B-2.	55
Figure 48: Distance traveled by the acoustic signal through the 17 ppg cement in the pulse-echo set-up.....	55
Figure 49: Acoustic signal collected after 24 hours curing.	56
Figure 50: Acoustic signal collected after 168 hours of carbon dioxide exposure.	57
Figure 51: Baseline CT-scan of the 17 ppg cement before carbon dioxide injection.	58
Figure 52: CT-scan taken immediately after carbon dioxide injection.....	58
Figure 53: Comparison of individual slices from CT-scans taken at different times of carbon dioxide exposure.....	59
Figure 54: Comparison of a cross-section from a CT-scan before injection and after 168 hours of exposure.....	59
Figure 55: Pressure and temperature development during the pressure drain.	60
Figure 56: Cut and dried disk of the 17 ppg cement after extraction from the autoclave.....	61
Figure 57: Comparison of two SEM pictures taken before carbonation (left) and after carbonation (right) (Urbonas et al. 2016).	62
Figure 58: Comparison of two SEM pictures of the cement-cap rock taken after the same exposure in nitrogen (left) and carbon dioxide in solution (right) (Jobard et al. 2018).....	63
Figure 59: Pressure and temperature development during carbon dioxide exposure in both experiments.	65
Figure 60: Comparison of cross-sectional views of both experiments.....	66
Figure 61: Comparison of a side cross-sectional view of both experiments at the end of carbon dioxide exposure.....	67

List of Tables

Table 1: Potential storage capacity of the eligible formations (Bert Metz 2005).	6
Table 2: Reported carbon dioxide storage costs from different studies and reports (Allinson et al. 2003; Bock et al. 2003; Chris Hendricks, Wina Crijns-Graus, Frank Bergen 2004).	8
Table 3: Chemical requirements for API Class G high-sulfate resistant cement (<i>ANSI/API 10A/ISO 10426-1-2001</i> 2002).	11
Table 4: Risk evaluation for the operation of the autoclave for continuous carbonation monitoring.	35
Table 5: Risks that require mitigation and the corresponding mitigation.	36
Table 6: Slurry data of the 17 ppg slurry.	51